UNIVERSITÀ DEGLI STUDI DI PADOVA

Dipartimento di Fisica e Astronomia "Galileo Galilei"

Master Degree in Physics

Final Dissertation

Characterization of a novel electromagnetic calorimeter for high-energy muon collisions at $\sqrt{s} = 10$ TeV

Thesis supervisor
Prof. Donatella Lucchesi
Thesis co-supervisor
Dr. Lorenzo Sestini

Candidate
Carlo Giraldin

Academic Year 2023/2024

Contents

Introduction

The Muon Collider represents a promising future collider project, designed to collide beams of muons (μ^-) and antimuons (μ^+) in a circular geometry at multi-TeV center-of-mass energies. The idea of a μ^- μ^+ collider dates back to the 1960s and 1970s [1], but due to the significant technical challenges posed by the short lifetime of muons, the proposal was concretely considered only in the 2000s.

Between 2011 and 2014, the Muon Accelerator Program (MAP) [2] in the U.S. made it possible to obtain the development of a first concept of a Muon Collider. These studies were a fundamental basis on which the current International Muon Collider Collaboration (IMCC) [3] was born. Actually the IMCC is focused on the full development of the project, encompassing the facility, the detector, and the relevant physics studies.

The purpose of this thesis is to provide an initial characterization of a novel electromagnetic calorimeter proposal, the CRILIN (CRystal calorImeter with Longitudinal INformation) calorimeter, as part of the ongoing development activities for the Muon Collider detector. The research and development of new technical solutions for the Muon Collider detector are of primary importance, as this novel collider presents unique challenges. One of the most significant challenges is the presence of an intense background of particles within the detector, generated by the in-flight decay of muons. This background, known as Beam-Induced Background (BIB), creates a considerable challenge for the detector's performance and requires innovative solutions both at software and hardware level for its mitigation.

For the characterization of CRILIN, I focused primarily on simulation studies, integrating the new CRILIN calorimeter into the detector with different design configurations and analyzing its performance using photon samples. In parallel with these activities, I had the opportunity to participate in experimental tests on the CRILIN prototype, where I contributed both to the data acquisition process and actively participated in the subsequent data analysis.

The work have been structured in this thesis as follows:

- **Chapter 1: Why a Muon Collider**

  In the first chapter provides a general description of the Muon Collider project. The initial section outlines the advantages that justify the use of muon beams for a collider experiment, highlighting the most relevant physical cases of interest. The next section describes the scheme of the entire accelerator complex for the Muon Collider, developed by the MAP collaboration. The production of muon beams is one of the most critical aspects of the project and this section describes the various steps from the production of the beams, to their acceleration, up to the moment of the collision. In the last two sections, a presentation of the Beam Induced Background (BIB) is given, detailing the design of the machine-detector interface that plays a key role in mitigating the BIB particle flux entering the detector region. In this context, the most important component is represented by the pair of tungsten conical absorbers positioned around the interaction point.

- **Chapter 2: Detector description**

In this chapter, the design concept of the Muon Collider detector for the 10 TeV center-of-mass energy phase on which my simulation work has focused is presented.

- **Chapter 3: Detector simulation and physics objects reconstruction**

  This chapter provides an overview of the simulation process and the reconstruction of physical objects, illustrating the main software tools used in the physics and detector development studies conducted within the IMCC.

- **Chapter 4: An electromagnetic calorimeter for a Muon Collider Detector**

  This chapter is devoted to the presentation of the main requirements of the electromagnetic calorimeter for a Muon Collider experiment. Starting from these specifications, the new proposal of the CRILIN calorimeter is introduced, which was the focus of the work carried out in my thesis.

- **Chapter 5: Characterization of CRILIN performance in Muon Collider detector**

  The simulation studies I conducted regarding the characterization of CRILIN performance are presented in this chapter. These studies were carried out using dedicated photon samples in a wide energy range and different detector configurations were also considered.

- **Chapter 6: Preliminary CRILIN prototypes tests**

  This chapter details the current development status of the Proto-0 and Proto-1 prototypes for the CRILIN calorimeter and presents the main results obtained from preliminary tests aimed at verifying their radiation resistance.

- **Chapter 7: CRILIN prototypes tests with electron beams**

  This chapter is devoted to the test beam conducted at CERN on the Proto-1 prototype in which I participated. The first part of the chapter presents in detail the experimental setup used and the second part presents the method with which I analyzed the data and the results obtained on the temporal resolution of CRILIN.

Chapter 1

Why a Muon Collider

High-energy muon collisions could open a new path to study physics beyond Standard Model by exploiting both the high-energy center of mass and the precision measurements achievable with that machine. The study of the facility and of the detector at $\sqrt{s} = 10$ TeV is in progress since this is uncharted territory. This chapter provides an overview of the Muon Collider project. It begins by discussing the main physics motivations that make a Muon Collider an attractive option for future high-energy experiments. Then, Section 1.2 is dedicated to the presentation of the proposed facility for muon beam production, cooling, and acceleration. Finally, Sections 1.3 and 1.4 describe the Machine-Detector Interface (MDI) and the Beam-Induced Background (BIB), which poses a significant challenge for the detector design and event reconstruction.

1.1 Physics cases

The Standard Model [4] represents the most advanced theory of our understanding of fundamental interactions of elementary particles. However, there are still many critical questions currently unanswered. These include, for example, the nature of the electroweak symmetry breaking and the origin of its energy scale. In 2012 the Higgs boson was discovered, however, it is not known whether the nature of this particle corresponds to the one predicted by the Standard Model. Additionally, the relationship between the physics described by the Standard Model and phenomena such as dark matter, the observed matter-antimatter asymmetry in the universe, and the hierarchy of the elementary particles remain open areas of investigation.

High-energy muon collisions offer the possibility to reach high center-of-mass energy with high luminosity as it will be explained in 1.2, and to perform high precision measurements since muons are elementary particles. This is an advantage compared to the proton interactions where collisions occur between their constituents, quarks and gluons, reducing the effective center-of-mass energy and giving more complex events to reconstruct.

Comparison of the production cross-section at proton and muon colliders for $2 \to 2$ and $2 \to 1$ can be found in [5] [6] to have an idea of the most appropriate machine to reach high energy. A fair comparison is very difficult because in addition to the fundamental physics, the characteristics of both machines should be taken into consideration.

Particle production can proceed via $s-$channel $\mu^+\mu^-$ annihilation. Here, heavy particles of mass M, with maximum $M = \sqrt{s}/2$, can be produced. The limit on the mass of new heavy particles can be extended beyond the kinematical limit by studying events properties as shown in [7].

1.1.1 Higgs studies at Muon Collider

Through the Higgs mechanism [8], the Higgs field interacts with elementary particles, giving mass to them while leaving massless particles, like photons and gluons, unaffected. The experimental results obtained so far by CMS [9] and ATLAS [10] experiments confirm the Standard Model expectations, therefore it is of paramount importance the precise determination of the Higgs boson properties. Multi-TeV muon collisions represent the ideal tool to study in detail the Higgs boson properties. In fact, the cross sections of the most important production channels reaches increase significantly for $\sqrt{s}$ above a few TeV, as shown in figure 1.1

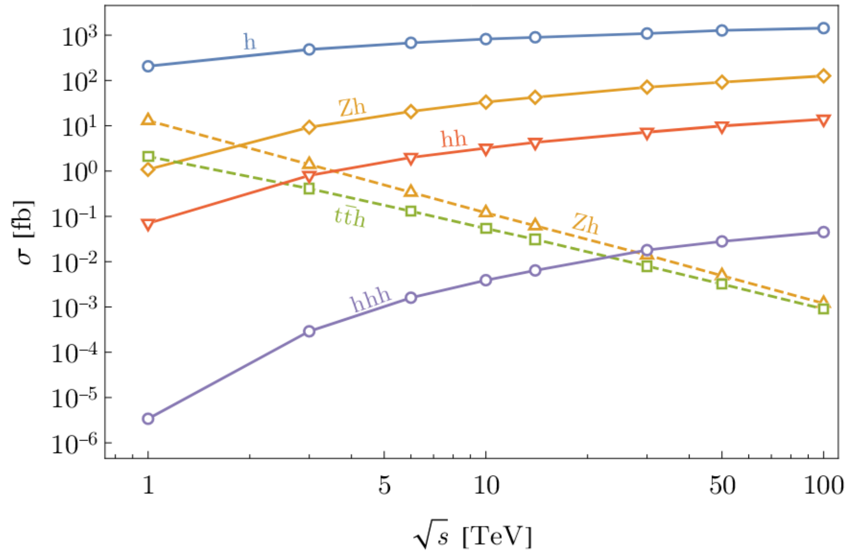

Figure 1.1: Cross sections of the most relevant Higgs boson production channels as a function of the muon collider center-of-mass energy [11].

At a $\sqrt{s} = 10$ TeV with a dataset of 10 ab^{-1}, about 9.3 million of single Higgs bosons and a sample of about 38000 double-Higgs events are expected.

The estimation of the precision on the Higgs boson cross sections in several final states has been performed at $\sqrt{s} = 3$ TeV by using a detailed detector simulation and including all the background contributions. In [12] and [13] a complete description of the analysis and the results can be found, here only a summary is provided. The statistical sensitivity on the production cross sections multiplied by the decay branching ratios: $\sigma_H \times BR(H \to f)$ with $f = b\bar{b}, WW^*, ZZ^*, \gamma\gamma$, and $\mu^+\mu^-$ has been evaluated. Here, the summary for each decay channel for an integrated luminosity of 1 ab^{-1}.

- $H \to b\bar{b}$: the final state with $2b$-jets is reconstructed by requiring two central($|\eta| < 2.5$), high momentum ($p_T^{jet} > 40$ GeV) jets. The requirement that both jets are identified as generated by b quark eliminates the major part of the physics background, the only contribution comes from $Z^0 \to b\bar{b}$. Higgs and Z^0 signal are statistically separated. The precision on $\sigma_H \times BR(H \to b\bar{b})$ is 0.75% .
- $H \to WW^*$: the final state is reconstructed in $qq^{'}\mu\nu_\mu$ to have a good signal-to-background ratio. Two central jets with $p_T^{jet} > 20$ GeV and a muon with $p_T^{\mu} > 10$ GeV still central are required. The precision on the cross section times the branching ratio for the final state is 2.9%.
- $H \to ZZ^*$: $q\bar{q}\mu^+\mu^-$ is used to reconstruct this process. At least two oppositely charged central muons with $p_T^{\mu} > 10$ GeV and two jets with $p_T^{jet} > 15$ GeV are selected. The precision on the cross section times the branching ratio is 17%.
- $H \to \gamma\gamma$: This process has a low branching ratio but it is very clean, this is the reason

why it is so important at LHC. At Muon Collider, it is less relevant but still important to measure the coupling. With the 3 TeV center-of-mass energy detector and the analysis described in [13] the precision on $\sigma_H \times BR(H \to \gamma\gamma)$ is 7.6%

- $H \to \mu^+\mu^-$: two oppositely charged muon in the central region with $p_T^\mu > 5$ GeV are required. The relatively low branching ratio of this decay limits the number of events produced. The precision on $\sigma_H \times BR(H \to \mu^+\mu^-)$ is 38%

The precise determination of $\sigma_H \times BR(H \to f)$ is needed to extract the precision to which it is possible to measure the Higgs boson couplings to fermions and bosons. This is done following a procedure referred to as global fit in the so-called k-framework [14], and it needs the determination of the cross section times the branching ratio for almost all the decay channel. Since that is not available, the parametric studies are used [15] with the detailed evaluations previously described taken as benchmarks.

Figure 1.2 shows the estimated precision on the couplings in the $k-$framework for muon collisions at $\sqrt{s} = 3$ TeV (in blue) and $\sqrt{s} = 10$ TeV (in red) with an integrated luminosity of 1 ab^{-1} and 10 ab^{-1} respectively. The dark-colored histograms are obtained by combining muon collider expectations with the HL-LHC estimates, in the assumption that there are no Beyond Standard Model decays of the Higgs boson.

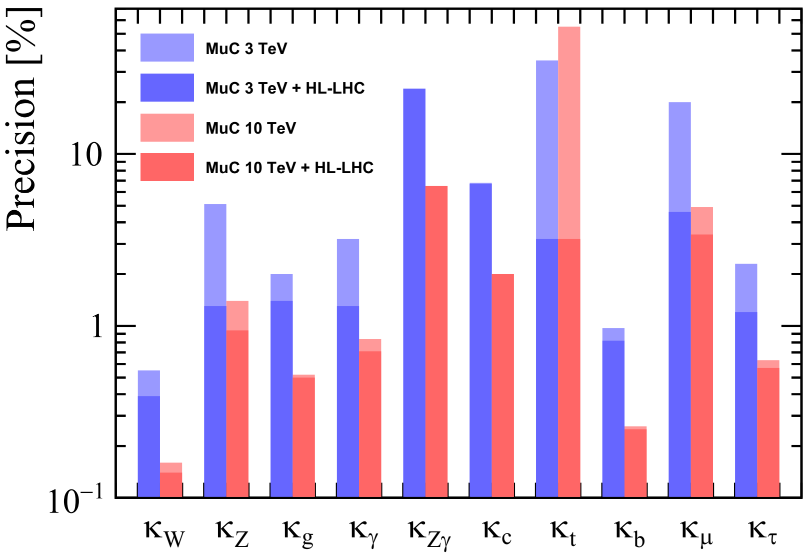

Figure 1.2: Precision on the Higgs boson couplings at a 3 TeV and 10 TeV muon collider. The light-colored histograms indicate the expected precision of Muon Collider alone, while the dark-colored ones show the precision when combining them with the HL-LHC. [12]

1.2 Muon accelerator complex

Being approximately 200 times more massive than electrons, muons can be accelerated in a circular collider with negligible synchrotron radiation losses up to tens of TeV. This allows the reach of much higher energies than electron-positron colliders.
Reduced radiation losses also enable tighter beam focusing, leading to the possibility of reaching a higher luminosity. This quantity defines the number of interactions that occur between the particles of the colliding beams per unit of time and surface area and together with the center of mass energy, represents a fundamental parameter to describe the potential of a collier. At the same time, it is one of the crucial ingredients for measuring the production cross sections of processes of interest.
In Figure 1.3, the luminosity, normalized to beam power, for a Muon Collider (blue line) is

compared with that of the Compact Linear Collider (CLIC) [16], a proposed linear e^+e^- collider (red line). Normalizing luminosity to beam power allows a direct comparison of how effectively different colliders employ their energy to achieve high interaction rates. The Muon Collider exhibits a nearly linear increase in luminosity, as a function of the center-of-mass energy. This feature allows the possibility to observe more frequently, and therefore study, rare production processes, which are often crucial for investigating key aspects of the standard model and are characterized by very small cross sections.

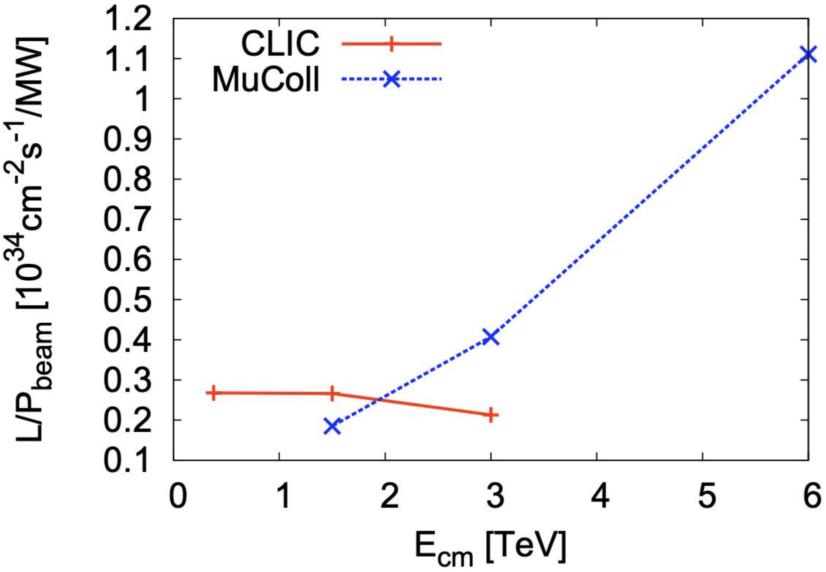

Figure 1.3: Luminosity normalized to the beam power values as a function of the energy of the center of mass: the blu line refers to the Muon Collider, the red line to the CLIC experiment. [17]

The construction of a Muon Collider accelerator presents numerous technological challenges. Achieving high luminosity requires the production of beams with high intensity, high collimation, and a short longitudinal size. Producing beams with these characteristics is particularly difficult for a Muon Collider due to the intrinsic properties of muons.

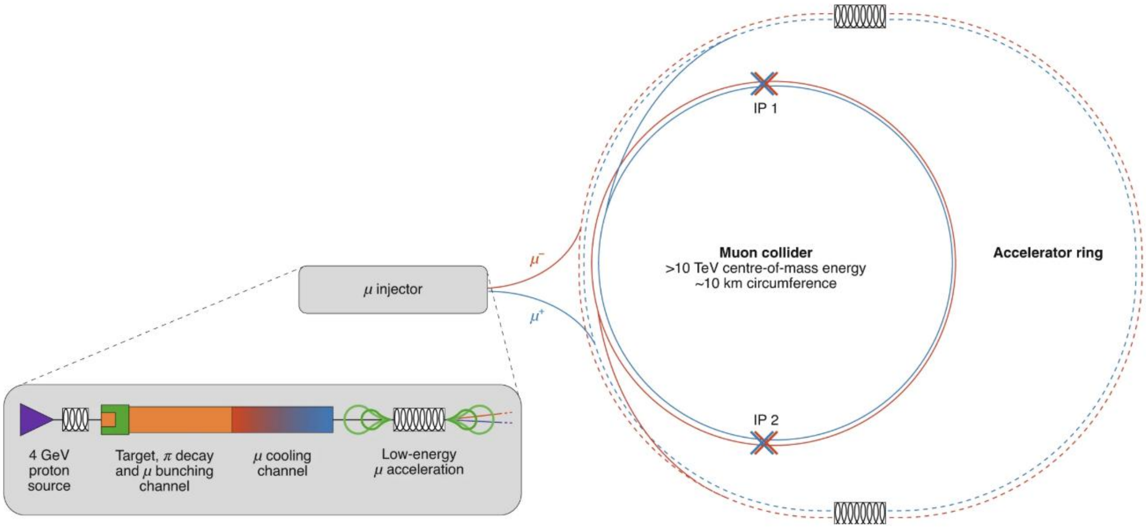

Figure 1.4: Complete scheme of the Muon Collider facility. On the right is illustrated the muon injector system, responsible for producing the muon and antimuon beams, that firstly enter inside the acceleration ring (larger in size) and finally in the collider ring (the smaller one). The locations of the interaction points are indicated with crosses.[18].

In Figure 1.4, the conceptual layout of the Muon Collider accelerator complex is illustrated.

The complex consists of three main components: the muon injector which generates the muon beams; an accelerator ring, where the μ^- and μ^+ beams are accelerated to higher energies; and a more compact collider ring, where the beams are brought into collision. This design involves the possibility of two interaction points (IP1 and IP2), where the position is indicated by the two crosses along the collider ring.

Following the scheme in Figure 1.4 the key steps involved in the muon collider facility are described below.

- **Muon production:** The technique for producing muon beams is based on protons bunches[1] impinging on a fixed high-Z target. The protons are delivered by a proton driver with energies ranging from 5 to 30 GeV. The bunches are produced with a compact length (RMS length of 1-3 ns) and a repetition rate of 15 Hz. The target material must be resistant to damage due to interactions with the bunches. Candidate materials under investigation include graphite and heavy liquid metal solutions. From the interaction of the protons on the target, charged pions with high transverse momentum are obtained. To efficiently capture these charged pions, the target is placed within a strong magnetic field (15-20 T) produced by a solenoid. Subsequently, the pions decay into muons.
- **Muon front-end:** The muons and antimuons obtained following the decay form a beam that is collected and in this section, a series of RF cavities operating at frequencies around 300-350 MHz divides the beam into packets (called bunches) of muons of both signs. The bunches then pass through a phase rotator section [19], which reduces the energy spread by decelerating higher-energy bunches and accelerating lower-energy ones. Finally, through the use of a magnet, the beam is separated into two lines relating to the contribution of μ^- and μ^+ respectively.
- **Muon cooling.** Muons emerging from the muon front-end system transport a large momentum spread, occupying a large phase space volume. It is crucial to reduce this phase space volume to achieve adequate luminosity for the collisions. This process is known as beam cooling. The current cooling techniques are not compatible with muon beams due to their short lifetime. A promising new technique is the Ionizing Cooling [20]. This technique involves passing the muon beam through a material, where the muons lose energy through ionization. They are then re-accelerated longitudinally to maintain the desired energy, effectively reducing the beam's transverse momentum and thus the phase space volume. This technique has been demonstrated to be a viable option by the Muon Ionization Cooling Experiment (MICE) [21].
- **Acceleration stage.** Following the cooling phase, the muon bunches undergo rapid acceleration. In the first stage, the beam is accelerated to an energy of 100 GeV using a combination of linear accelerators (linacs) and recirculating linacs accelerators (RLAs) [22]. The second stage takes place in the acceleration ring, where the beam passes many times through Rapid-Cycling Synchrotrons (RCS)[23] or Fixed Field Alternating Gradient accelerators (FFA) [24], reaching the required energy (TeV range) for collision.
- **Collider** After the acceleration phase, the final step for the muon and antimuon bunches is to be injected into the collider ring. As shown in the figure, this ring is designed to be compact to maintain the highest possible luminosity. For the $\sqrt{s} = 10\ TeV$ phase, the proposed collider ring will have a circumference of approximately 10 km. It will be equipped with high-field bending magnets, providing a strong magnetic field of around 16 T to efficiently bend and contain the high-energy muon beams.

Due to the short lifetime of muons, the entire sequence of processes, starting with the muon production to the final bunch collision, must be completed in a very short time. This is crucial to

---

[1] A bunch refers to a group of particles that are very close together forming a package that travels as a single unit along the accelerator.

minimize the loss of muons due to decay and, in turn, to maintain high luminosity levels for the collider. Currently, studies within the IMCC have explored three center-of-mass energy scenarios for the Muon Collider: 1.5 TeV, 3 TeV, and, most recently, 10 TeV. Table 1.1 summarizes the key parameters of the facility for 10 TeV center of mass energy.

Luminosity	$20 \cdot 10^{34} cm^{-2} s^{-1}$
N_b	$1.8 \cdot 10^{12}$
Fill rate	5 Hz
β^*	1.5 mm
σ^*	0.9 μm
σ_z	1.5 mm
Lorentz factor	47322
ϵ_n	25 μm

Table 1.1: Main parameters relating to the $\sqrt{s} = 10\ TeV$ muon collider facility. [18]

The research and analysis conducted in my thesis are centered on the 10 TeV center-of-mass energy stage of the Muon Collider.

1.3 The Machine-Detector Interface

The decay of muons in flight along the accelerator ring produces high-momentum secondary particles, which interact with the machine's materials (such as the beam pipe and magnets), and generate an intense flux of tertiary particles. This flux is referred to as Beam-Induced Background (BIB) [25]. Specifically:

- Energetic electrons, produced along the collider ring as a result of muon decay, can emit synchrotron photons due to the presence of bending solenoid magnetic fields.
- The interaction of these electrons and synchrotron photons with the machine materials, such as the beam pipe, generates a large number of tertiary particles through electromagnetic showers. Furthermore, γ-nuclear interactions lead to the production of hadrons, while the Bethe-Heitler process [26] produces muons.
- This cascade of particles can further interact with the machine materials, ultimately resulting in an intense flux of various particle types.

The presence of BIB particles has profound implications both on the machine and the detector. Two aspects are particularly important:

- **Damage to Machine components:** The flux of BIB along the accelerator ring can damage sensitive elements of the machine. For example, in the case of superconducting magnets, exposure to radiation from BIB particles can lead to quenching effects by degrading the properties of the superconducting materials or can overload the cryogenic system required to maintain the magnets at low temperatures. The implementation of dedicated protection systems is therefore necessary to safeguard the correct functioning of the machine.
- **Interference with detector operations:** Particles from the BIB, if not adequately mitigated, can enter the detector region, making very challenging the reconstruction of the events resulting from muon beam collisions. Indeed the high rate of background particles can overwhelm the detector, compromising the precision and accuracy of the experimental data. Furthermore, as will be explained in 2.6, the detector components are subject to doses of radiation that can damage some components.

In addition to the background induced by muon decay, the process of incoherent $e^+ e^-$ production [27] and the effect of the beam halo [28] are other significant sources of background at the

Muon Collider.
In particular, studies conducted by MAP at 1.5 TeV center-of-mass energy [29] indicate that the effects of the incoherent pair production process are almost negligible and the background is dominated by the muon decays. This is primarily due to the suppression of the cross-section at lower energies for this process, as well as the influence of the detector's magnetic field, which confines the e^- e^- pair around the beam pipe. While in the $\sqrt{s} = 10$ TeV scenario, the pair production process becomes more relevant and the resulting particles can affect mainly the first layers of the tracking system of the detector.

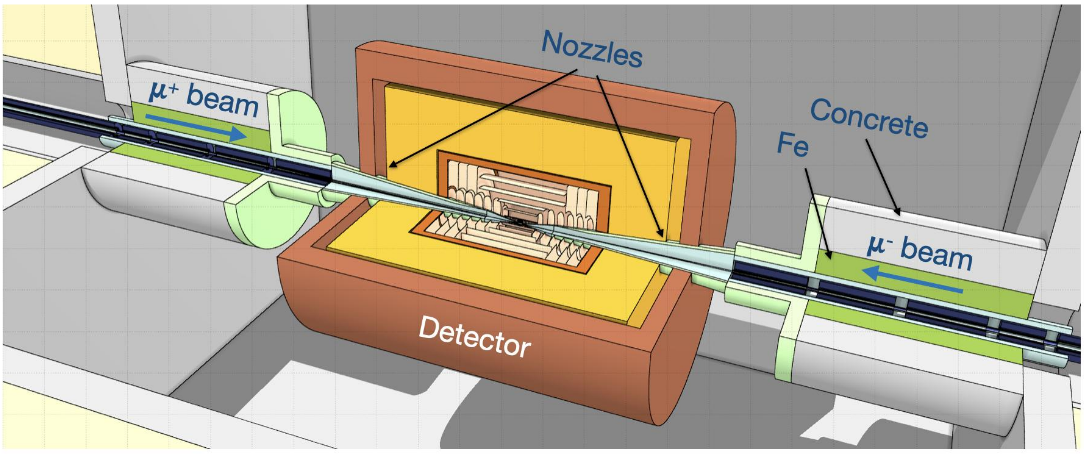

Figure 1.5: View along the beam axis of the interaction region of the Muon Collider. From left and right, the muon and antimuon beams enter the interaction region and collide at the interaction point, surrounded by the detector. The figure shows the pair of nozzles positioned around the beam pipe.

The Machine-Detector Interface (MDI) plays a crucial role in ensuring the optimal performance of the detector. Figure 1.5 illustrates a 3-dimensional view along the beam direction of the interaction region (IR), based on studies conducted by the MAP for a Muon Collider with a 1.5 TeV center-of-mass energy.
Referring to the figure, the description of the MDI can be carried out on the basis of two distinct areas from right to left along the beam axis:

1. Starting from the region furthest from the interaction point (IP), it is possible to see the beam pipe entering the IR. In the figure, the black arrow indicates the direction of the incoming μ^- beam towards the interaction point (IP). The beam pipe is encased in a first layer of iron (colored green) and concrete (colored gray). The black boxes along the beam pipe represent 11 T quadrupoles, installed to perform the final focusing of the beam.

2. In the region closest to the IP, where z is less than 6 m, the beam enters the detector area, in the figure represented in red and yellow. Here, the beam pipe is housed within a pair of tungsten cones called nozzles [18]. These structures, play a crucial role in absorbing particle backgrounds generated by the decay of muons in the beam. Figure 1.6 illustrates the geometric structure of the nozzles and specifies the materials used in their construction. The outermost region of the nozzles, extending from 100 cm to 6 m from the interaction point, has a reduced opening angle of 5° to optimize the detector's acceptance in the forward region. This section of the nozzles is covered by an outer layer of borated polyethylene. The section closest to the interaction point includes the tip, which features an opening angle of 10°. The right panel details the geometric configuration of the tip and its integration with the beam pipe. The distance between the tips of the two nozzles is 6 cm.

The design presented above is the result of an optimization process for muon interactions at a center-of-mass energy of 1.5 TeV. Specifically, the choice to use a high-Z material like tungsten allows for the efficient absorption of the electromagnetic component of the BIB. This effect

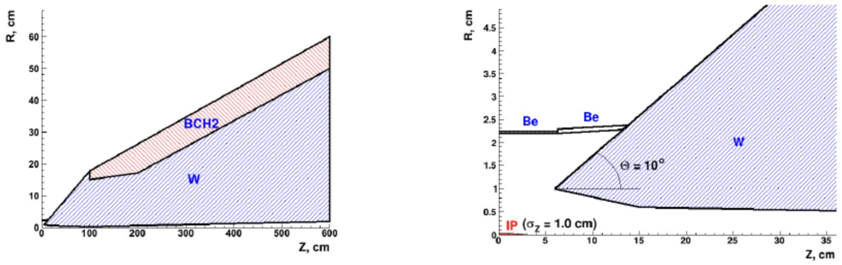

Figure 1.6: Geometric structure of the entire nozzle (left) and detail of the tip (right).[25]

is further enhanced by the presence of the magnetic field inside the detector region which, by deflecting the trajectory of the charged BIB particles, increases the possibility of their absorption and preventing the propagation into the detector.
Additionally, a layer of borated polyethylene was placed to absorb the neutron component of the BIB, which is generated from the interaction of BIB particles with the material of the nozzles. However, this solution has a side effect: it generates photons that can propagate into the detector region and affect the operation of the electromagnetic calorimeter.

1.4 Background characterization in the detector region

Given the profound impact on the operation of the detector, the BIB has been investigated in depth with dedicated simulation studies. The initial studies were conducted using the Monte Carlo generator software MARS15 [30], with a center-of-mass energy of 1.5 TeV [31]. Subsequently, studies conducted by the IMCC utilized the multiparticle transport code FLUKA [32], investigating the energy cases at $\sqrt{s}$ = 1.5, 3, and 10 TeV.
The procedure to generate background samples with the FLUKA program follows the procedure here described.

- The geometric structure of the IR, including the nozzles and the magnetic field generated by the detector along with the collider optics, is modeled by using the LineBuilder package [33].
- The components of the collider are defined in the FLUKA Elements Database [34].
- The simulation of the primary beam begins at a certain distance, from the IP. This distance is selected based on the center-of-mass energy and corresponds to the location along the beam pipe where the cumulative number of particles exiting the machine fully saturates those arriving in the detector region.
- The contributions of the BIB particles exiting the MDI and entering the detector region are carefully recorded. In this way it is possible to obtain the information regarding the position, time, energy and typology of each individual BIB particle entering in the detector region. This allows the subsequent simulation of the effects of BIB particles with the detector elements. This process is explained in detail in Chapter 3.

Table 1.2 compares the multiplicities of different types of particles that constitute the BIB as they exit the MDI and enter the detector region, obtained from studies at different center-of-mass energies.
Firstly, it is observed that the results obtained for the center of mass energy of 1.5 TeV with FLUKA and MARS15 are in good agreement. This result provide confidence in the robustness and reliability of the simulation procedure.
Furthermore, the results in the table shows a substantial independence of the multiplicities with respect to the beam energy. This aspect indicates that the number of the BIB particles entering the detector region is primarily influenced by the nozzles. Optimization studies on the design

Monte Carlo generator	MARS15	FLUKA	FLUKA	FLUKA
Beam energy [GeV]	750	750	1500	5000
μ decay length [m]	$46.7 \cdot 10^5$	$46.7 \cdot 10^5$	$93.5 \cdot 10^5$	$311.7 \cdot 10^5$
μ decay/m/bunch	$4.3 \cdot 10^5$	$4.3 \cdot 10^5$	$2.1 \cdot 10^5$	$0.64 \cdot 10^5$
Photons ($E_\gamma > 0.1$ MeV)	$86 \cdot 10^6$	$51 \cdot 10^6$	$70 \cdot 10^6$	$107 \cdot 10^6$
Neutrons ($E_n > 1$ MeV)	$76 \cdot 10^6$	$110 \cdot 10^6$	$91 \cdot 10^6$	$101 \cdot 10^6$
Electron/positrons ($E_{e^\pm} > 0.1$ MeV)	$0.75 \cdot 10^6$	$0.86 \cdot 10^6$	$1.1 \cdot 10^6$	$0.92 \cdot 10^6$
Charged hadrons ($E_{h^\pm} > 0.1$ MeV)	$0.032 \cdot 10^6$	$0.017 \cdot 10^6$	$0.020 \cdot 10^6$	$0.044 \cdot 10^6$
Muons ($E_{\mu^\pm} > 0.1$ MeV)	$0.0015 \cdot 10^6$	$0.0031 \cdot 10^6$	$0.0033 \cdot 10^6$	$0.0048 \cdot 10^6$

Table 1.2: Comparison of the multiplicities values of the BIB contribution generated with MARS15 Monte Carlo generator at $\sqrt{s} = 1.5$ TeV and with FLUKA at $\sqrt{s} = 1.5$, 3, and 10 TeV. [18]

and materials of the nozzles and the interaction region are currently ongoing in order to further mitigate the BIB flux.

As can be seen from the results in the Table 1.2, the most relevant BIB contributions entering the detector region come mainly from neutrons, photons, and electrons/positrons, while charged hadrons and muons show lower multiplicity values.
The comparison between the results obtained with the simulation of the IR at the center of mass energy of 3 TeV and 10 TeV are shown in Figure 1.7 and Figure 1.8.
Figure 1.7 shows the energy distribution of BIB particles entering the detector, it is possible to notice that they are characterized by a low energy spectrum. Figure 1.8 displays the arrival time of BIB particles in the detector region presenting a broad distribution with respect to the bunch crossing time set at t≈ 0. These two characteristics are due to the nozzles in the MDI, and the fact that they are very similar is an additional demonstration that the absorbers dominate the characteristics of the particles arriving into the detector.

For the study of my thesis project, I used a BIB sample generated with FLUKA at a center-of-mass energy of 10 TeV.

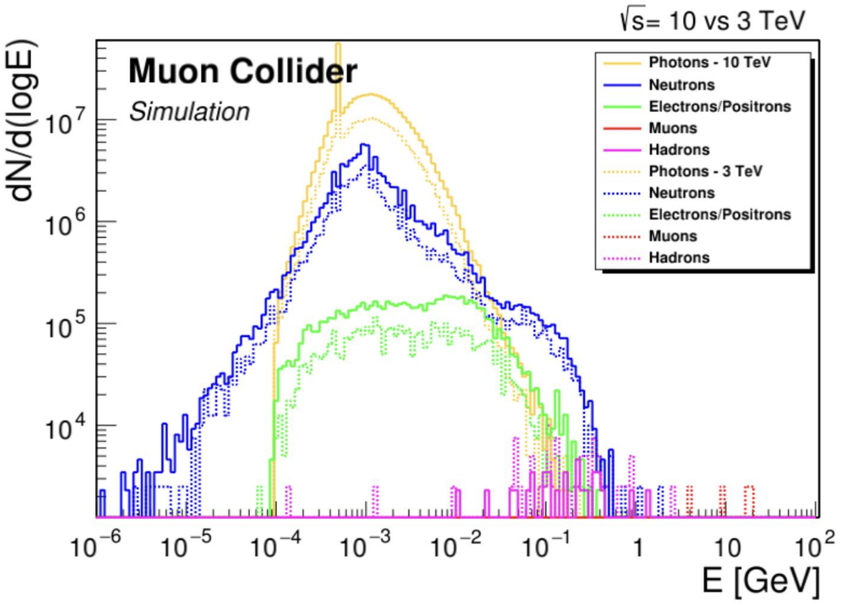

Figure 1.7: Energy distribution of the various BIB contributions entering the detector region, comparing the $\sqrt{s} = 3$ TeV case (dashed line) with the $\sqrt{s} = 10$ TeV case (solid line). The colours of the lines refer to the different contributions of the BIB and are specified in the legend.[12]

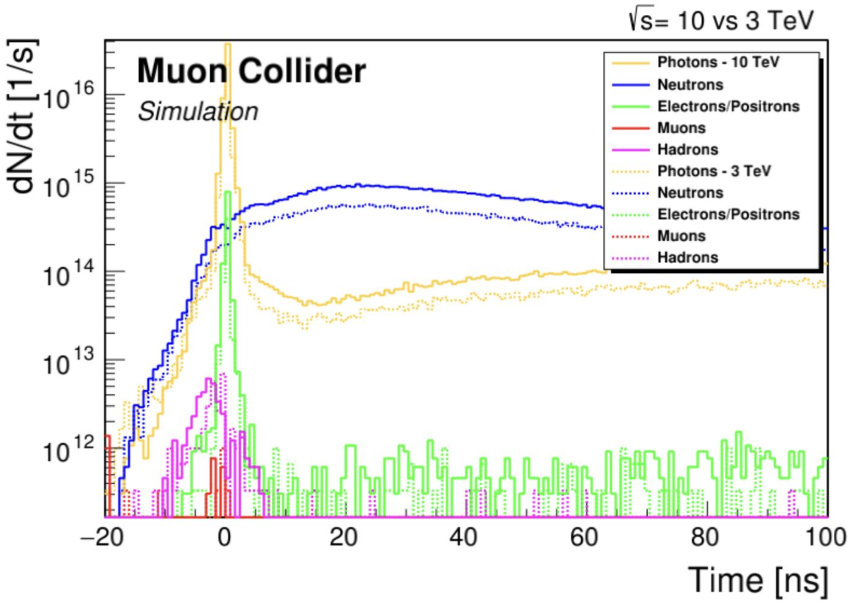

Figure 1.8: Arrival time distribution of the various BIB contributions entering the detector region, comparing the $\sqrt{s} = 3$ TeV case (dashed line) with the $\sqrt{s} = 10$ TeV case (solid line). The colours of the lines refer to the different contributions of the BIB and are specified in the legend.[12].

Chapter 2

Detector description

This Chapter focuses on the design concept of the detector to be used to study $\sqrt{s} = 10$ TeV muon collisions, referred to as MUSIC (MUon detector System for Interesting Collisions). As discussed in 1.4, the presence of BIB has profound implications in the reconstruction of muon collision events. Therefore, to achieve optimal detector performance in terms of resolution, efficiency, and precision, it is crucial to mitigate as much as possible the effects of BIB. In this Chapter, the components that constitute the detector layout are described.

2.1 Overview of the detector

The detector proposed for the Muon Collider experiment follows a classical cylindrical shape and hermetic geometry typical for multipurpose detectors of symmetric collisions. The detector design proposed for $\sqrt{s} = 3$ TeV collisions [35] was derived from the CLIC detector concept [36], with the key modification represented by the inclusion of nozzle cones in the forward and backward regions. This change required significant adjustments to the geometry of several subdetectors to ensure compatibility with the updated forward and backward regions.

Detection of $\sqrt{s} = 10$ TeV muon collisions are foreseen with a different detector, optimized for the new environment. Figure 2.1 presents a general view of the detector layout, showing a transversal section along the beam axis. The origin of the spatial coordinates is set at the beam interaction point. Following the axis diagram in the figure, the z-axis is aligned parallel to the beam pipe oriented with the direction of the μ^+ beam; the y-axis is oriented parallel to the direction of gravitational acceleration; the x-axis is defined as perpendicular to both the y and z axes, and is oriented in such a way that the coordinate system forms a right-handed set of axes. In the following discussion, spherical coordinates (R, θ, ϕ) will be used. In this system, R indicates the radial distance from the interaction point, θ is the polar angle relative to the beam axis (z-axis), and ϕ is the azimuthal angle in the x-y plane.

The global dimensions of the detector are 5.9 meters long and 6.8 meters in diameter. As shown in Figure 2.1, from the inside out, the detector is formed by the following subsystems:

- vertex (VTX) and tracker (TD) detector;
- electromagnetic calorimeter (ECAL);
- superconducting solenoid which provides a magnetic field of 5 T;
- hadronic calorimeter (HCAL);
- iron joke instrumented with a resistive plate chamber for the muons.

The configuration used in this thesis does not represent the final design for the $\sqrt{s} = 10\ TeV$ detector, as it is under optimization. In particular, the tracking system's design is undergoing significant development. However, this does not have major implications on the presented ECAL studies.

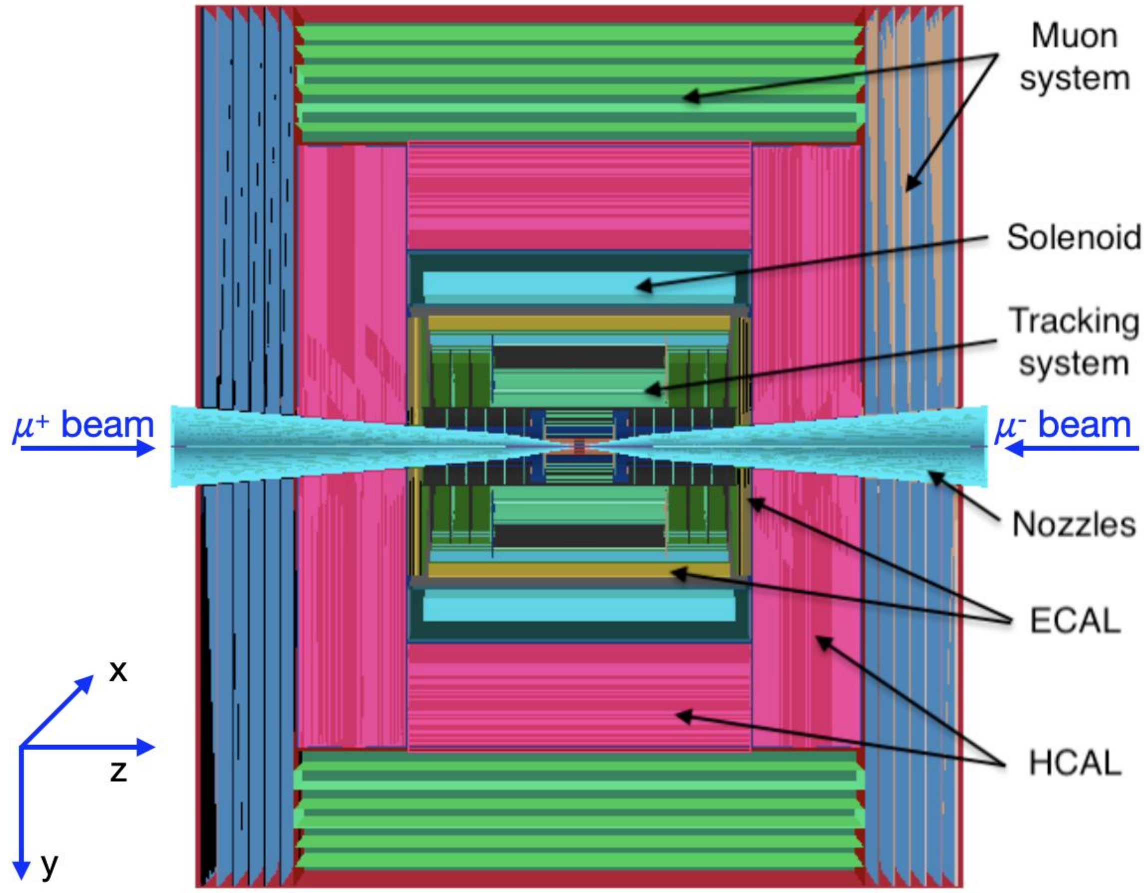

Figure 2.1: View of the longitudinal section along the beam axis of the MUSIC detector proposal. The sub-detectors are visible, identified by the different colors in the Figure. In the forward region with the blue colour, the nozzles are visible.

2.2 The Tracking system

The tracking system is composed og the following elements: a vertex detector (VXD), positioned closest to the interaction point, followed by an inner tracker (IT) and an outer tracker detector (OT).

The structure of the vertex and tracker detector follows the overall symmetry of the detector and it is divided into two components: barrel and endcap. As visible in Figure 2.1, the barrels cover the central part of the detector and consist of cylindrical layers with their symmetry axis aligned with the beam pipe at different radii. The endcaps cover the two forward regions of the detector and are formed by disks placed along the x-y plane and centered on the z-axis, positioned at variable distances from the interaction point and with different radii. In Figure 2.2, the layout of the layers for the tracking system is shown: the vertex detector is indicated in red, the inner tracker in blue, and the outer tracker detector in green.

2.2.1 Vertex detector

The vertex detector is crucial for reconstructing the impact parameter of tracks with high precision, which is essential for identifying secondary vertices. Additionally, it plays a significant role in accurately identifying primary vertices. For this reason, it must be positioned very close to the interaction point and it is the first sub-detector that particles encounter.

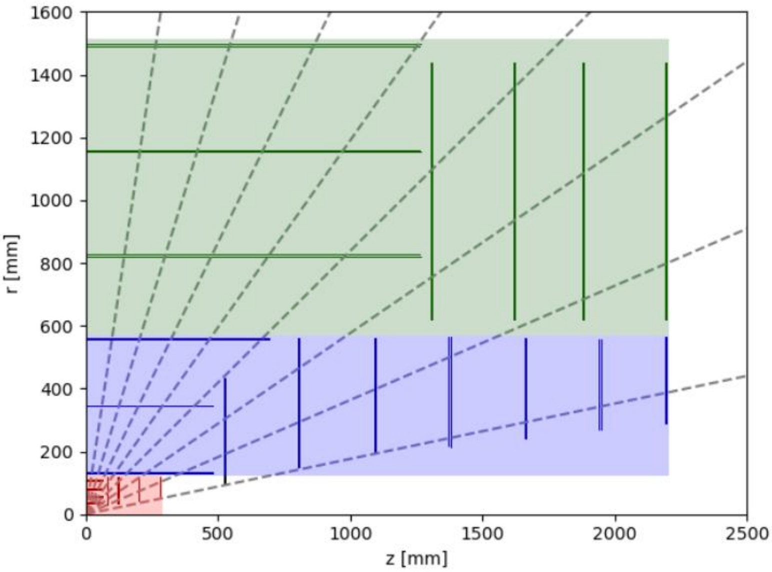

Figure 2.2: A schematic view of the layer arrangement for the tracking system along the Z-R plane. The horizontal lines represent the barrel layers, while the vertical lines indicate the endcap layers. The red color represents the vertex detector, blue denotes the inner tracker, and green the outer tracker.[35]

Figure 2.3 (left) illustrates a schematic layout of the barrel layers in the transverse (x-y) plane, aligned with the beam axis. The VTX detector is composed of a double-layer structure made up of silicon sensors, with a 2 mm gap between each layer. As shown in Figure 2.3 (right), the barrel region consists of four sequentially arranged double layers at increasing radii, while the endcaps are formed by eight disks—four on each side of the detector. Tables 2.1 and 2.2 summarize the relative dimensions of the various layers in both the barrel and endcap regions respectively.

VTX layers are based on silicon pixel sensors with dimensions of 25μm x 25μm and a thickness of 50μm. This choice provides high granularity with a spatial resolution of 5μm x 5μm and a high temporal resolution of 30 ps. These characteristics allow the achievement of adequate performance in a region where the presence of BIB is particularly high.

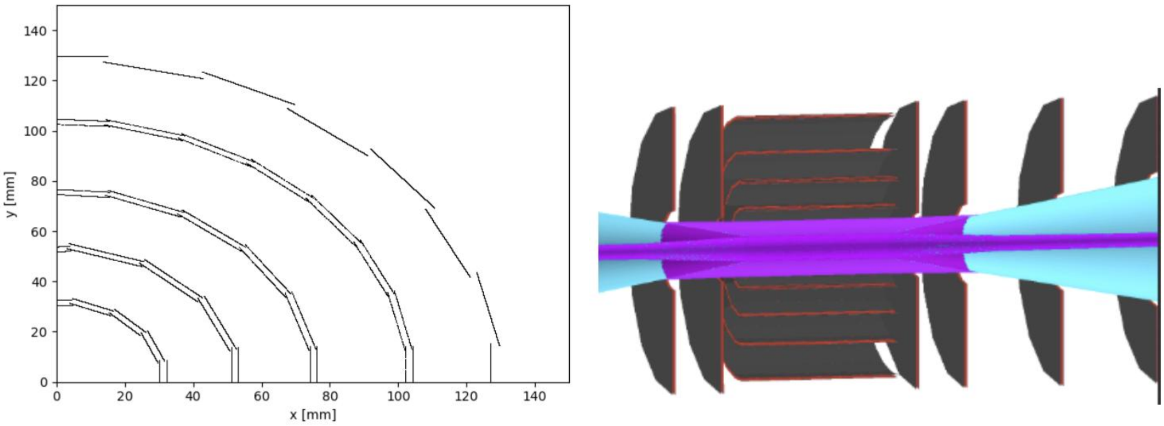

Figure 2.3: Right: A view along the transverse plane to the beam direction (x-y plane) shows the composition of the barrel layers of the vertex detector [35], clearly highlighting the double-layer structure. Left: A three-dimensional view of the vertex detector structure along the longitudinal plane relative to the beam axis.

Barrel	Radius [cm]	N^o of staves
R_1	3	16
R_2	5.1	15
R_3	7.4	21
R_4	10.2	29

Table 2.1: Radius values for each layer of the vertex detector at the barrel. The third column also specifies the number of staves that form each layer.

Endcap	$\|\Delta z\|$ [cm]	R_{min} [cm]	R_{max} [cm]
$\|\Delta z_1\|$	8	2.2	11.2
$\|\Delta z_2\|$	12	2.8	11.2
$\|\Delta z_3\|$	20	3.5	11.2
$\|\Delta z_4\|$	28	5	11.2

Table 2.2: Geometric values specifying the dimensions of each endcap disk of the vertex detector in terms of the inner and outer radius, and their position along the z-coordinate (Δz) respect the interaction point.

2.2.2 Inner and Outer Tracker detector

Figure 2.4 shows a 3D rendering of the tracking detector (TD), IT, and OT where the arrangement of the barrel layers and the endcap disks can be appreciated. Like the vertex detector, the TD structure is based on layers of silicon sensors.

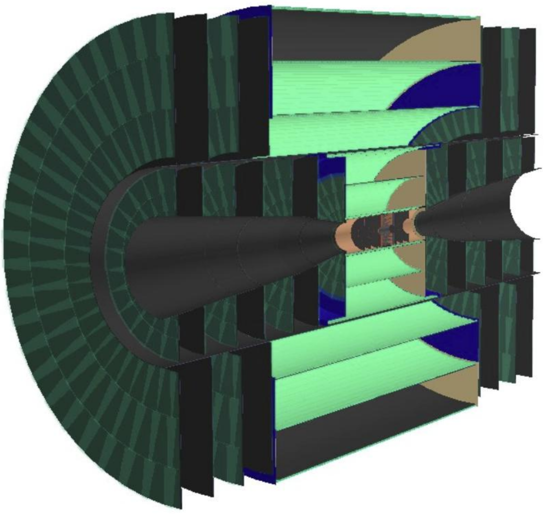

Figure 2.4: Three-dimensional view of the longitudinal section of the complete tracker system along the y-z plane. The inner tracker occupies the central region, encircled by the outer tracker layers.[37]

Inner Tracker

The inner tracker is structured as follows:

- The barrel consists of three cylindrical-shape layers with the relative geometric specifications summarized in Table 2.3. Layers are instrumented with silicon macro-pixel sensors, oriented along the beam axis, with dimensions of 50 $\mu m \times 1 mm$ and a thickness of 100 μm.
- The endcaps consist of 14 disks, symmetrically arranged with 7 on each side of the detector. Each disk has a different position along the z-axis and varying values for the inner radius R_{min} and outer radius R_{max}. The geometric specifications are summarized in Table 2.4.

The innermost disk is equipped with silicon pixels measuring $25\mu m \times 25\mu m$ and a thickness of $100\mu m$, while the remaining disks are instrumented with silicon strips measuring $50\mu m \times 1mm$, oriented radially with respect to the center of the disk.

Barrel	Radius [cm]	Half length [cm]	N^o staves
R_1	12.7	48.2	28
R_2	34.0	48.2	76
R_3	55.4	69.2	124

Table 2.3: Geometric specifications of the Inner Tracker barrel layers.

Endcap	$\|\Delta z\|$ [cm]	R_{min} [cm]	R_{max} [cm]
$\|\Delta z_1\|$	52.4	9.5	42.7
$\|\Delta z_2\|$	80.8	14.7	55.8
$\|\Delta z_3\|$	109.3	19.0	55.6
$\|\Delta z_4\|$	137.7	21.2	56.1
$\|\Delta z_5\|$	166.1	23.7	55.7
$\|\Delta z_6\|$	194.6	26.4	55.4
$\|\Delta z_7\|$	219.0	28.4	55.8

Table 2.4: Geometric specifications of the disks that form the endcaps of the Inner Tracker

Outer Tracker

The outer tracker has the structure described below:

- The barrel, as shown in Figure 2.2, is formed by three cylindrical layers, with the geometric characteristics presented in Table 2.5. The layers are equipped with silicon strip sensors of larger dimensions: $50\ \mu m \times 10mm$ and a thickness of $100\ \mu m$. The strips are oriented along the beam axis.
- The endcap consists of 8 disks, with 4 of them on each side. Table 2.6 lists the positions along the z-axis and the inner and outer radii of each disk. Each disk is divided into 48 modules, and the sensors used are silicon strips with dimensions of $50\ \mu m \times 10mm$ and a thickness of $100\ \mu m$. Similar to the inner tracker endcaps, the strips in the outer tracker endcaps are oriented radially.

Barrel	Radius [cm]	Half length [cm]	Num. staves
R_1	81.9	126.4	184
R_2	115.3	126.4	256
R_3	148.6	126.4	328

Table 2.5: Geometric specifications of the Outer Tracker barrel layers

.

Endcap	$\|\Delta z\|$ [cm]	R_{min} [cm]	R_{max} [cm]
$\|\Delta z_1\|$	131.0	61.7	143.0
$\|\Delta z_2\|$	161.7	61.7	143.0
$\|\Delta z_3\|$	188.3	61.7	143.0
$\|\Delta z_4\|$	219.0	61.7	143.0

Table 2.6: Geometric specifications of the disks that form the endcaps of the Outer Tracker.

	Vertex Detector	Inner Tracker	Outer Tracker
Cell Type	pixels	macro-pixels	micro-strips
Cell Size	$25\ \mu m \times 25 \mu m$	$50 \mu m \times 1 mm$	$50 \mu m \times 10 mm$
Sensor Thickness	$50\ \mu m$	$100\ \mu m$	$100\ \mu m$
Time Resolution	30 ps	60 ps	60 ps
Spatial Resolution	$5 \mu m \times 5 \mu m$	$7 \mu m \times 90 \mu m$	$7 \mu m \times 90 \mu m$

Table 2.7: Size of the silicon sensors and characteristics in terms of time and spatial resolution for the three components of the tracking system.

2.3 Calorimetric system

The calorimetric system is divided into two parts: the Electromagnetic Calorimeter (ECAL) and the Hadronic Calorimeter (HCAL). In Figure 2.5, the ECAL is shown in yellow, the HCAL in blue, while the grey color represents the superconducting solenoid. Both subparts consist of a barrel component, which covers the central region of the detector, and endcap components with lateral disks symmetrically placed on both sides.

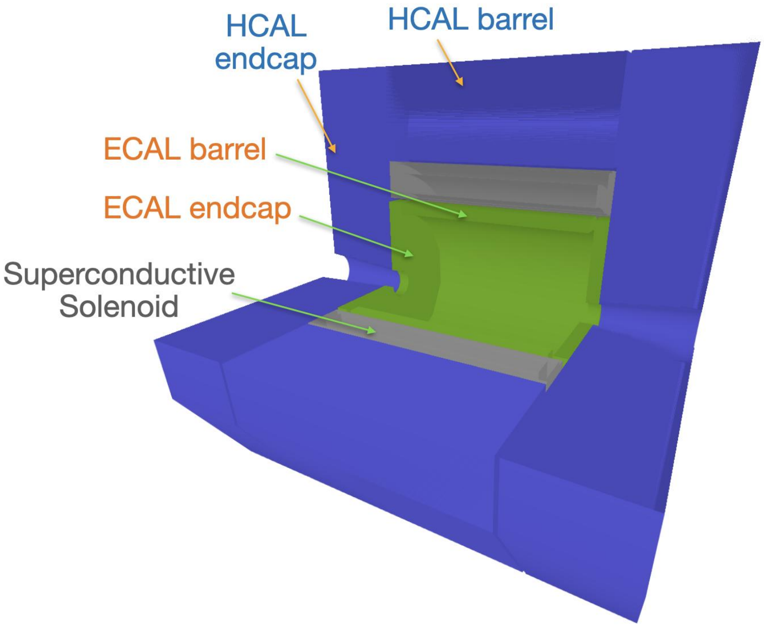

Figure 2.5: Three-dimensional view of the calorimeter system, including both the barrel and endcap regions. The ECAL is shown in yellow, while the HCAL is shown in blue. The superconducting solenoid, shown in gray, is located between the ECAL and the HCAL.

Electromagnetic calorimeter

The electromagnetic calorimeter is essential for measuring the energy of electromagnetic particles, such as electrons, positrons, and photons, by absorbing their energy and generating a corresponding signal. Furthermore, it provides essential information for identifying the various particles generated in the interaction events. As seen in Figure 2.1, the electromagnetic calorimeter is positioned immediately after the tracking system and within the superconducting solenoid. The ECAL has a dodecahedral shape in the barrel region, the forward regions of the detector are covered by two endcap disks. To adequately contain the energy deposited with the electromagnetic showers of very energetic objects produced in muon interaction events, the number of radiation lengths considered is equal to 25 X_0. Table 2.8 presents the geometric specifications of the volume occupied by the ECAL. A detailed description of the electromagnetic calorimeter is given in Chapter 4.

Barrel		**Endcap**	
R_{min} [cm]	160	R_{min} [cm]	31
R_{max} [cm]	196	R_{max} [cm]	196
Half-length [cm]	221	Δz [cm]	27

Table 2.8: ECAL barrel and endcap geometric specifications.

Hadronic calorimeter

The hadronic calorimeter plays a crucial role in measuring the energy of hadronic particles, such as protons and neutrons, for the study of jets produced by quarks. Located outside the magnetic field provided by the solenoid, it consists of a barrel with a dodecahedral shape and is enclosed on the sides by a pair of endcap disks as illustrated in Figure 2.5. The geometric characteristics of HCAL are summarized in Table 2.9.
The proposed technology for the hadronic calorimeter is based on a sampling calorimeter formed by 60 layers of interlaced layers of steel absorber with a thickness of 19 mm and plastic scintillating tiles, with 30 x 30 mm^2 size. The total thickness, both in the barrel and endcap regions, corresponds to 7.5 interaction lengths (λ_I). Including ECAL, this increases to 8.5 (λ_I).

Barrel		**Endcap**	
R_{min} [cm]	290.2	R_{min} [cm]	32
R_{max} [cm]	475.2	R_{max} [cm]	475.6
Half-length [cm]	250.9	Δz [cm]	185.5

Table 2.9: HCAL barrel and endcap geometric specifications

2.4 Superconductive solenoid

The superconducting solenoid is positioned between the electromagnetic calorimeter and the hadronic calorimeter as illustrated in Figure 2.5. It provides a very intense magnetic field, with a nominal value of 5 T inside, with a residual field evaluated to be around 1.88 T on the outer side of the solenoid. From a construction perspective, the solenoid is encased in a specialized vacuum tank made of 40 mm thick steel. The usage of Al-stabilized coils reinforced with superconducting wire is one possibility to build up a system able to generate such an intense magnetic field over a such large volume. An option for the superconducting wire is NbTi/Cu (niobium-titanium/copper), a technology well-known and used in the CMS experiment. The thickness of the coils is 423 mm and in Table 2.10 the geometric specifications are summarized.

Solenoid inner radius [cm]	205.5
Solenoid outer radius [cm]	286.2
Vacuum tank thickness [cm]	4.0
Solenoid half length [cm]	250.9
Coil thickness [cm]	42.3
Coil radius [cm]	239.3
Coil half length [cm]	228.0

Table 2.10: Geometric specifications of the superconductive solenoid as in the current version of the simulation.

2.5 Muon system

The muon system is the outermost component of the detector, as shown in Figure 2.1 where the barrel is represented in green and the endcap in blue. This subdetector is responsible for identifying muons and to characterize their properties. The design proposed for the muon system is represented by an iron yoke that allows closing the remaining flux lines of the magnetic field generated by the solenoid which are instrumented by different layers of muon detectors.

The current design contains Resistive Plate Chambers (RPCs) sensors. However, in the forward regions, this sensors are near the limit of their rate capability. Therefore, the next developments of the system will investigate the use of other sensors from different technologies to optimize global performance. In Table 2.11, the geometric dimensions occupied by the muon system are summarized.

Barrel		Endcap	
R_{min} [cm]	480.6	R_{min} [cm]	62.2
R_{max} [cm]	680.0	R_{max} [cm]	680.0
Half length [cm]	444.4	Δz [cm]	145.9

Table 2.11: Muon system barrel and endcap geometric specifications.

2.6 Radiation levels

The presence of BIB particles in the detector region can gradually damage the subsystems, affecting their performance and longevity. For this reason, during the development of the detector design, it is crucial to quantify the expected radiation dose levels. Figures 2.6 and 2.7 illustrate respectively the expected 1 MeV neutron equivalent fluence (1-MeV-neq) and the total ionising dose (TID) in the detector region as a function of the z coordinate and the radial distance r from the beam axis. These maps were obtained by considering the BIB generated by FLUKA at 1.5 TeV center-of-mass energy and a simplified model of the detector. The calorimetric system, solenoid, and iron yoke are simplified into a single cylindrical body whose density is the average of the materials of the individual components, while the tracking system remains unchanged.

The radiation dose is normalized by considering the maximum collision rate expected for the muon collider, which is 100 Hz (1 collision every 10 μs). Considering an annual data-taking period of 200 days, the 1-MeV-neq fluence is expected to be approximately $10^{14} - 10^{15}$ cm^{-2}y^{-1} in the region of the tracking detector and around 10^{14} cm^{-2}y^{-1} in the electromagnetic calorimeter. The total ionising dose is expected to be approximately 10^{-3} Grad/y in the tracking system and 10^{-4} Grad/y in the electromagnetic calorimeter. In both maps, a strong decrease in the expected dose after the calorimetric system is observed as most of the radiation has been absorbed.

The radiation dose levels expected for the Muon Collider at 1.5 TeV center-of-mass energy, if compared to the levels expected for the CMS and ATLAS detectors in LHC phase 2 at high luminosity, are lower. For example, considering the case of the CMS experiment, in the tracking system a total TID of or 1.2 Grad and a 1 MeV neutron equivalent fluence of up to $2.3x10^{16}neq/cm^2$ is expected [38]. This is an important fact that ensures that the radiation levels in the Muon Collider will be manageable already with the current technologies of the various detector components and, even more so, with future ones.

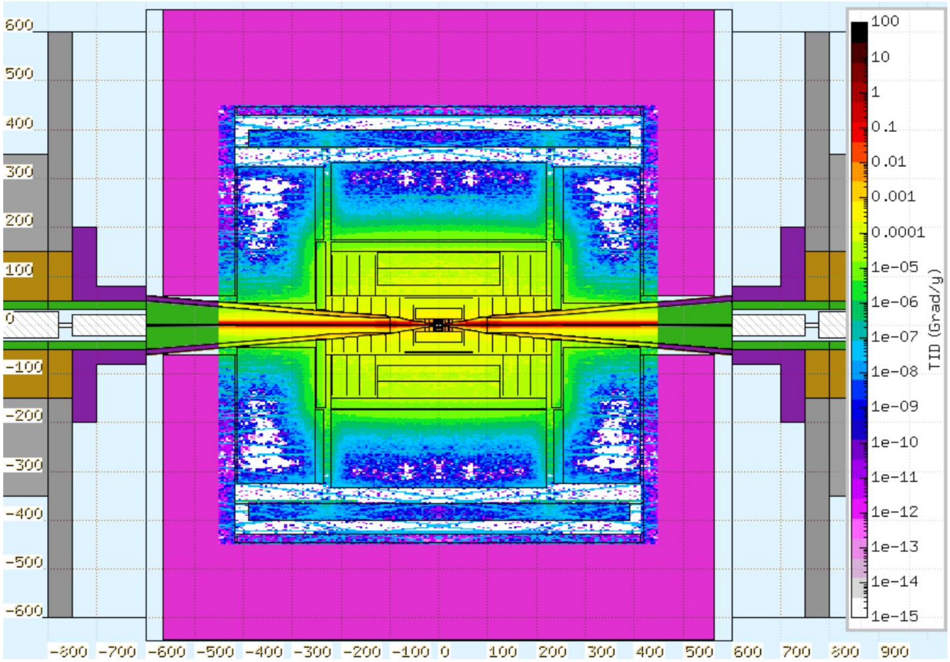

Figure 2.6: Map of the Total Ionizing Dose (TID) at the detector region corresponding to one year of data taking at a collision rate of 100kHz.[18]

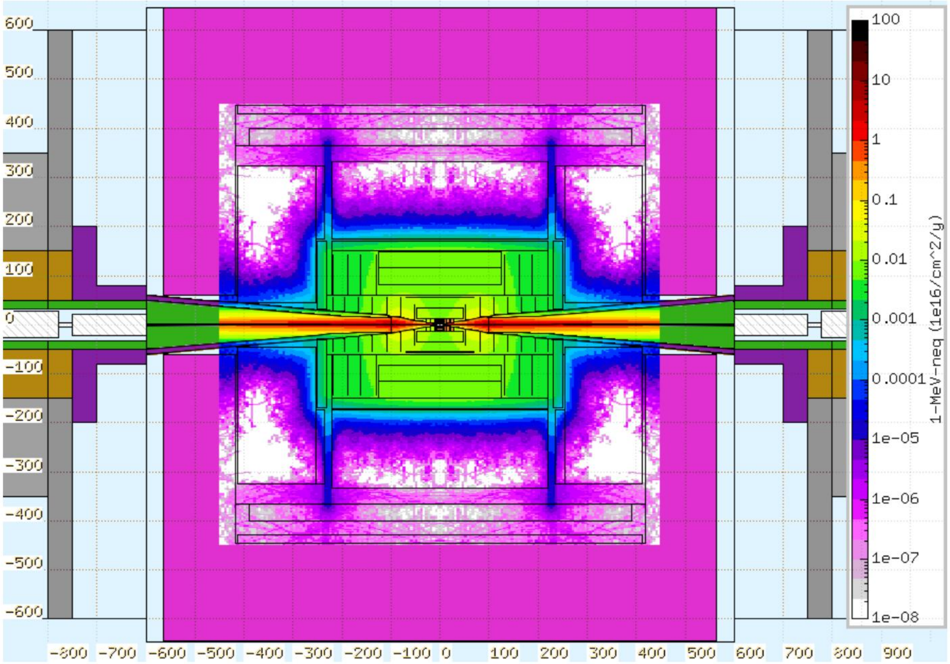

Figure 2.7: Map of the 1-MeV-neq fluence at the detector region corresponding to one year of data taking at a collision rate of 100kHz.[18]

Chapter 3

Detector simulation and physics objects reconstruction

Modern particle physics experiments demand increasingly high-performance detectors, which often leads to greater complexity in their design. In this context, simulation studies have become an indispensable tool to evaluate the most appropriate design choices, considering both geometry and technologies employed.
For a novel experiment like the Muon Collider, where the presence of a peculiar background like the BIB poses challenges never met before, simulation studies are even more critical. Through detailed simulations, it is possible to analyze the characteristics of the BIB and conduct fundamental studies for its mitigation.
This Chapter provides an overview of the simulation process, physics object reconstruction, and the software tools used in the studies conducted within the IMCC for the development of the Muon Collider detector. The different stages of the simulation process, from the generation of input particles to the reconstruction of their interactions within the detector will be illustrated.

3.1 Simulation procedure workflow

The complete simulation workflow comprises several steps. Starting with the generation of the initial input particles, a precise simulation of their interactions with the detector materials is performed, also reproducing the digitized response of the electronics of the various subsystems of the detector. After that, the physics objects are reconstructed by using dedicated software tools. The individual steps are described in detail below.

3.1.1 Events Generation

The first step of the simulation process is the generation of input particles at the Monte Carlo level. In this phase, different types of particle samples can be created:

- **Samples of $\mu^+\mu^-$ interactions** where the specific processes and final states can be selected, and the center-of-mass energy for the interaction is specified. In this thesis, the MadGraph software [39] was used as the Monte Carlo event generators. This tool allows the generation of hard collision events up to the Next-to-Leading Order (NLO) level in perturbation theory.

- **Samples of single particle events** can be generated at the interaction point. Using Python code, it is possible to generate particle samples of a given type with fixed energy and polar angle values or defined within a specified range, depending on the needs of the study. This scenario is often referred to as a “particle gun” approach, where the generated samples are particularly useful for the characterization of some detector subsystems, as discussed in Chapter 5.

- **BIB particles** are a further category of particle samples that are considered in the simulation studies of the Muon Collider. As anticipated in section 1.4, the Monte Carlo generators used to obtain the samples of BIB events are MARS15 and FLUKA.

3.1.2 Simulation

This simulation process is carried out within the ILCSoft framework [40], taking as input the generated particles along with the detailed geometry of the detector, which includes the specific components and the materials used. The description of the detector geometry is provided by DD4HEP software [41], a specific tool within the ILCSoft framework.

The interactions of the particles at the generator level with the detector's sensitive and passive materials are simulated using the GEANT4 toolkit [42]. The process generates hits, labeled SimHits in this thesis, which represent the energy deposits released by particles at specific spatial locations and times as they pass through the detector and interact with materials.

3.1.3 Digitization

The SimHits generated during the simulation step represent the pure interactions of the particles at generation level with the materials composing the detector. In the following step, the digitization procedure, the SimHits are taken as input and the simulation of the response of each detector component is processed considering the effect of the readout electronics. This procedure takes into account the characteristics of the individual subdetectors such as the spatial and temporal resolutions, the geometry, and also operational parameters such as signal integration time windows. At the end of this procedure, the collections of digitized hits for each subsystem of the detector are obtained, which in this thesis are called DigiHit.

Reflecting the different characteristics and functions of the various components of the detector, the digitization procedure presents different methods. In particular, in the context of the tracker system and the calorimeter system, the following procedures are applied:

- **Tracker digitization:** the digitization of SimHits in the tracking system actually does not represent true digitization and is currently at a preliminary stage. It primarily involves a Gaussian smearing procedure with respect to the spatial and time coordinates for each single SimHit from GEANT4 within the corresponding tracker layer. The Gaussian smearing is defined considering the temporal and spatial resolutions of the given layer and for each SimHit a corresponding DigiHit is generated without any clustering process.

  A more refined digitization procedure is currently under development, aiming to more accurately simulate the effects of the silicon sensors and include a clustering phase. At the same time, this improvement will reduce the number of DigiHits outputted, thereby lowering the computational time required for the reconstruction process.

  DigiHits are selected within a specific time window for each subsystem (VTX, IT, OT detectors), carefully configured to filter out the out-of-time component from the BIB and reproduce the finite readout time window of the electronics in a real detector.

- **Calorimeter digitization:** the digitazation procedure in the calorimetric system involves the sum of all the SimHits within a single calorimeter cell during a given acquisition time window. This summation results in the formation of a calorimetric DigiHit, to which spatial position, energy, and time are properly assigned.

  Specifically, the associated energy is determined by summing the energy deposits from the SimHits with energy greater than 2 MeV and the obtained result is then corrected by a factor that accounts for the fraction of charge collected within the signal integration time. The selected integration time window range is [-1, 25] ns.

  The time associated with the DigiHit is defined as the arrival time of the first SimHit

contributing to the corresponding DigiHit.
The acquisition time window is carefully selected to exclude the out-of-time component of the BIB, maximizing the signal-to-noise ratio. For further details on the selection of the acquisition time window, refer to Chapter 5.
The same procedure is apply also for the muon detector system.

Overlay of the BIB contribution

As shown in Figure 3.1, the generation and simulation phases of event samples (interactions or single particles) and BIB samples are performed separately. The Overlay procedure allows the combination of these two contributions before the start of the digitization phase. In this way, during the digitization phase, both contributions are processed together, thereby enabling the accurate reproduction of the experimental environment characteristic of the Muon Collider, including the presence of the BIB. Moreover, the advantage of this procedure is that it simplifies the computational process, allowing the simulation of the BIB sample only once and the usage of it for studies with different samples during the subsequent reconstruction phase.

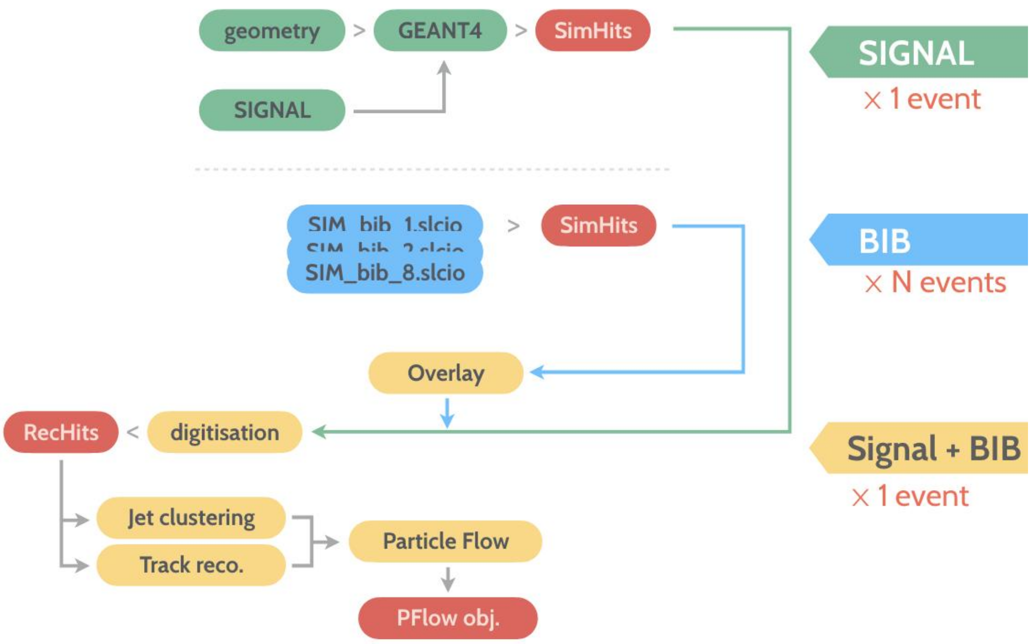

Figure 3.1: Scheme summarizing the main steps of the simulation workflow. At the top, in green, the steps from the particle sample at the generation level to the production of SimHits, following the simulation, are illustrated. Similarly, the processes for the BIB samples are represented in blue. At the bottom, in yellow, the process leading to the digitization and, finally, to the reconstruction of the particles is summarized.[43]

3.2 Event Reconstruction procedure

3.2.1 Charged particle reconstruction

In a particle detector, a track is the reconstructed trajectory of a charged particle as it passes through the active volume of the tracking detector. Track reconstruction is a key aspect of data analysis, as it provides crucial information about the properties of particles produced in collision events, including momentum, primary vertices, and particle identification (PID). Due to the presence of a uniform magnetic field in the detector, charged particles describe a helical trajectory, the curvature of which is inversely proportional to the transverse momentum of the particle. The main parameters describing a track, referred to the interaction point z_0 as the reference point, include:

- D_0: minimum distance between the track and the interaction point in the transverse plane respect the beam axis (z).
- Azimuthal angle ϕ: between the reference point with respect to the center of the helix.
- Z_0: represents the perpendicular distance between the helix path of the particle and the reference point, typically the origin, along the z-axis (the beam direction).
- Ω: the curvature of the track, which is inversely proportional to the transverse momentum of the particle.
- $tan(\lambda)$: is the tangent of the dip angle, which describes the angle between the particle's helix trajectory and the x-y plane (the plane perpendicular to the beam direction).

The DigiHits hits of the tracker system that pass the temporal selection cuts in the digitization phase, serve as input to the reconstruction algorithm, which allows the determination of the trajectories of the charged particles. Currently, within the IMCC framework, two reconstruction approaches have been considered: the Combinatorial Kalman Filter (CKF) and Conformal Tracking (CF) [44]. The CKF method was originally developed for the high-occupancy environment of hadronic colliders, where it is essential to manage a large number of hits. In contrast, the CF algorithm was designed for the e^+e^- colliders, where the experimental environment is much cleaner. In the current studies conducted by the IMCC, the CKF has been adopted. This choice is motivated by the fact that CFK can efficiently process a large number of hits in the tracking system due to the BIB. As shown in Figure 3.2, the average occupancy level for bunch crossings in the tracking system, due to BIB particles at $\sqrt{s} = 10$ TeV, is very high, especially in the first layers of the vertex detector, and then progressively decreases with the increase of the radial distance from the beam pipe. The figure also compares the occupancy levels without the application of an acquisition time window (in blue) and with the application of a time window between $[-3\sigma_t, 3\sigma_t]$ (in red), where $\sigma_t = 30$ ps for the vertex detector and $\sigma_t = 60$ ps for the tracking detector.

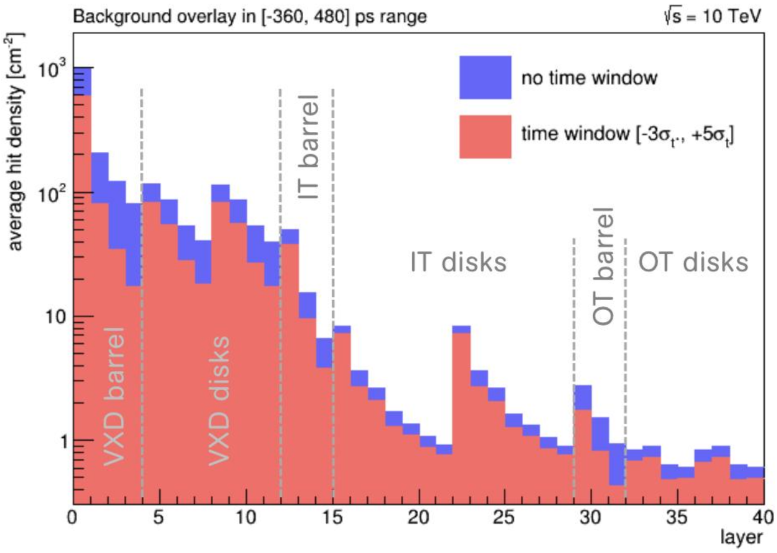

Figure 3.2: Average hit density for bunch crossing of BIB particles at $\sqrt{s} = 10$ TeV in the vertex and tracking detector. Results with the application of an acquisition time window are shown in red.[45]

A detailed description of the CKF algorithm can be found in [46, 47, 48]. The main steps are summarized as follows:

- **Seed generation:** The starting point in the CFK algorithm involves generating track seeds, which are the initial track candidates. This process begins with the DigiHit in the tracking system: seeds are formed by selecting triplets of DigiHits within the four layers

of the Vertex Detector, specifically considering only those hits located in the outer half of the doublet layers.
The seed generation process relies on the ACTS framework [49], a high-performance software toolkit developed for track reconstruction.

- **Track fitting** Once the seeds are identified, the CKF algorithm proceeds to the track fitting stage. In this step, the algorithm iteratively propagates each seed track through the subsequent layers of the tracker detector. As the track advances, the algorithm searches for additional hits in the layers that align with the predicted trajectory of the track. At each layer, the Kalman filter is employed to update the track parameters, refining the track's position, momentum, and direction by incorporating the new hits. This iterative fitting process continues until the track is fully reconstructed, with all relevant hits included. The result is a precisely fitted track that accurately represents the particle's trajectory through the entire detector system.

The performance of the CKF algorithm was evaluated using two samples of single muons generated from the interaction point with momentum fixed at $p = 10\,\text{GeV}$. The first sample consists of muons with uniform polar angle θ distribution between [10°, 170°], while the second sample includes muons with transverse momentum (p_T) respect the beam axis between [0, 10] GeV. Figures 3.3 illustrate the reconstruction efficiency as a function of the transverse moment, on the left side, and of the polar angle, on the right side. In this study, both scenarios were analyzed, with the contribution of the BIB, represented by the red line, and without it, indicated by the blue line. For muon with $p_T > 2GeV$ and in the central angular region, the reconstruction efficiency is about 100%, even in the presence of BIB. The visible drop in efficiency in the very forward/backward regions of the detector is mainly due to the increased presence of BIB particles in the proximity to the nozzles at very low and very high θ. This behavior is further confirmed by Figure 3.4, in which the distributions of the correctly reconstructed tracks associated with a generated muon are compared with those of the fake tracks (spurious tracks) as a function of the transverse momentum. From the figure, a strong increase in fake tracks in the low p_T regions can be observed.

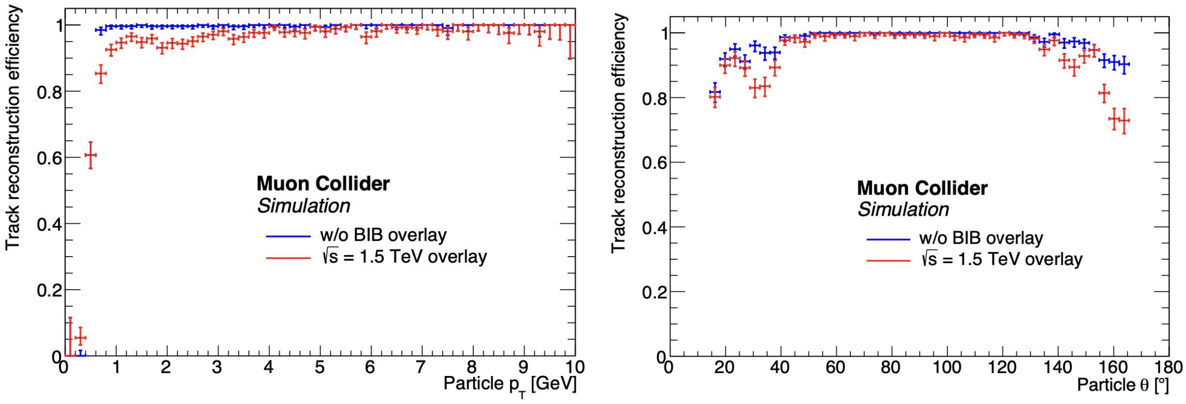

Figure 3.3: Track reconstruction efficiency as a function of the transversal momentum (figure left) and polar angle (figure right). The blu colour refers to the case considering the contribution of BIB, while in red the case without.[18]

3.2.2 Particle Flow Calorimetry and the PandoraPFA Algorithm

The Particle Flow calorimetry (PF) [50] was developed to address the need for high-granularity calorimeters, with the main goal of obtaining precise jets reconstruction. Jets are sets of particles generated by the hadronization process of quarks or gluons and represent one of the most complex objects to reconstruct accurately in a detector. The energy of a jet is carried mainly

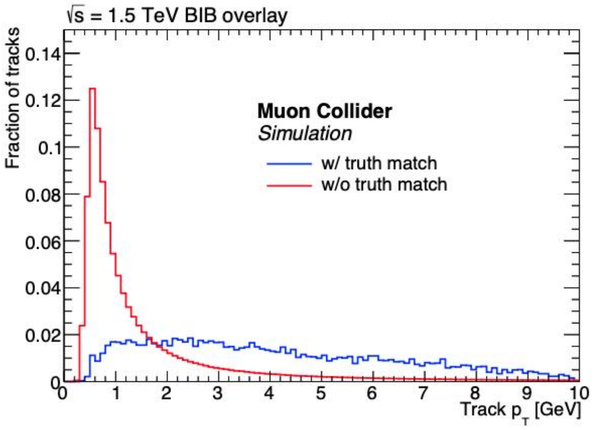

Figure 3.4: Distribution of the fraction of reconstructed tracks matched to a true simulated muon (in blue) and without matching (in red) as a function of transverse momentum.[18]

by charged particles, while a smaller part is given by photons, long-lived neutral hadrons and neutrinos.
To achieve high energy resolution in jets, the approach underlying the Particle Flow consists of precisely reconstructing the momentum and energy of each particle by combining the information provided by the various subdetectors.
In the standard calorimetric approach, the measurement of the energy of a jet is provided exclusively by the calorimetric system, which sums the energy deposits in both the ECAL and the HCAL. The main limitation of this methodology is due to the low energy resolution of hadronic calorimeters, with values typically around $\frac{\sigma_E}{E} \approx \frac{50\%}{\sqrt{E}}$.

Methods based on PF algorithms allow the enhancement of the jet energy resolution involving not only the calorimeters but also the information coming from the tracking system. Specifically from the tracker detector, it is possible to measure precisely the momentum of charged particles while the energy of the photons can be measured from the energy deposits in the ECAL. Consequently, the HCAL is mainly employed to measure only a small fraction of the jet energy associated with long-lived neutral hadrons and neutrons, thus reducing the effect of the poor resolution of the HCAL on the jet energy measurement. A representation of the Particle Flow method for the jet energy measurement can be seen in Figure 3.5 on the right side, while a comparison with the standard calorimetric method is shown on the left.

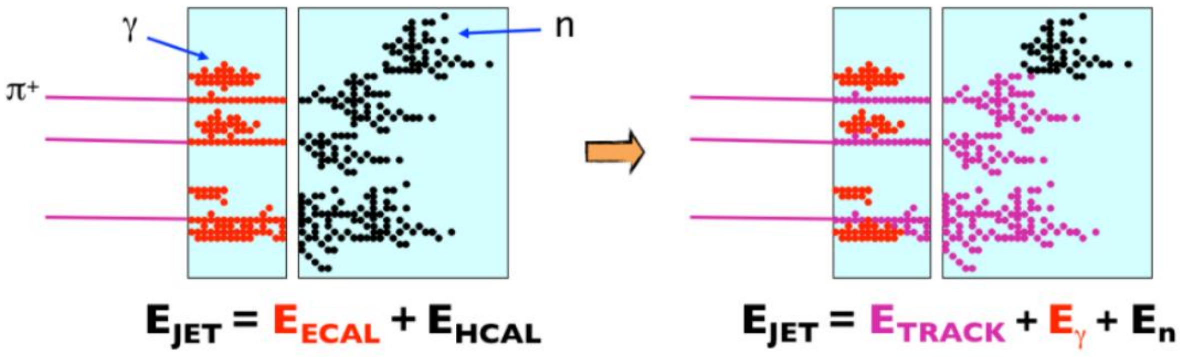

Figure 3.5: Illustration of standard calorimetric reconstruction method (left figure) and a Particle Flow algorithm (right figure).

PandoraPFA algorithm

A crucial aspect of achieving high performance with the Particle Flow approach is ensuring the correct association between energy deposits in the calorimeter and the corresponding particles. For instance, if the showers of a photon and a charged particle are close to each other and not well resolved, the photon's energy might be incorrectly attributed or even missed entirely. This task is managed by the Particle Flow Reconstruction Algorithm (PFA), which plays a pivotal role in correctly matching energy deposits to the corresponding particles. The accuracy of jet energy resolution is thus influenced not only by the intrinsic performance of the individual subdetectors but also by the effectiveness of the PFA software.
In the context of the International Linear Collider (ILC), the PandoraPFA algorithm was developed and implemented as part of the MARLIN reconstruction framework. This algorithm is also used in the Muon Collider environment, where the presence of Beam-Induced Background particles makes jet reconstruction particularly challenging.

PandoraPFA takes as input the track information of charged particles obtained from the tracking reconstruction, along with the DigiHits from the calorimeter system. The algorithm performs calorimeter clustering and Particle Flow reconstruction and the main steps are summarized in the following:

- Track selection: tracks are projected onto the front face of the electromagnetic calorimeter. The analysis identifies specific track patterns, such as kinks where a charged particle decays into another charged particle and neutral particles or cases where neutral particles decay into two charged particles.

- Selection of the Calorimeter hits: DigiHits in the calorimetric system contain information about the position (x,y,z) of the energy of the time and in the given layer of the calorimeter on which they are located. They are processed with the following procedure:

  - Hit selection: to identify relevant hits, a filter based on the energy of Minimum Ionizing Particles (MIPs) is applied. Specifically, only DigiHits exceeding a certain fraction of the energy expected from a MIP hit are retained, with specific thresholds of 0.5 for ECAL and 0.3 for HCAL.

  - Calibration: a correction is applied to the energy of the digits through specific calibration factors depending on whether the hit is associated with an electromagnetic or hadronic shower. This distinction is due to the difference between purely electromagnetic showers in ECAL generated by electrons and photons compared to hadronic showers. Hadronic showers are composed of two main components: an electromagnetic component, mainly generated by the decay of η and π mesons into photon pairs, and a purely hadronic component. The latter involves processes of interaction with matter, characterized by a portion of energy that is not directly measurable, called "invisible energy". This invisible energy is related to the binding energy of the nuclei released during the numerous nuclear interactions that occur in the shower.
    Due to the invisible energy effect, an asymmetry occurs in the calorimeter response when measuring the electromagnetic component and not in the hadronic showers. To correct this aspect, a specific compensation software is applied that allows the re-weight of the contribution of the energy given by the hits in HCAL.

  - Isolation requirements: During the initial phase of the clustering algorithm, groups of calorimetric hits that satisfy a minimum criterion of number of hits within a certain predefined distance are selected. Hits that do not meet these pre-clustering requirements are identified as isolated hits. These isolated hits are generally produced by the passage of particles that interact poorly with matter, such as low-energy neutrons generated during the development of hadronic showers. Since isolated hits are unlikely to be subsequently associated with particle showers, they are treated separately to avoid compromising the accuracy of the event reconstruction.

  - MIP identification: at the calorimetric system level, it is possible to identify tracks associated with minimally ionizing particles (MIPs) by analyzing the energy of the corresponding hits. In particular, the energy of the hits must not exceed predefined thresholds, calculated based on the expected energy that a MIP deposits when crossing the various layers of the calorimetric system. These thresholds helps in distinguishing MIPs from other particles that produce a higher energy deposition.
  - Hit Ordering: for each layer of the colorimetric system the hits are ordered according to their energy. With this order, they are given as input to the clustering algorithm.

- Clustering: hits in the calorimeter are grouped into clusters using a cone-based algorithm. This method leverages the fact that the hit direction is nearly aligned with the original particle's trajectory. As shown in the upper part of Figure 3.6, the process begins by using hits from the projected tracks on the electromagnetic calorimeter's front face as cluster seeds. The track direction at the ECAL face sets the initial cone direction. The algorithm proceeds layer by layer, adding hits within the cone or starting new clusters from unmatched hits.

- Topological Cluster Merging: the cluster fragments produced by the initial clustering algorithm, which are not associated with any trace, are processed through a series of algorithms based on topological models of the showers. In this way, neutral clusters are merged with charged clusters associated with traces, improving the reconstruction of showers. The algorithms use topological signatures to guide the merging of clusters, based on defined spatial and energetic criteria.

- Statistical re-clustering: if there's a mismatch between the energy measured in a cluster and the momentum of any tracks linked to it, the clustering process is repeated using adjusted parameters to better align the cluster energy with the expected track momentum.

- Photon identification: is based on the analysis of the longitudinal and transverse development of the showers inside the electromagnetic calorimeter. Specifically, the identification procedure can be done by comparing the shower profile as a function of the number of radiation lengths with the expected profile for an electromagnetic shower. An important aspect of this process is the ability to distinguish electromagnetic showers from hadronic showers. Through this methodology, it is also possible to identify and recover photons that may have been embedded in energy clusters associated with a hadronic shower, thus improving the accuracy of photon identification and reconstruction.

- Fragment removal: any remaining neutral clusters that haven't been identified as photons are added to the hadronic showers of charged particles, ensuring that all energy deposits are accounted for in the particle reconstruction.

- Formation of Particle Flow Objects: following these steps, reconstructed particles, called Particle Flow Objects (PFOs), are obtained. The energy of charged particles is derived from the momenta of their tracks, while the energy of neutral particles is determined directly from calorimeter measurements.

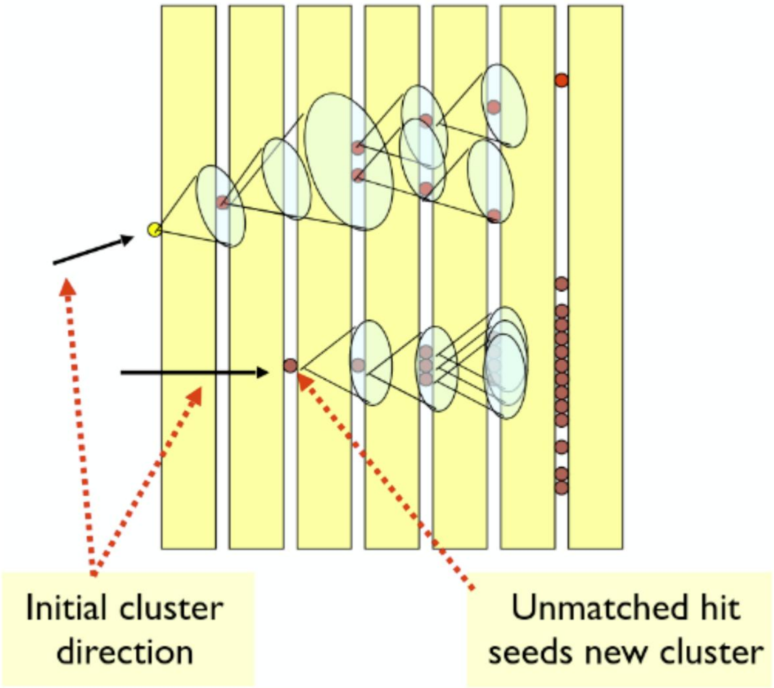

Figure 3.6: Schematic of the cone-based clustering algorithm. Two cases are distinguished: the presence of a seed on the internal face of the electromagnetic calorimeter (top) and the presence of unmarked hits (bottom).[51]

Chapter 4

An electromagnetic calorimeter for a Muon Collider Detector

This chapter presents the electromagnetic calorimeter requirements for a Muon Collider experiment and then introduces a highly promising and novel electromagnetic calorimeter technology being developed specifically for the Muon Collider's needs.

4.1 Overview on electromagnetic calorimeter in collider experiment

Calorimeters [52] are essential devices in detectors used in high-energy physics experiments, with the fundamental task of measuring the energy of particles. The operating principle underlying each calorimeter is the absorption of the energy of particles through their interaction with the material constituting the calorimeter. Particles, depending on their nature, can interact electromagnetically or through strong interaction. The result of these interactions is the production of numerous particles that form electromagnetic or hadronic showers, respectively, depending on the type of interaction. By measuring the energy deposited by these particles in the active components of the calorimeters, it is possible to obtain signals proportional to the energy of the initial particle.
Another important aspect regarding calorimeters is that they play a crucial role in particle identification (PID) since the analysis of the evolution of the showers inside the detector is possible and provides the possibility to detect neutral particles such as photons and neutrons, which leave no trace in other types of detectors, contributing significantly to the complete reconstruction of events in high-energy physics.

Electromagnetic calorimeters (ECAL) are a class of calorimeters specifically developed to measure photons, electrons, and positrons. They can be classified into two main categories based on their construction technique: homogeneous calorimeters and sampling calorimeters. Homogeneous calorimeters are characterized by being formed entirely of an active material, which absorbs the energy of the particles and at the same time generates a signal directly proportional to the deposited energy. The chosen material must be dense enough to be able to absorb even high-energy particles. While sampling calorimeters are made up of an alternating structure of passive materials (which absorb the energy of the particles and generate electromagnetic showers) and active materials (which collect the energy deposited by the shower products).

The energy resolution is one of the crucial parameters characterizing the performance of a calorimeter and allows to quantify the precision with which the calorimeter can determine the energy of the particles. The energy resolution of an electromagnetic calorimeter is usually described by the relation:

$$\frac{\sigma_E}{E} = \frac{a}{\sqrt{E}} \oplus \frac{b}{E} \oplus c \tag{4.1}$$

Where the following terms are:

- Stochastic term ($\frac{a}{\sqrt{E}}$): This term is related to the statistical fluctuations in the number of particles generated inside the calorimeter cell, which give rise to an electrical signal proportional to the deposited energy. It expresses the uncertainty due to the probabilistic nature of the particle interaction process in the calorimeter.

- Noise term ($\frac{b}{E}$): This term quantifies the contribution to the energy resolution arising from the noise in the readout chain. It depends on the type of detector used to measure the energy deposited in the calorimetric cell, as well as the specific characteristics of the readout circuit. In calorimeters where energy measurement is based on the detection of light produced by particle interactions with the material, the noise term is typically small. This is due to the high signal-to-noise ratio, resulting from the significant gain of the signal relative to the noise.

- Constant term (c): This term does not depend on the energy of the particle and is mainly related to effects due to non-uniformity of the calorimeter material. A typical cause of non-uniformity is for example aging following radiation damage.

4.2 Electromagnetic calorimeter requirements for a detector at Muon Collider

The presence of BIB within the detector significantly impacts also the calorimetric system, in addition to the tracking system discussed in section 3.2.1. Specifically, simulation studies at a center-of-mass energy of 1.5 TeV indicate that the flux of the BIB particles at the inner surface of the electromagnetic calorimeter barrel reaches approximately 300 particles per cm^2 [18]. Figure 4.1 provides a qualitative representation of the significant presence of BIB particles within the calorimetric system, highlighting the high particle density. This is further emphasized by the fact that in the figure, only a fraction of the particles from a single bunch crossing is considered. In the electromagnetic calorimeter, the BIB is predominantly composed of photons, about 96%, with an average energy of 1.7 MeV, while the remaining 4% consists of neutrons [18]. Additionally, an important characteristic, already mentioned in Section 1.4, relates to the arrival time of the BIB particles, which exhibits a broad distribution relative to the bunch crossing. As presented in the following, this characteristic is crucial for the mitigation process of the BIB in the ECAL.

Figure 4.2 shows the occupancy levels in the barrel (figure left) and endcap (figure right) of the calorimetric system: ECAL (red line) and HCAL (blue line). In the Barrel is possible to notice that the occupancy level has a decreasing trend as the depth of the calorimeter increases; this effect is due to the progressive absorption of particles by the calorimeter material. Similarly in the endcap region, the occupancy level decreases as a function of the z-coordinate. The histograms indicate that the majority of BIB particles are absorbed by the first layers of the electromagnetic calorimeter, with only a small fraction reaching the hadronic calorimeter where therefore the impact of the BIB is considerably lower.

Another important consideration, closely related to the high flux of BIB particles, is the amount of radiation dose received by the calorimeter system. An elevated radiation dose can impact the performance and longevity of the materials, necessitating robust design and material choices to

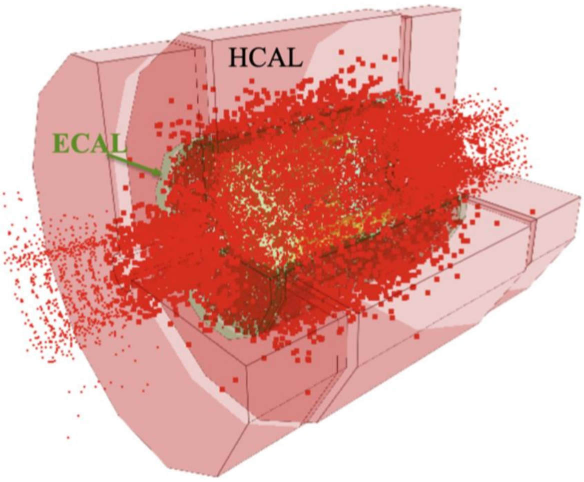

Figure 4.1: Illustration of the presence of BIB particles in the calorimeter systems: ECAL and HCAL. The figure has been obtained with BIB generated at a center-of-mass energy of 1.5 TeV and considering only a fraction of the entire amount of BIB particles in a bunch crossing.[53]

ensure accurate measurements and detector durability. Simulation studies at $\sqrt{s} = 1.5$ TeV, predict that the ECAL will be subjected to a total ionizing dose of 100 krad/y and a $10^{13-14} cm^{-2}$ 1-MeV-neq fluence.

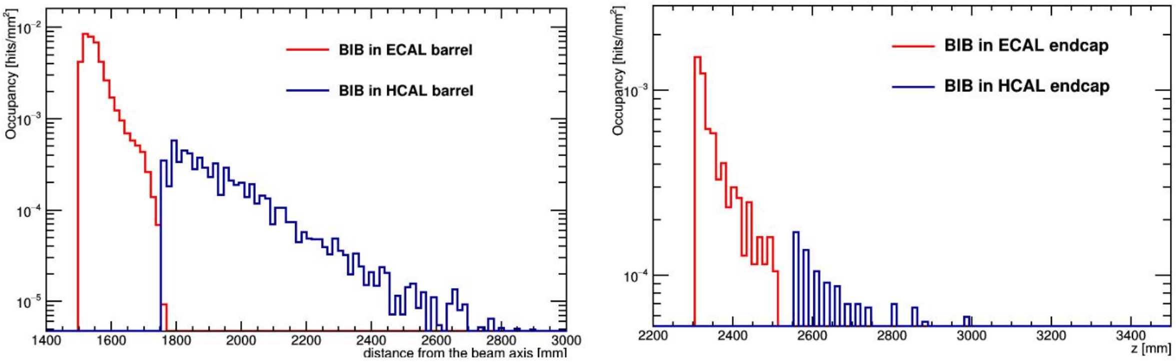

Figure 4.2: Occupancy at hit level in the calorimeter system as a function of the distance from the beam axis. The red line represents the ECAL, and the blue line represents the HCAL. The Figure on the left shows the Barrel region, while on the right there is the Endcap region. [18]

In this experimental environment, the calorimetric system for the Muon Collider detector must meet the following requirements to provide the necessary BIB mitigation and ensure optimal measurement performance:

- **High granularity** to reduce the overlap of BIB particle hits in the same calorimeter cell. During the signal integration time within a cell, this overlap can produce hits with an energy deposit similar to the one of a primary interaction particle, making it harder to separate the two contributions. Additionally, high granularity allows for more accurate measurement of energy deposits from the particles of interest.
- **Good arrival particle time resolution** to reduce the out-of-time component of the BIB. Figure 4.3 (left) compares the arrival time distribution of hits generated by BIB particles (in red) to those produced by particles from $\mu + \mu^- \rightarrow H\nu\bar{\nu} \rightarrow b\bar{b}$ decay process (in blue). It can be observed that by introducing an acquisition time window of about $\Delta t \approx 300$ps from the bunch crossing time, a significant portion of the BIB hits can be effectively filtered out while preserving most of the hits from the events of interest. To

apply such an acquisition window it is necessary to achieve a temporal resolution at ECAL in the order of 100 ps ($\Delta t \approx 3\sigma_t$).

- **Longitudinal segmentation** to discriminate between the different energy profiles produced by particles coming from a muon collision and those coming from BIB. Figure4.3 on the right shows a comparison of the energy distribution as a function of the distance from the beam axis between hits produced by particles originating from interaction events $\mu + \mu^- \to H\nu\bar{\nu} \to b\bar{b}$ (in blue) and those from BIB (in red). Most of the energy from BIB particles is deposited in the first layers of the ECAL, while particles from a primary interaction present a deeper longitudinal energy distribution. An appropriate segmentation of the calorimeter is fundamental for distinguishing between electromagnetic showers originating from particles produced in muon collision events and those arising from BIB contributions.

- **Good energy resolution** in the electromagnetic calorimeter represents an essential feature for critical physics measurements. Specifically, allows to precisely reconstruct the energy of electrons and photons, which are fundamental to study processes such as Higgs boson decay into photon pairs ($H \to \gamma\gamma$) or Z boson decay into electron-positron pairs ($Z \to e^+e^-$). These measurements require high energy resolution to accurately determine the invariant mass of these systems. Achieving an energy resolution below $10\%\sqrt{E}$ is necessary to minimize uncertainties in mass reconstruction, enabling the detector to resolve small mass differences and significantly enhance the overall discovery potential of the Muon Collider.

- **Radiation hardness** of the components forming the calorimeter system. As discussed in 2.6, the radiation levels expected in the calorimetric system of the Muon Collider are lower than those expected for the HL-LHC. This guarantees that the performance of the calorimeter will not be compromised by critical issues related to the accumulation of high doses of radiation. As a result, materials can be selected from those commonly used in high-energy collider experiments.

- **Optimal containment of electromagnetic showers:** A crucial aspect to evaluate during the design of a calorimeter is its capability to contain the energy of electromagnetic showers. This property is crucial for an electromagnetic calorimeter and directly impacts its performance in measuring the energy of particles that pass through it. In the high-energy experimental environment of the Muon Collider, it is very important to have an electromagnetic calorimeter with a sufficient number of radiation lengths (X_0), to properly contain the energy of high-energy particles like photons or electrons with TeV-scale energies.

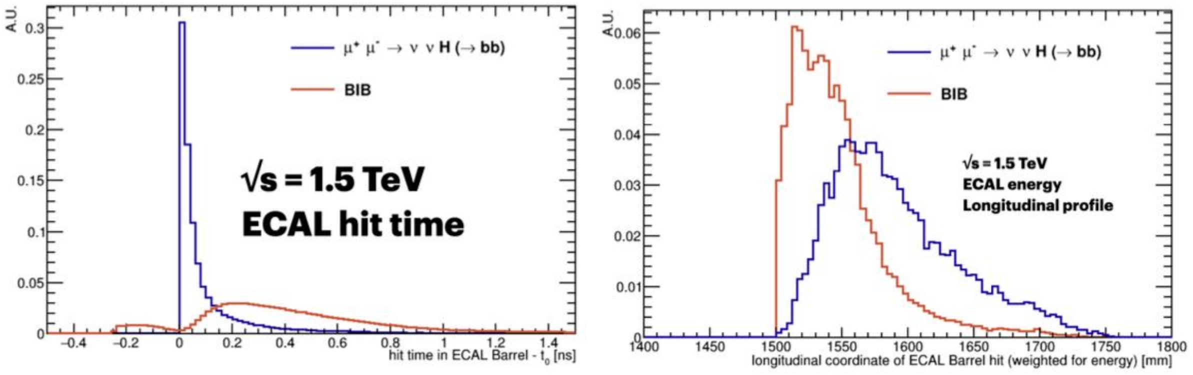

Figure 4.3: Left: Distribution of the arrival time of hits in the ECAL barrel relative to the bunch-crossing time. The blue line corresponds to particles coming from a primary interaction, while the red line shows the contribution from BIB particles. Right: Energy distribution of hits in the ECAL barrel as a function of distance from the beam axis. Color legend is the same of left plot. [54]

4.3 The CRILIN calorimeter

CRILIN (CRystal calorImeter with Longitudinal INformation) [55], can meet the above requirements. It consists of a semi-homogeneous calorimeter based on Lead Fluoride (PbF_2) crystals read out by surface mounted ultraviolet extended Silicon Photomultipliers (SiPMs). Figure 4.4 provides a representation in the Muon Collider detector, of the geometric configuration and spatial arrangement of the barrel,in green, of the CRILIN calorimeter, illustrating its dodecahedral structure surrounding the interaction point along with the two nozzles.

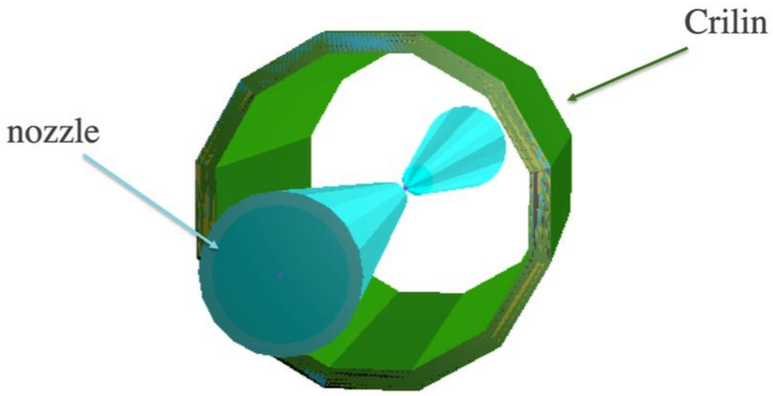

Figure 4.4: Rendering of the CRILIN electromagnetic calorimeter barrel showing its dodecahedral structure in the x-y transverse plane relative to the z-axis of the beam. In blue, the pair of nozzle absorbers are depicted.[56]

A semi-homogeneous calorimeter represents a modern design approach that aims to combine the intrinsic high-energy resolution of homogeneous calorimeters with the longitudinal segmentation typically found in sampling calorimeters. This combination enhances both performance and flexibility. In Figure 4.5, the semi-homogeneous structure is shown. The left figure illustrates the arrangement of the crystals forming the various layers, with the black lines indicating the separation between consecutive layers. The right figure highlights the positions of the photodetectors within the calorimeter structure; these detectors are placed between crystal layers and are related to each individual calorimeter cell.

By employing a structure composed of crystal matrices, a modular design is achieved, consisting of interchangeable blocks of crystal matrices. This feature is highly advantageous for the calorimeter design, as it allows for optimization of the geometry (such as the number of layers) to achieve the best measurement performance. Consequently, the longitudinal information from the shower development can be utilized effectively to optimize BIB effects mitigation. This adaptability ensures that the calorimeter can be fine-tuned to meet specific experimental requirements, thus maximizing the efficiency and precision of particle detection.

Figure 4.6 (left) provides a graphical representation of a single cell of the CRILIN calorimeter. Each one comprises a single crystal optically connected to a photosensor made up of 4 SiPM sensors. These SiPMs are paired to form two readout channels for each cell, with the flexibility to be connected either in series or in parallel. This aspect will be discussed in more detail in Chapter 6.

Figure 4.6 on the right shows in red the development of the Cherenkov radiation component within the cell, obtained via GEANT4 simulation of a 120 GeV electron passing through the crystal longitudinal axis. To efficiently contain the Cherenkov light produced within the cell, the crystals are equipped with an external wrapping of material with a high reflectivity index. The materials considered for the CRILIN cells are primarily Teflon and Mylar [57]. The performance and radiation resistance characteristics of the CRILIN proposal will be discussed in Chapter 6.

The layout considered for the electromagnetic calorimeter design using the CRILIN proposal consists of six layers of crystals in the shape of parallelepipeds with a square base. To achieve adequate granularity, the transverse size of the crystals was set at 10x10 mm^2. With a length of 40 mm, this configuration allows for a total of 26 radiation lengths (X_0), ensuring sufficient containment of electromagnetic showers even for objects with energies in the TeV range.
Regarding the photodetectors, SiPMs were chosen for their excellent radiation resistance and their ability to operate within magnetic fields, which is crucial given the ECAL's placement inside the solenoid. The selected SiPM sensors, with dimensions of 30x30 mm^2, were chosen to maximize light collection efficiency within each individual cell, ensuring optimal coverage of the crystal's base surface. This size also reflects a careful consideration of energy consumption, aiming to minimize heat generation by the detectors while maintaining high performance. As detailed in Chapter 6, the SiPM pixel size was set to 10 μm. This specific choice helps to significantly reduce dark noise, which is essential for achieving a high signal-to-noise ratio. Additionally, the smaller pixel size enhances resolution and accuracy in detecting the Cherenkov light produced within the CRILIN crystals, contributing to overall detector performance.

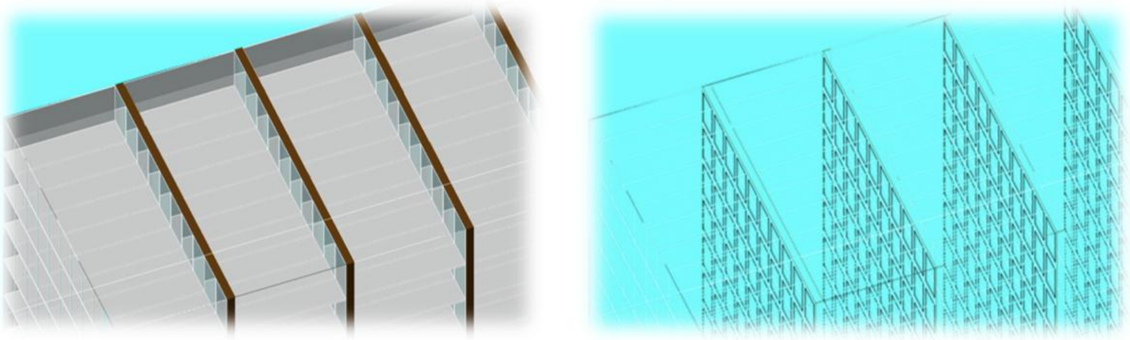

Figure 4.5: Graphical representation of the design of a semi-homogeneous calorimeter, like CRILIN. Left: arrangement of various layers of crystal matrices. Right: illustration of the position of SiPMs within the semi-homogeneous structure.[58]

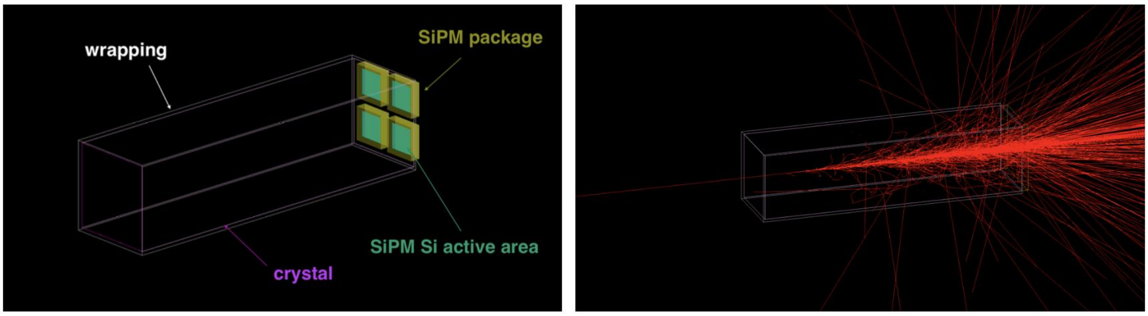

Figure 4.6: Left: schematic view of a single CRILIN cell. Right: graphical representation of Cerenkov light within a single cell, obtained from the simulation of a 120 GeV electron passage thought the crystal.[58]

4.4 CRILIN in the Muon Collider detector

The CRILIN ECAL offers a promising option for a Muon Collider detector, optimally meeting the requirements for the electromagnetic calorimeter as presented previously, in particular:

- Thanks to its semi-homogeneous configuration composed of layers of crystals, CRILIN ECAL enables the extraction of longitudinal information about the development of electromagnetic showers. This aspect is extremely useful to distinguish showers caused by BIB particles from those originating from primary muon interaction particles. By analyzing the shower development across various calorimeter layers, it becomes possible to identify and mitigate the effects of BIB particles through the implementation of dedicated algorithms.

- The use of crystals with a base size of 10 x 10 mm^2 allows the creation of cells with fine granularity. This feature helps to reduce the density of hits within a single cell that are summed during the acquisition window, thereby improving the ability to distinguish, based on the measured energy, between the two contributions. Additionally, the high granularity offers significant advantages for the Particle Flow calorimetry approach, as discussed in Section 3.2, enhancing the accuracy of particle reconstruction.
- The use of Cherenkov crystals PbF_2 enables the production of a very fast signal. As soon as particles enter the cell, they immediately start generating Cherenkov light. This feature, combined with the cell's longitudinal dimension, allows for high temporal resolution. This capability allows for the implementation of precise time windows to effectively filter out the out-of-time component of the BIB as presented in 1.4.
- PbF_2 crystals and SiPMs are components that offer excellent radiation resistance. They have been used in other collier experiments, and their resistance to radiation is well-documented [59] and [60]. This aspect, together with the radiation levels expected at the calorimeter of the Muon Collider which are lower than those of the HL-LHC, guarantee stable operation during the data acquisition runs.

The combination of all these aspects mark the fact that the CRILIN proposal for the electromagnetic calorimeter could be a very promising option for a Muon Collider detector experiment.

Chapter 5

Characterization of CRILIN performance in Muon Collider detector

This chapter is dedicated to the discussion of the performance characterization of the CRILIN EMCal through a simulation study. The CRILIN EMCal was implemented within the detector geometry using the configuration presented in Chapter 4. The response of the electromagnetic calorimeter equipped with 6 layers of CRILIN is evaluated in terms of energy resolution, reconstruction efficiency, and electromagnetic shower containment.

The first part of the chapter describes the various particle samples used during this study. Following this, the characterization of BIB particles in the calorimetric system will be presented, and a background mitigation procedure will be defined, taking advantage of the characteristics of CRILIN. The chapter will describe the analysis procedure for the estimation of the energy resolution comparing the results obtained from a sample of photons also considering the presence of the BIB. Finally, the last part of the chapter is dedicated to a study on the energy containment of the electromagnetic showers in the CRILIN calorimeters.

5.1 Photon Sample Datasets for Calorimeter Studies

The performance of the CRILIN ECAL within the muon collider detector configuration has been evaluated through detailed simulations of the detector by using a specific photon sample. The choice to use photons as reference particles for the analysis of the calorimeter performance is motivated by the fact that photons, unlike electrons, do not interact with the detector tracking system. This allows the isolation and study in a more direct and effective way of the behavior of the calorimetric system, without introducing the additional complexities related to the reconstruction of the track and the identification of the electrons from other charged particles.

Two categories of single-photon events samples (referred to as photon-gun in this thesis) are generated at the interaction point: one features a continuous energy spectrum and the other with a discrete energy spectrum. These samples are produced at the Monte Carlo level as explained in 3.1.1 and then processed through the simulation and reconstruction pipeline, as described in Chapter 3.

5.1.1 Continuous energy spectrum samples

The photon samples with continuous energy spectrum are used for the performance evaluation of the CRILIN ECAL. In particular, two distinct sets of samples are produced in the barrel region of the detector.

- A first sample of 15000 photons with energies uniformly distributed between 1 GeV and 1000 GeV. This sample was used for the CRILIN performance studies for the 1.5 TeV detector geometry presented in section 5.2.
- A second sample of 20000 photons, divided into 10000 photons with energies uniformly distributed between 1 GeV and 250 GeV and another 10000 photons with energies uniformly distributed between 250 GeV and 1000 GeV. This sample of photons was used for the performance studies of CRILIN with the detector configuration for a center-of-mass energy of 10 TeV (the MUSIC concept described in 2).

In Figure 5.1, the energy at generation level, called in this thesis E_{True}, distributions of both samples are shown. The left figure shows the 15000 photon sample with a uniform energy range between 1 GeV and 1000 GeV. While the right figure shows the second sample with the low-energy part depicted in red and the high-energy component in blue.
Both samples are uniformly generated within a polar angle range, θ, between 70° and 110°. This angular range defines a region around the center of the detector barrel at 90°, which is perpendicular to the beam axis. The choice of this angular range is motivated by the need to avoid transition regions between the barrel and endcap, where the detector is less instrumented. Finally, the sample was uniformly generated across the entire azimuthal angle, ϕ. Figure 5.2 shows the angular distributions for the two samples together, highlighting their uniformity between 70° and 110°.

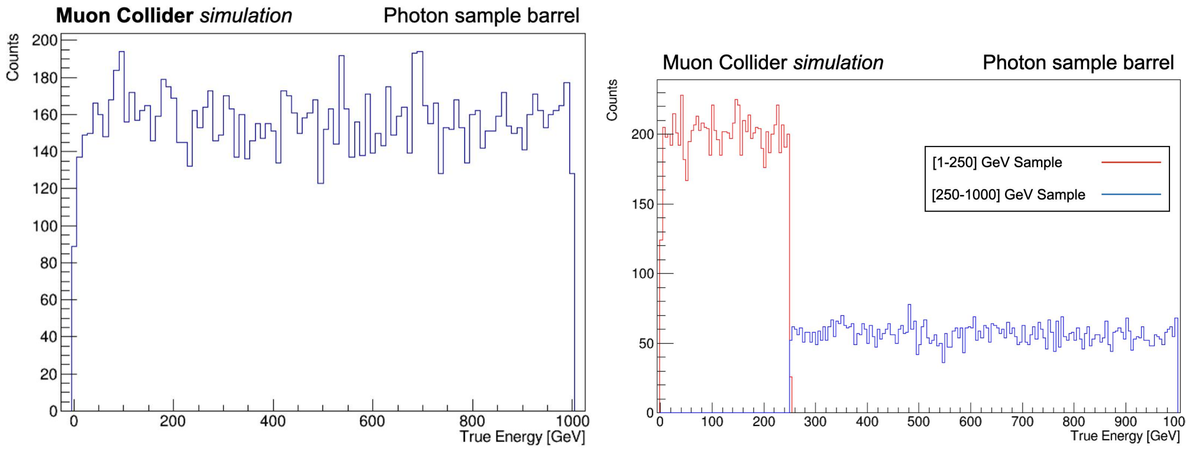

Figure 5.1: True level energy distribution of the photon samples generated in the barrel region of the detector. Left: sample of 15000 photons with uniform energy distribution between [1, 1000] GeV. Right: sample of 20000 photons, of which 10000 with energy between [1.250] GeV (in red) and the remaining 10000 with energy between [250,1000] GeV (in blue).

5.1.2 Discrete energy spectrum samples

In order to compare the characteristics of the BIB particles in the electromagnetic calorimeter with respect to the signal generated by the photons, a series of monochromatic photon samples was generated using the Monte Carlo generation method with the particle gun described in 3.1.1. These samples are produced both in the barrel and endcap regions. Each sample consisted of 1000 single-photon events with fixed energies of 1 GeV, 10 GeV, 100 GeV, and 500 GeV. The photon samples were generated with a uniform distribution in polar angle within the following angular regions:

- Barrel region: uniformly distributed within the total angular region of the barrel $\theta \in [35°, 145°]$.
- Endcap region: uniformly distributed within $\theta \in [10°, 35°] \cup [145°, 170°]$, corresponding the complete polar angular interval of the endcap.

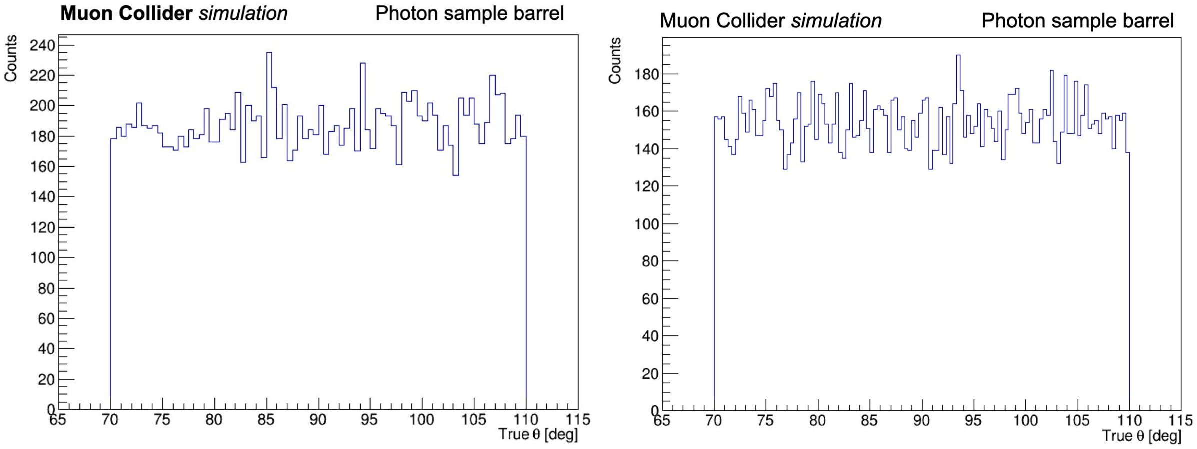

Figure 5.2: Distribution of the polar angle θ at the true level of the generation, uniformly distributed between 70° and 110°. The histogram shows the contributions from both samples: on the left, the sample of 15000 photons, and on the right, the sample of 20000 photons.

5.2 The CRILIN characterization for $\sqrt{s} = 1.5$ TeV Muon Collider detector

The first approach to the characterization study of the CRILIN electromagnetic calorimeter in the Muon Collider experiment was carried out starting from the detector configuration for the $\sqrt{s} = 1.5$ TeV phase [18]. The main differences compared to the configuration proposed for a center of mass energy of 10 TeV, presented in Chapter 2, are the following:

- in the 1.5 TeV configuration, the solenoid is positioned outside the HCAL, while in the $\sqrt{s} = 10$ TeV configuration it has been placed between the ECAL and the HCAL.
- the CRILIN system is composed of 5 layers of crystals, while in the MuSIC configuration, 6 layers are considered.

Considering this detector configuration, the performances of CRILIN in terms of energy resolution, reconstruction efficiency, and energy containment level of the electromagnetic showers were estimated considering the 15000 photon sample in the barrel region of the detector with energy between [1, 1000]GeV as defined in 5.1. This study was carried out also considering the effect of the presence of the BIB by using a BIB sample at a center-of-mass energy of 1.5 TeV, which as seen in 1.4 presents characteristics very similar to the case $\sqrt{s} = 3$ TeV.

5.2.1 Reconstruction procedure with the BIB overlay

The reconstruction process for the performance study in the presence of the BIB was performed by applying a DigiHit selection procedure in the electromagnetic calorimeter, with the aim of reducing the computational time during the clustering phase in the reconstruction of single photon events. In the case of the performance study without the BIB, this procedure was not applied, since the aim was to obtain an estimate of the pure CRILIN performance.
The selection criterion adopted is based on the fact that, as illustrated in chapter 1.4, BIB particles are characterized by low energy and release hits with lower energy than those produced by the passage of signal particles from muon collisions. Therefore, the selection procedure involves the application of thresholds on the energy of the DigiHits in the CRILIN calorimeter, with values that vary as a function of the layer and of the spatial region of the barrel along the longitudinal coordinate z (corresponding to the beam axis). In particular, the barrel has been divided into 3 regions: a central region defined by the interval $z \in [-736.6, 736.6]$ mm and a intermediate region defined by the intervals $z \in [-1473.6, -736.6] \cup [736.6, 1473.6]$mm and a forward region defined by the intervals $z \in [-2210, -1473.6] \cup [1473.6, 2210]$mm . For

each layer and region, the BIB energy distribution was examined and the energy threshold value was extrapolated from the mean energy summed with two times the Root-Mean-Square of the corresponding distribution. This represents a lower limit for the DigiHit energy in order to filter out the contribution form the BIB. The values are presented in the following Table5.1:

Layer	Central region [MeV]	intermediate region [MeV]	Forward region [MeV]
1	285.3	232.7	138.4
2	165.1	137.5	83.6
3	68.5	58.6	38.8
4	44.2	39.5	29.4
5	36.4	33.7	25.3

Table 5.1: Energy threshold values as a function of the CRILIN layer for the forward and the central, intermediate and forward regions of the barrel.

5.2.2 Matching procedure

In order to evaluate the performance of the CRILIN calorimeter, it was necessary to match the reconstructed photon with the corresponding particles generated at the Monte Carlo level.

The matching procedure adopted for this study is based on the following criteria applied to the reconstructed particles:

- I selected, among the set of particles reconstructed in the detector in a single event, all those identified as photons.
- As illustrated in Figure 5.3 left, among the particles reconstructed as photons, I subsequently selected only those contained within a cone defined around the direction of propagation of the generated photon. The cone is characterized by an opening radius $\Delta R = \sqrt{\Delta\phi^2 + \Delta\eta^2} = 0.1$, where $\Delta\phi$ represents the difference in azimuthal angle between the direction of propagation of the generated photon and the reconstructed one, while $\Delta\eta$ indicates the corresponding difference in pseudorapidity ($\eta = -\ln[\tan\frac{\theta}{2}]$). The chosen value for the cone opening radius was determined by observing the distribution of ΔR among all particles reconstructed as photons in all the photon sample. As highlighted in Figure 5.3 right, a radius of 0.1 allows the inclusion of the reconstructed photon corresponding to the generated one. At the same time, it was important not to choose an excessively large value to avoid the higher contamination by BIB.
- Following this selection step, if multiple particles reconstructed as photons were observed inside the cone, the one with the energy closest to that of the generated photon was chosen. Conversely, if no reconstructed photon was observed, the event was discarded and labeled as unreconstructed.
- Finally, the event was considered reconstructed if the photon inside the cone had an energy at least half that of the generated photon.

By applying the described matching procedure, it was possible to associate the particles reconstructed as photons to those corresponding at the generation level. This selection criterion was adopted both in the study conducted in the absence of BIB and in the subsequent one, with the BIB overlay on the photon sample.
In Figure 5.4, the reconstruction efficiency of the detector using the described selection procedure is shown. The left figure presents the efficiency as a function of the photon energy at the generation level, while the right figure shows the efficiency as a function of the polar angle between 70° and 110°, the range in which the photon sample was defined.
The results obtained show an excellent reconstruction efficiency, with values above 95% over the entire energy spectrum and angular range analyzed. This is true both in the case without

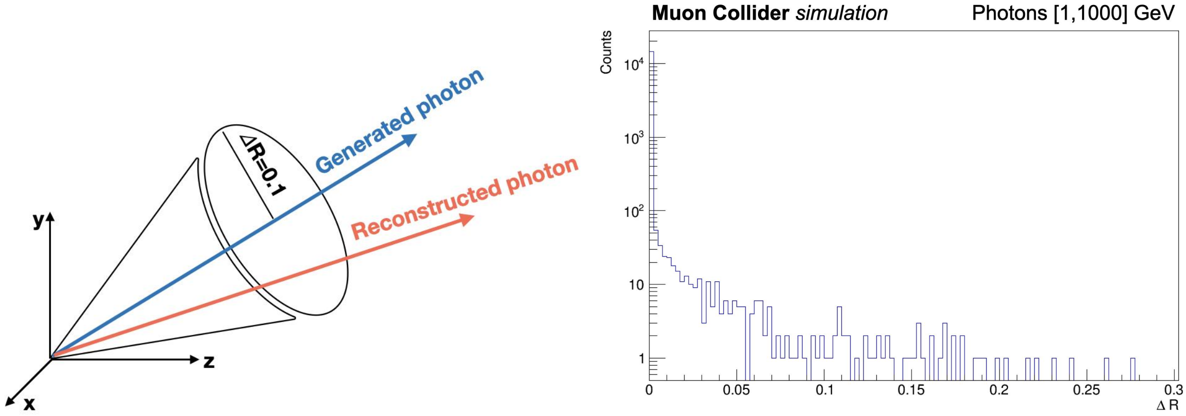

Figure 5.3: Left: Graphical representation of the cone defined around the direction of the generated photon, with opening radius $\Delta R = 0.1$. The selection includes only particles reconstructed as photons and contained within the cone. Right: Distribution of ΔR values among the generated photons and all particles reconstructed as photons. The histogram refers to the entire sample of 15000 events containing photons.

the contribution of the BIB (blue line) and in the case in which the overlay with the BIB at $\sqrt{s} = 1.5$ TeV was considered.

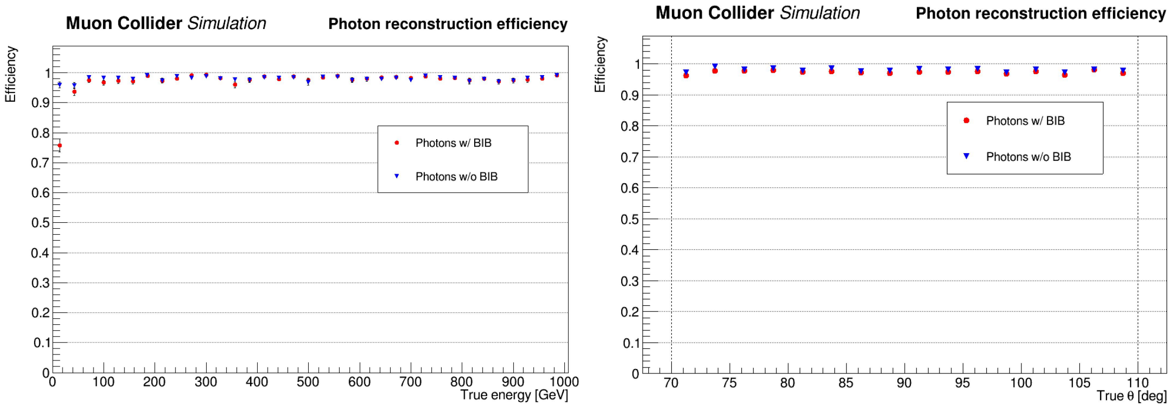

Figure 5.4: Left: reconstruction efficiency as a function of the energy of the generated photon sample. Right: reconstruction efficiency as a function of the polar angle between 70° and 110° in which the sample was defined. In both graphs the case in which the BIB contribution was absent (blue) was compared with the case in which the BIB at $\sqrt{s} = 1.5$ TeV was considered (red)

5.2.3 Energy resolution study

Before starting the study of the energy resolution of the CRILIN calorimeter, it was necessary to apply a correction to the energy of the photons reconstructed by the detector, selected with the procedure described above. This correction was essential to make the uniform in the entire energy range considered the response of the detector. The energy of the reconstructed photons, denoted as E_{reco}, was corrected by multiplying it by a correction factor K_{corr}, defined as the ratio between the generation-level photon energy, called E_{True}, and the reconstructed photon energy:

$$K_{corr} = \frac{E_{True}}{E_{reco}} \tag{5.1}$$

In Figure 5.5 on the left, the values of the correction parameter as a function of the reconstructed photon energy for each single event of the photon sample are reported. As can be observed, the values of K_{corr} are primarily concentrated below 1.2, maintaining an almost constant trend around 1.065 for energies above 25 GeV, while showing a more pronounced increase for energies below 25 GeV. In Figure 5.5 on the right, the corresponding distribution of the correction parameter values for the photon sample is reported, also considering the contribution of the BIB. In this case, it is observed that the energy deposits due to the BIB particles lead to a general increase in the correction parameter values, which are distributed around $K_{corr} \approx 1.55$.

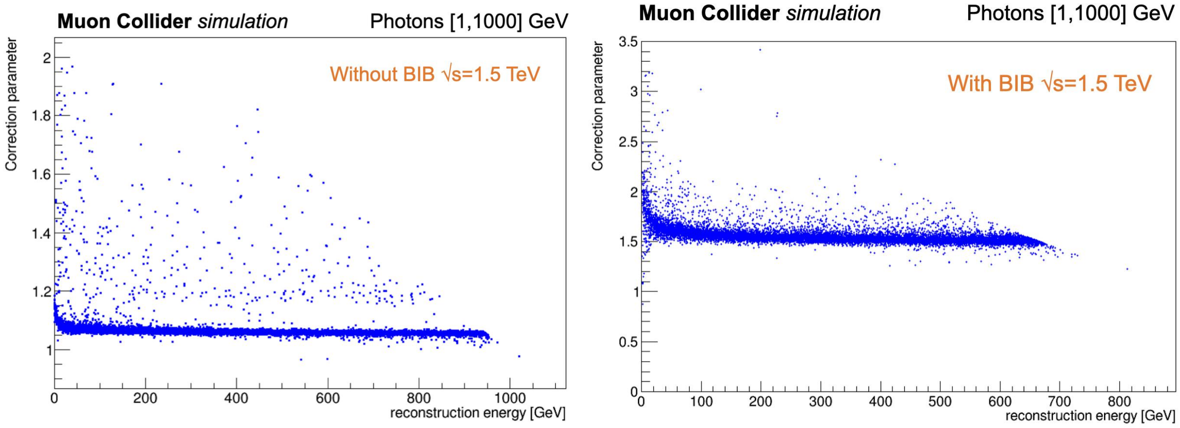

Figure 5.5: Distribution of the correction parameter values as a function of the reconstructed photon energy for each single event of the photon sample. On the left, is the case without BIB overlay while on the right, is the case with photons and the BIB contribution at $\sqrt{s} = 1.5$ TeV.

To parameterize the behavior of the correction factor as a function of the reconstructed energy, the energy range was divided into sub-intervals of equal width. For each interval, the mean value of the correction factor was calculated. The overall trend of the mean correction factor as a function of reconstructed energy is shown in Figure 5.6: on the left, case without BIB contribution, and on the right with the presence of the BIB. In both cases, the mean values of the correction parameter were fitted with a polynomial function of degrees 9 and 6, respectively. It is emphasized that no correction of the energy as a function of the polar angle has been applied, but only as a function of the energy. This choice is motivated by the narrow angular region considered for the photon sample.

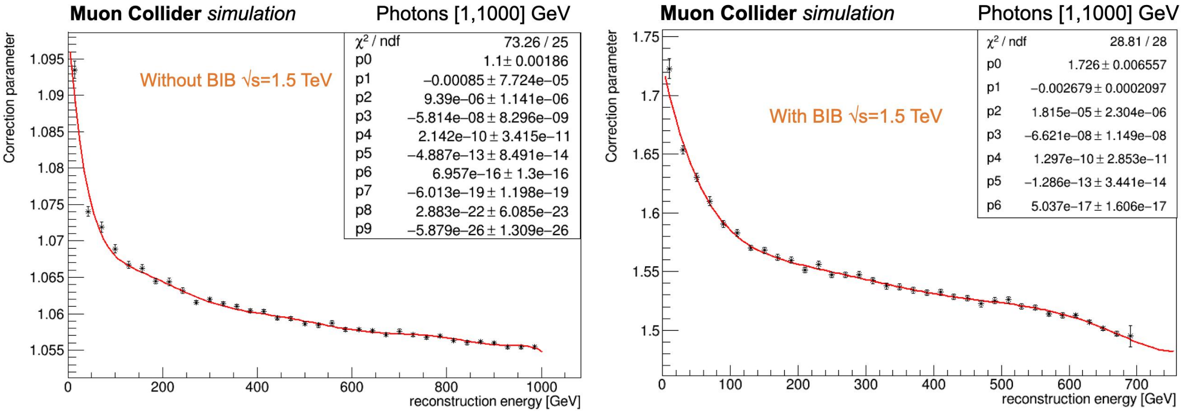

Figure 5.6: Trend of the mean values of the correction parameter as a function of the energy of the reconstructed photons. The fit was obtained with a polynomial function of degree 9 and 6 respectively for the case without BIB contribution (left figure) and with BIB (right figure).

Once the energy calibration of the calorimeter was obtained, the energy resolution characterization of the CRILIN calorimeter was performed by analyzing the relative difference ($\frac{\Delta E}{E}$) between the photon energy at the generator level and the energy of the reconstructed photon incorporating also the correction parameter K_{corr}. The relative difference $\frac{\Delta E}{E}$ is defined with the following relation:

$$\frac{\Delta_E}{E_{True}} = \frac{E_{True} - E_{reco} \cdot K_{corr}}{E_{True}} \tag{5.2}$$

In particular, the procedure I applied to determine the energy resolution, both with and without the contributions from the BIB, is described in the following points:

- first of all, I divided the [1, 1000] GeV range of E_{True} into 18 sub-intervals of equal width and, for each of them, I have considered the distribution of $\frac{\Delta_E}{E_{True}}$. In Figure 5.7 four representative examples of these distributions in the case of the photon sample without the BIB contribution are reported. In the top row, the left figure refers to the energy sub-interval between [166-222] GeV and the right figure to the sub-interval [500-555] GeV. In the row below, the histograms relating to the sub-intervals between [833,888] GeV and [916, 972] GeV are presented on the left and right sides respectively. As can be observed, the distributions of $\frac{\Delta_E}{E_{True}}$ show a peak around zero, this aspect confirms the effectiveness of the correction procedure applied to the reconstructed energy.
- As illustrated in Figures 5.7, I applied a Gaussian fit to each of these distributions. This approach allows the extraction of the sigma value from the fit, providing an estimate of the width of the $\frac{\Delta_E}{E_{True}}$ distributions for each energy sub-interval.

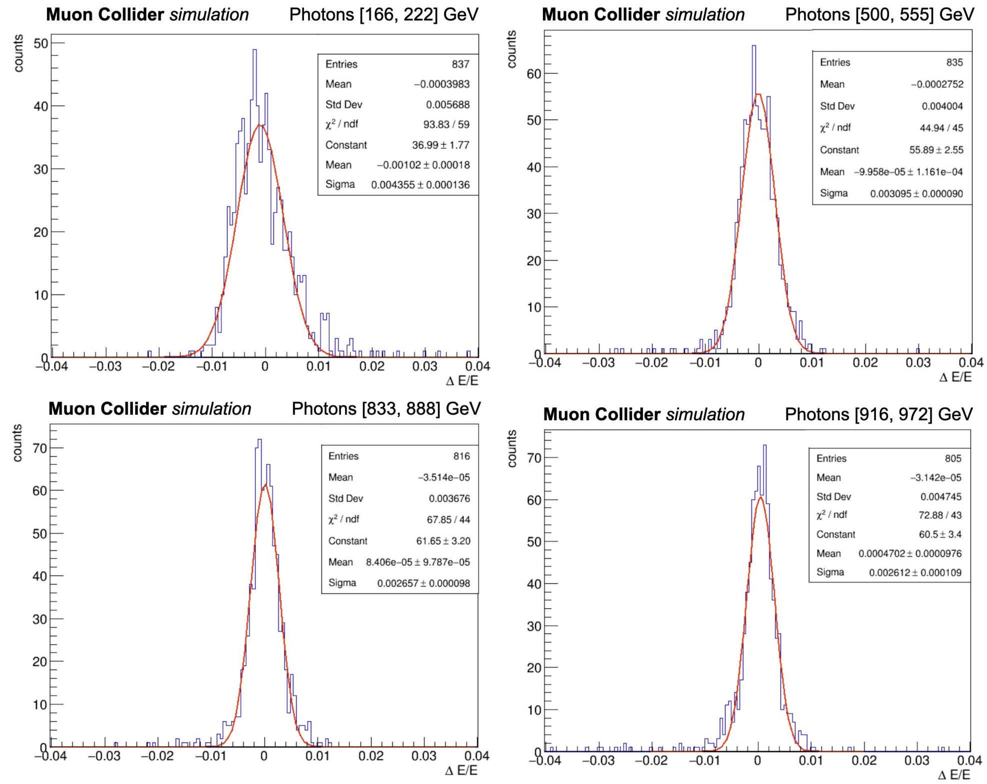

Figure 5.7: Distribution of the energy ratio $\frac{\Delta_E}{E}$ relative to different true level photon energy sub-intervals. Upper left $E \in [166, 222]$ GeV. Upper right $E \in [500, 555]$ GeV. Lower left $E \in [833, 888]$ GeV. Lower right $E \in [916, 972]$ GeV.

Figure 5.8 shows the trend of the σ values obtained for each energy interval, using the procedure described above. The results are compared between the case without the contribution of the BIB (in blue) and the case with the contribution of the BIB (in red). The trend of the energy resolution of the CRILIN calorimeter was determined by fitting the data with the typical parameterization used for homogeneous electromagnetic calorimeters.
The results obtained, both in the case without BIB 5.3 and in the case with BIB 5.4, are reported below:

$$\frac{\sigma_E}{E} = \frac{(4.8 \pm 0.1)\%}{\sqrt{E[GeV]}} \oplus (0.222 \pm 0.006)\% \tag{5.3}$$

$$\frac{\sigma_E}{E} = \frac{(15 \pm 1)\%}{\sqrt{E[GeV]}} \oplus (0.77 \pm 0.04)\% \tag{5.4}$$

Based on these results, the following observations can be made:

- Starting from the result obtained for the photon sample in the absence of the BIB contribution; this has been an important verification of the pure performances of the ECAL CRILIN in a wide energy range. The value of the estimate of the energy resolution obtained falls perfectly within the requirements for the electromagnetic calorimeter for the Muon Collider and this confirms the validity of this new proposal of electromagnetic calorimeter.
- Considering the result obtained with the photon sample and also considering the contribution of the BIB at $\sqrt{s} = 1.5$ TeV, a marked difference is observed compared to the case without BIB. This demonstrates how the BIB particles have a notable impact on the performance of the electromagnetic calorimeter. However, the result obtained does not deviate too much from the resolution benchmark within $10\%/\sqrt{s}$ for the Muon Collider. This indicates that the CRILIN continues to represent an excellent calorimeter option.

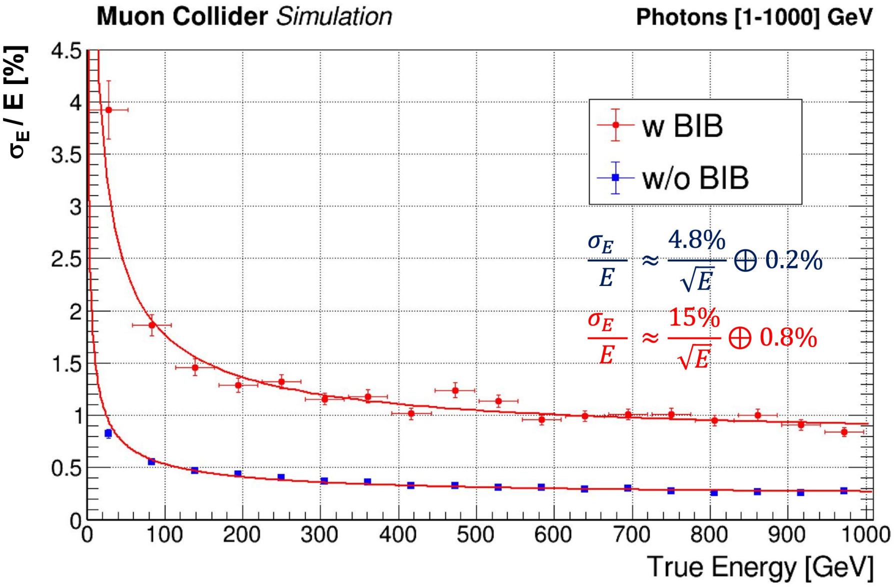

Figure 5.8: Trend of the energy resolution of the CRILIN electromagnetic calorimeter. In blue is the case without the presence of the BIB and in red is the case with the contribution of the BIB particles. These results refer to the 5-layer CRILIN configuration used in the design of the Muon Collider detector for a center-of-mass energy of 1.5 TeV.

5.3 The $\sqrt{s} = 10$ TeV Beam-Induced Background in the electromagnetic calorimeter

In addition to the study of the performance of CRILIN conducted with the detector configuration for a center-of-mass energy of 1.5 TeV, during my thesis, I also carried out a first study of the performance of CRILIN in the context of the development of the detector design for $\sqrt{s} = 10 TeV$. In this study, based on the detector configuration presented in Chapter 2, I initially focused on the detailed characterization of the BIB at a center-of-mass energy of 10 TeV at the CRILIN electromagnetic calorimeter.

The first step of this study consisted of simulating the passage of particles of a BIB sample at $\sqrt{s} = 10$ TeV, coming from the MDI and crossing the detector, considering the MUSIC geometry described in chapter 2. The SimHits obtained were subsequently processed through a trimming procedure, in which only the hits within a time window of [-1, 25] ns with respect to the passage of the bunch were retained. This choice was motivated by the need to reduce the number of SimHits due to computational limitations, focusing on the most relevant time range.
The next step was the digitization process of the SimHits generated by the BIB sample. In this phase, the same signal integration interval of [-1, 25] ns used for trimming was adopted, thus obtaining the corresponding DigiHits.

The characterization of the BIB in the electromagnetic calorimeter, both in the barrel and in the endcap, was performed by studying the DigiHits and comparing them with those related to different photon samples with discrete energies of 1, 10, 100, and 500 GeV, as defined in 5.1.

Figures 5.9 and 5.10, respectively related to the barrel and the endcap, show the normalized DigiHit number in the six CRILIN layers, comparing the contribution of the BIB (indicated in red) with that of the single monochromatic energy photon samples, as specified by the colors in the legend. It is observed that, both for the endcap and for the barrel, the BIB presents most of its hits in the first layer: about 40% for the barrel and about 48% for the endcap. Subsequently, the hit fraction progressively decreases as the layer increases. This trend reflects the spatial distribution of the hits generated by the BIB, with a higher concentration in the first layers of the calorimeter. For the signal samples, it is observed that the maximum value of the count fraction moves deeper into the calorimeter as the photon energy increases. This phenomenon is directly related to the greater extension of the electromagnetic shower development, which increases with the particle energy. In particular, the sample with an energy of 1 GeV shows the maximum at the second layer of the calorimeter, while the sample with an energy of 500 GeV shows the maximum at the fifth layer. This shift towards deeper layers is indicative of the increase in the particle energy and the consequent amplification and diffusion of the shower.

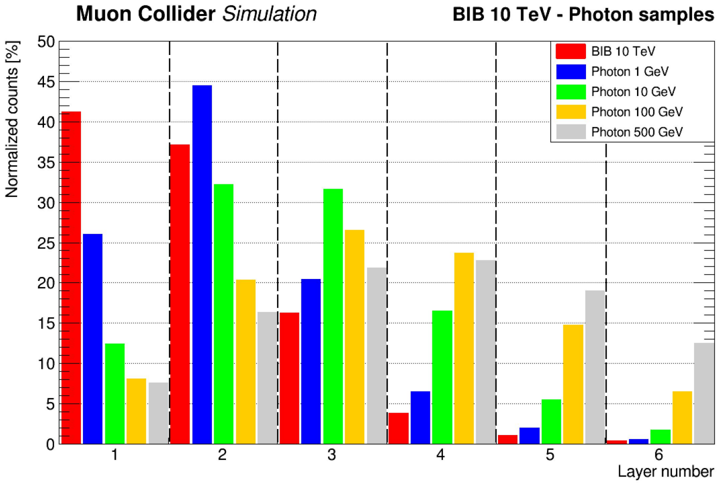

Figure 5.9: Histogram representing the fraction of the number of DigiHits as a function of the CRILIN calorimeter layer at the barrel region. The red color indicates the contribution of the BIB, while the 1, 10, 100, and 500 GeV photon samples are indicated with the colors in the legend.

Figures 5.11 and 5.12 illustrate the energy fraction of the DigiHit as a function of the CRILIN layer, for the barrel and the endcap, respectively. In this context, the energy fraction represents the percentage of the total energy deposited in the calorimeter that is attributed to each layer. The red dashed line indicates the contribution of the BIB sample, compared with the results obtained by analyzing the single photon samples at different energies. This comparison allows the visualization of how the BIB energy is distributed across the various layers and how it compares

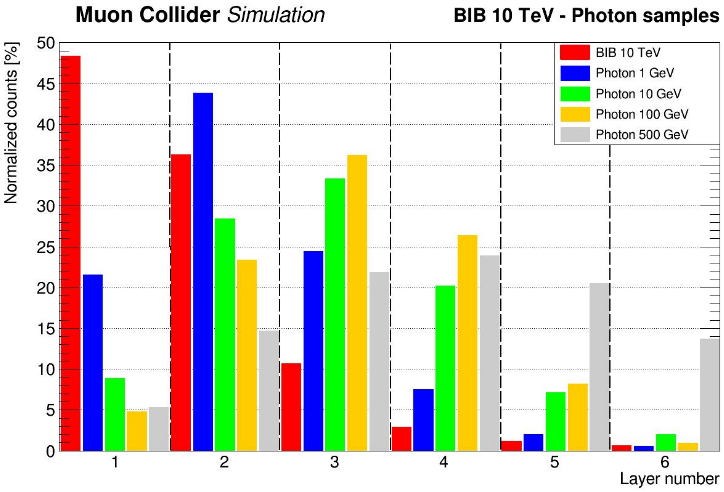

Figure 5.10: Histogram representing the fraction of the number of DigiHits as a function of the CRILIN calorimeter layer at the endcap region. The red color indicates the contribution of the BIB, while the 1, 10, 100, and 500 GeV photon samples are indicated with the colors in the legend.

with the energy distributions of the photon showers at different energies. It is observed that, similarly to what was found in the histograms related to the number of counts, the energy fraction related to the BIB particles shows a decreasing trend as the CRILIN layer increases. In particular, it is noted that most of the energy is deposited in the first layer, with values reaching about 80% for the barrel and 75% for the endcap. On the contrary, the distribution of the energy fraction for the various photon samples is more uniform in the first CRILIN layers. Furthermore, following the development of the electromagnetic shower, the position of the maximum of the deposited energy moves progressively deeper as the photon energy increases.

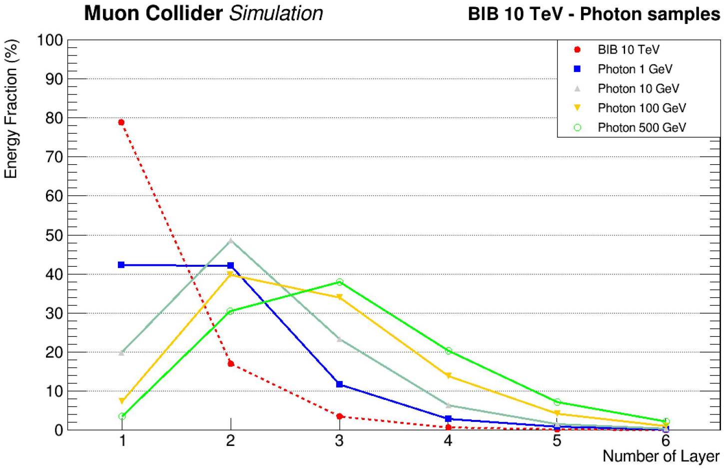

Figure 5.11: Trend of the DigiHit energy fraction as a function of the CRILIN layer in the barrel region. The red dashed line represents the contribution of the BIB at a center-of-mass energy of 10 TeV which is compared with the photon samples with energies of 1, 10, 100, and 500 GeV indicated with the colors in the legend.

From this first study of the BIB at $\sqrt{s} = 10$ TeV at the electromagnetic calorimeter, it emerged that the first layers of CRILIN are the ones most subject to the impact of the BIB particles. This result indicates the need to optimize the mitigation of the BIB effects in the detector calorimetric system by paying more attention to the first layers. This requires a careful analysis of the BIB characteristics and the development of effective strategies to reduce as much as possible the number of DigiHits.

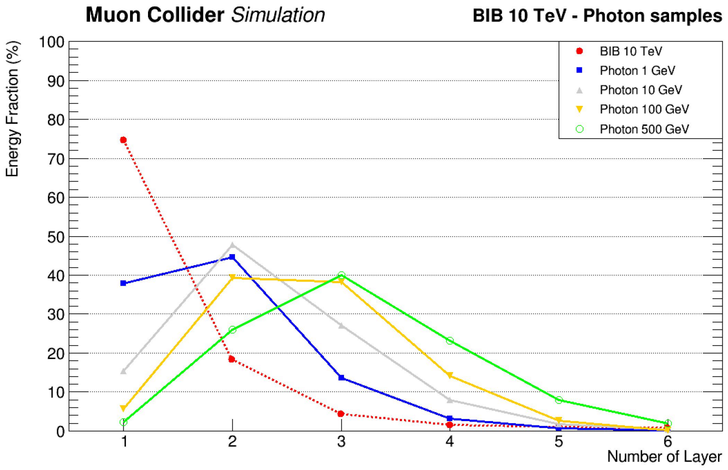

Figure 5.12: Trend of the DigiHit energy fraction as a function of the CRILIN layer in the endcap region. The red dashed line represents the contribution of the BIB at a center-of-mass energy of 10 TeV which is compared with the photon samples with energies of 1, 10, 100, and 500 GeV indicated with the colors in the legend.

5.3.1 Study for the CRILN digitization for $\sqrt{s} = 10$ TeV collision

After this preliminary study on the characteristics of the BIB at $\sqrt{s} = 10$ TeV in the CRILIN calorimeter, the second phase of this research focused on optimizing the digitization process of the electromagnetic calorimeter in order to improve BIB mitigation at ECAL.

During the the study at $\sqrt{s} = 1.5$ TeV in section 5.2,in the digitization procedure only energy thresholds were applied, varying as a function of the CRILIN layer and the spatial region, while the acquisition time window was constant for all layers equal to [-0.25, 25]ns.
The strategy I applied to optimize the selection of hits due to BIB consists of implementing not only variable energy thresholds but also appropriate acquisition time windows differentiated depending on the layer and the spatial region. This approach aims to exploit the high temporal resolution offered by CRILIN to improve BIB mitigation, eliminating the asynchronous component of the BIB with respect to the signal. Consequently, this would allow to further lower the energy thresholds respect the $\sqrt{s} = 1.5$ TeV studies, improving the performance of CRILIN in terms of energy resolution in the presence of BIB.

To identify the aforementioned appropriate selection requirements for the DigiHits, I conducted an analysis study on the time-energy correlation of the DigiHits comparing them betweem the BIB sample with the monochromatic energy photon samples, for each layer of CRILIN.
The two-dimensional histograms obtained from this study with photon sample at 100 GeV are shown in Figures 5.14 to Figure 5.19, where the x-axis represents the arrival time of the hits, while the y-axis reports the corresponding energy. The DigiHit time displayed in the histograms has been corrected considering the propagation time of the particle in relation to the position of the hit in the specific CRILIN cell.

From these histograms, we can make some observation. By looking at the time-energy distributions it is possible to see the presence of BIB hotpots in the positive time range that correspond to the time interval of interest of the signal. Therefore, it is difficult to find appropriate time-energy requirements for a proper energy resolution study and, due to the very high number of BIB particles on the CRILIN layers, it was observed that the clustering procedure does not work properly. This can be used to prove that the BIB at $\sqrt{s} = 10TeV$ presents a different behaviour with respect to the one at $\sqrt{s} = 1.5TeV$.

To address this issue, it will be necessary to optimize the clustering algorithm of the calorimetric system for the BIB at 10 TeV center of mass energy, which takes into account not only spatial but also temporal information. Also a novel nozzles design, as the one showed in Figure 5.20, should be considered since the current one was optimized for BIB at 1.5 TeV.

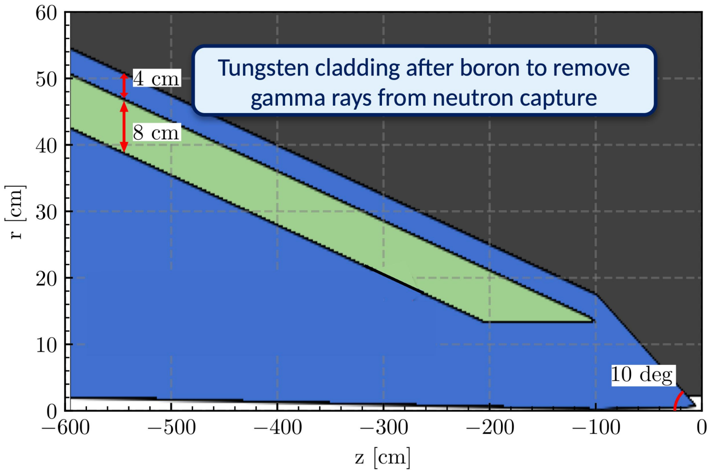

Figure 5.13: Longituninal section of new nozzle design proposed for the 10 TeV center of mass energy detctor. [61]

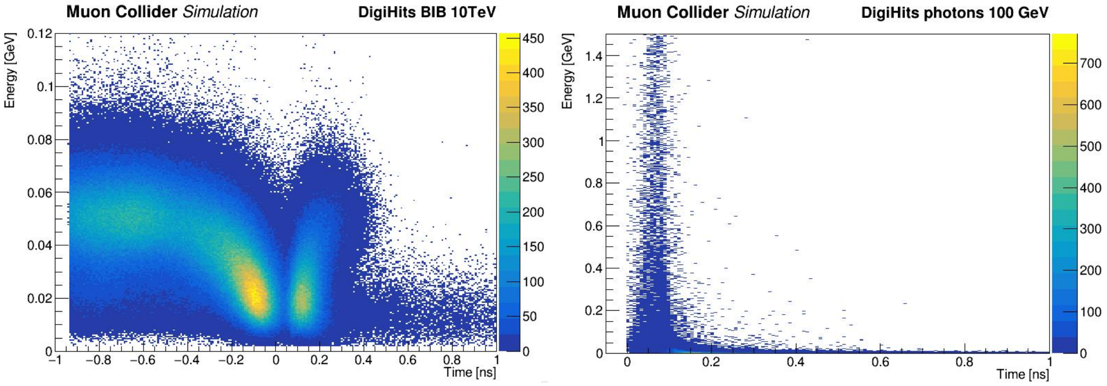

Figure 5.14: Time-energy distribution of the DigiHit on the first layer of CRILIN. Left: $\sqrt{s} = 10$ TeV BIB. Right: 100 GeV photons.

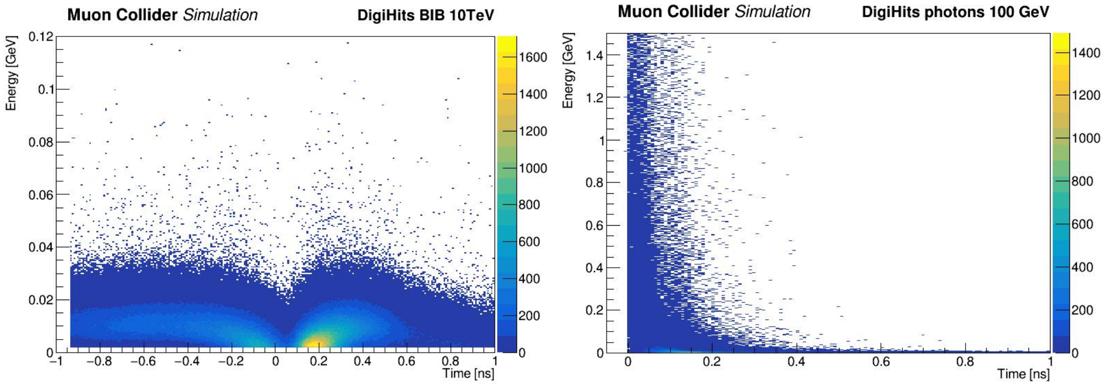

Figure 5.15: Time-energy distribution of the DigiHit on the second layer of CRILIN. Left: $\sqrt{s} = 10$ TeV BIB. Right: 100 GeV photons.

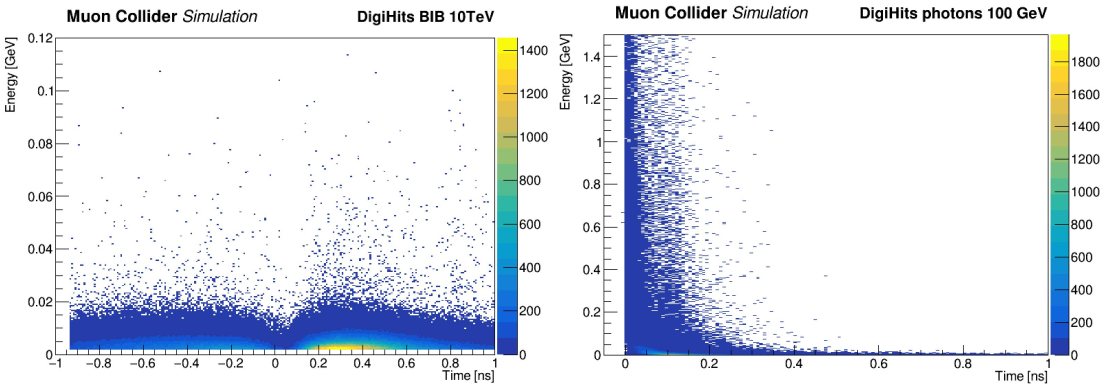

Figure 5.16: Time-energy distribution of the DigiHit on the third layer of CRILIN. Left: $\sqrt{s} = 10$ TeV BIB. Right: 100 GeV photons.

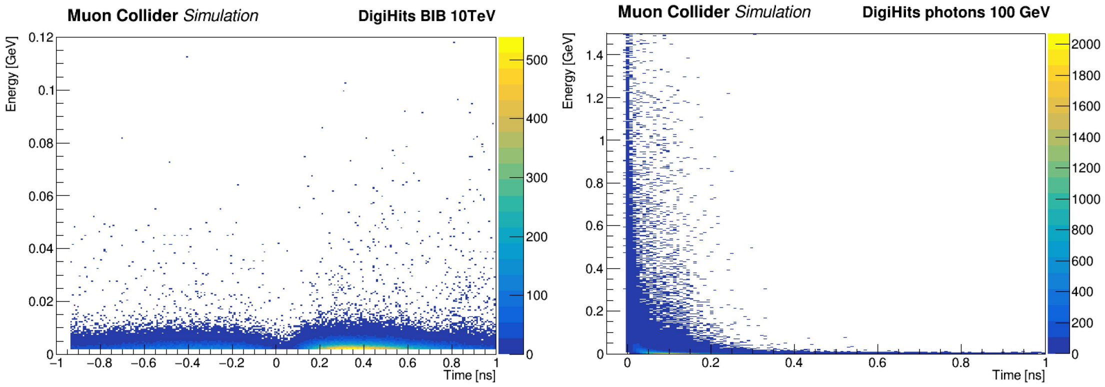

Figure 5.17: Time-energy distribution of the DigiHit on the fourth layer of CRILIN. Left: $\sqrt{s} = 10$ TeV BIB. Right: 100 GeV photons.

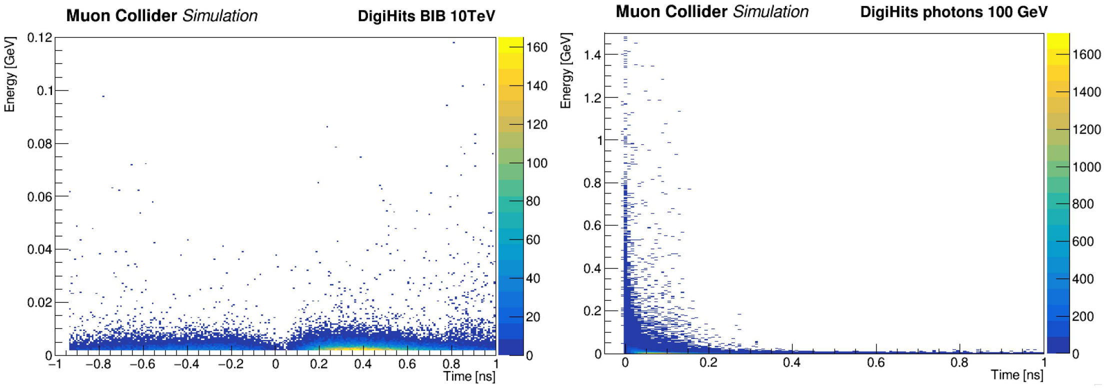

Figure 5.18: Time-energy distribution of the DigiHit on the fifth layer of CRILIN. Left: $\sqrt{s} = 10$ TeV BIB. Right: 100 GeV photons.

5.4 Electromagnetic shower containment

This section presents a study on the containment of electromagnetic showers generated by photons with energies ranging from 1 GeV to 1 TeV. The study is based on the two photon samples described in the previous section 5.1. The results are for two configurations of CRILIN ECAL with 5 layers and 6 layers of crystals.

The energy containment analysis is based on the SimHits at the simulation level in the electromagnetic calorimeter. For each photon event, the energy containment ratio, denoted by K_E, is calculated. This ratio is defined as the sum of the energy of the SimHits in the CRILIN ECAL, divided by the true level photon energy (E_{True}).

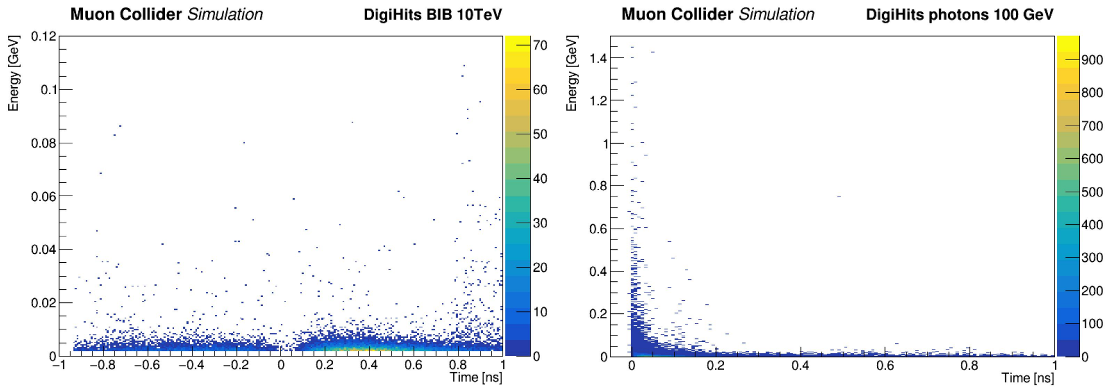

Figure 5.19: Time-energy distribution of the DigiHit on the sixth layer of CRILIN. Left: $\sqrt{s} = 10$ TeV BIB. Right: 100 GeV photons.

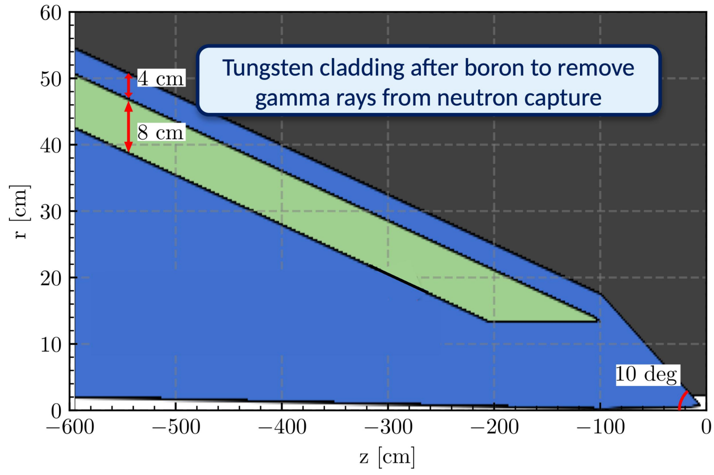

Figure 5.20: Longituninal section of new nozzle design proposed for the 10 TeV center of mass energy detctor. [61]

$$K_E = \frac{\sum E_{Hits\ Ecal}}{E_{True}} \tag{5.5}$$

By dividing the true energy range and the true polar angle (θ) range into bins of constant width and analyzing the average value of the energy containment ratio (K_e) for each bin, it is possible to examine the shower energy containment as a function of the energy and the polar angle. Figure 5.23, compares the energy containment of the electromagnetic shower as a function of the true level energy, comparing the result for CRILIN ECAL with 5-layer (red) and 6-layer (blue) configurations. For both configurations, a decreasing trend of shower containment is observed as the photon energy increases. In the 6-layer case, the values vary between 92.5% and 91.4%, while the 5-layer configuration presents an overall worsening of the containment, with a greater dependence on energy and values between 91.6% and 87.5%.

Figure 5.22 compares the shower energy containment trend as a function of polar angle for the 5- and 6-layer configurations. The vertical lines indicate the angular range in which the photons were generated. In both configurations, the minimum shower containment is observed at 90°, while at more forward angles, the containment is higher. This effect, more visible in the case with 5 layers, is due to the varying amount of material traversed by the shower, which is minimal in the direction orthogonal to the barrel.

The results of this study show that a 6-layer configuration of the CRILIN electromagnetic

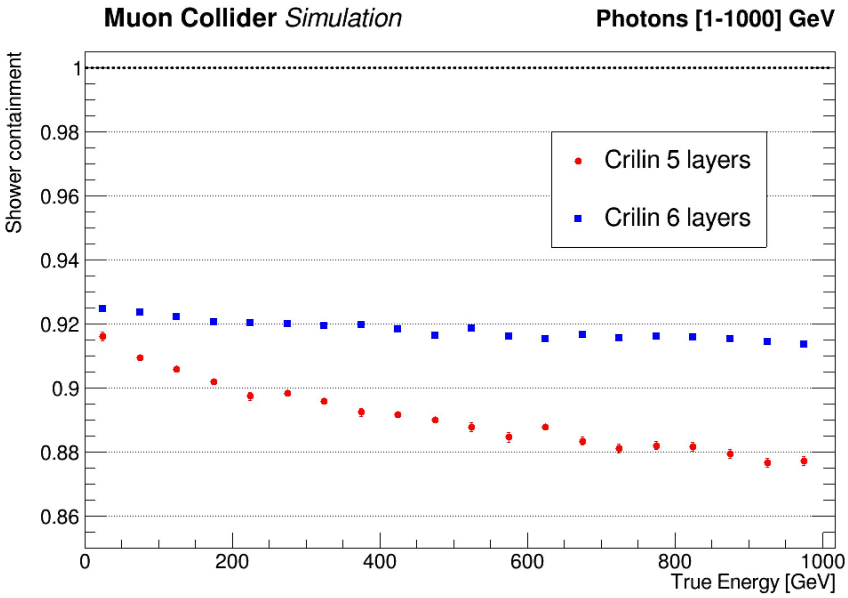

Figure 5.21: Average values of the K_E ratio of the shower energy containment as a function of the photon energy at the true level. In red are the results for the 5-layer CRILIN configuration and in blue are the 6-layer case.

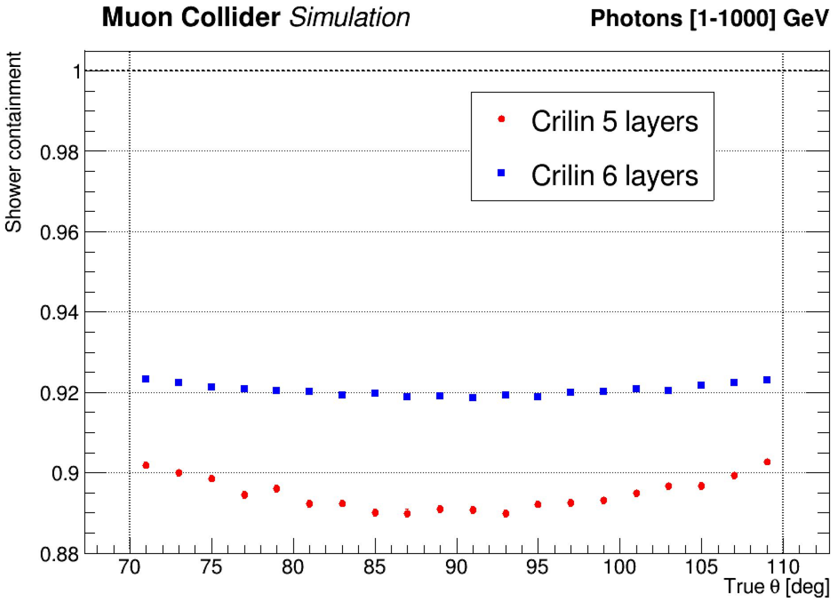

Figure 5.22: Average values of the K_E ratio of the shower energy containment as a function of the polar angle at the true level. In red are the results for the 5-layer CRILIN configuration and in blue are the 6-layer case. The vertical lines indicate the angular range of the sample.

calorimeter provides good energy containment of electromagnetic showers up to 1 TeV. The analysis shows that moving from a 5-layer to a 6-layer configuration provides a significant improvement in energy containment, with an increase of about 3%, compared to an increase of about 4 radiation lengths.

5.5 Alternative detector design proposal for the 10 TeV center of mass energy

Within the discussion to find the optimal design for the Muon Collider detector at the $\sqrt{s} = 10$ TeV stage, there is an alternative proposal in addition to the MUSIC configuration presented

in the Chapter 2. The main difference with respect to the MUSIC detector design is related to the position of the superconductive solenoid. In this case, the solenoid is placed between the tracking system and the electromagnetic calorimeter.
This solution allows for a more uniform magnetic field within the tracking system and makes it easier to achieve a higher magnetic field strength, around 5T, from a construction perspective. Moreover it can help to shield the calorimeter system form the BIB particles.
However, having the solenoid placed in front of the calorimetric system requires careful study to optimize the calibration in energy of the ECAL.

Using the sample of 15000 photons with energy between 1 GeV and 1000 GeV I conducted a preliminary study on the energy resolution that can be achieved with this detector configuration. Applying the same procedure described in section 5.2.3 for the study of the energy resolution, Figure 5.23 shows the result obtained in this case witout the contribution of the BIB.

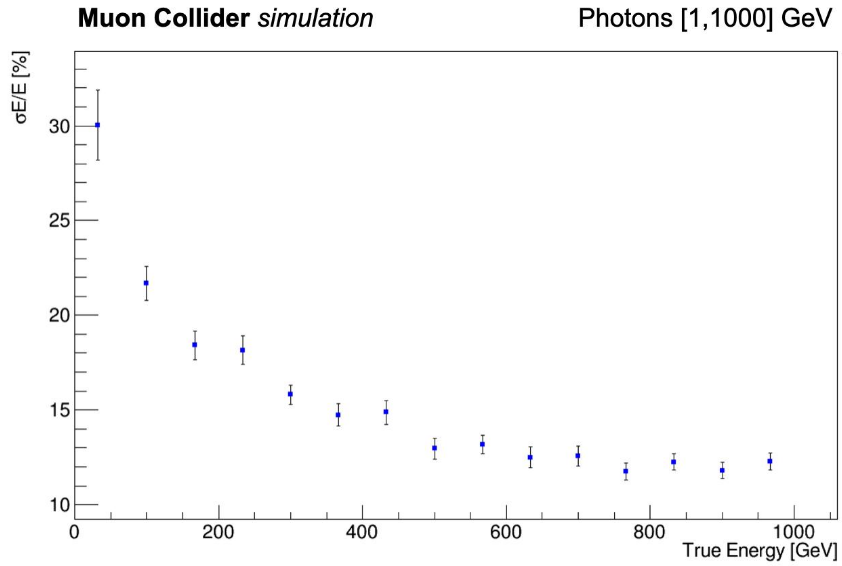

Figure 5.23: Energy resolution values for the detector configuration featuring a solenoid placed between the tracking system and ECAL.

Comparing this to the result obtained in the absence of the BIB presented in 5.2.3 it is evident that the energy resolution has significantly worsened. This is mainly due to the degradation in reconstructed energy that occurs due to the presence of the solenoid in front of the calorimeter system.

Chapter 6

Preliminary CRILIN prototypes tests

Since 2021, initial experimental tests have been conducted to assess the feasibility of a technology based on semi-homogeneous device for ECAL in high energy muon collisions [62], and subsequent years have seen tests of dedicated prototypes. The experimental tests conducted thus far have been crucial in verifying the correct operation of this device and providing a preliminary assessment of its performance. This chapter will present an overview of the state-of-the-art in prototype development, along with the main results obtained from these preliminary tests.

6.1 Description of the Prototypes

Two distinct prototype models have been developed labeled Proto-0 and Proto-1. Special attention is given to Proto-1, which currently represents the most advanced and fully developed prototype available. A detailed description will be provided of the front-end electronics component that has been developed for Proto-1, as well as the cooling system.

6.1.1 Prototype model Proto-0

Proto-0 is the first prototype of CRILIN constructed, as illustrated in Figure 6.1. The structure has two PbF_2 crystals, each measuring 10x10x40 mm^3, arranged in a single layer housed in a mechanical structure, made from Acrylonitrile Styrene Acrylate (ASA), of dimensions 61x40x44 mm^3 (in black in 6.1 right). The crystals are directly coupled to a 2x2 matrix of silicon SiPMs. Specifically, Hamamatsu S14160-3010PS SMD SiPM model [63], with dimensions 3x3 mm^2 and a pixel size of 10 μm. They are installed on a dedicated printed circuit board referred to as SiPM Board (in green in Figure 6.1 left). The optical coupling between the crystals and the SiPMs is achieved through direct contact, without the use of optical grease.

6.1.2 Prototype model Proto-1

The Proto-1 prototype, shown in Figure 6.2, represents an evolution of the Proto-0 design, with two layers of 3x3 matrices of crystals. Each crystal, of dimensions 10x10x40 mm^3, is directly coupled to a 2x2 matrix of SiPMs, similar to the configuration of Proto-0. The transverse and longitudinal dimensions of this prototype are characterized by a Moliere Radius (R_M) of 0.7 and a total radiation length (X_0) of 8.5, respectively.
Figure 6.2 (left) illustrates the assembly of Proto-1, showing that the structure consists of two stacked modules (indicated in blue). Each module is equipped with a dedicated SiPM Board, which will be described in detail in 6.1.3. The prototype has a cooling system of the SiPMs,

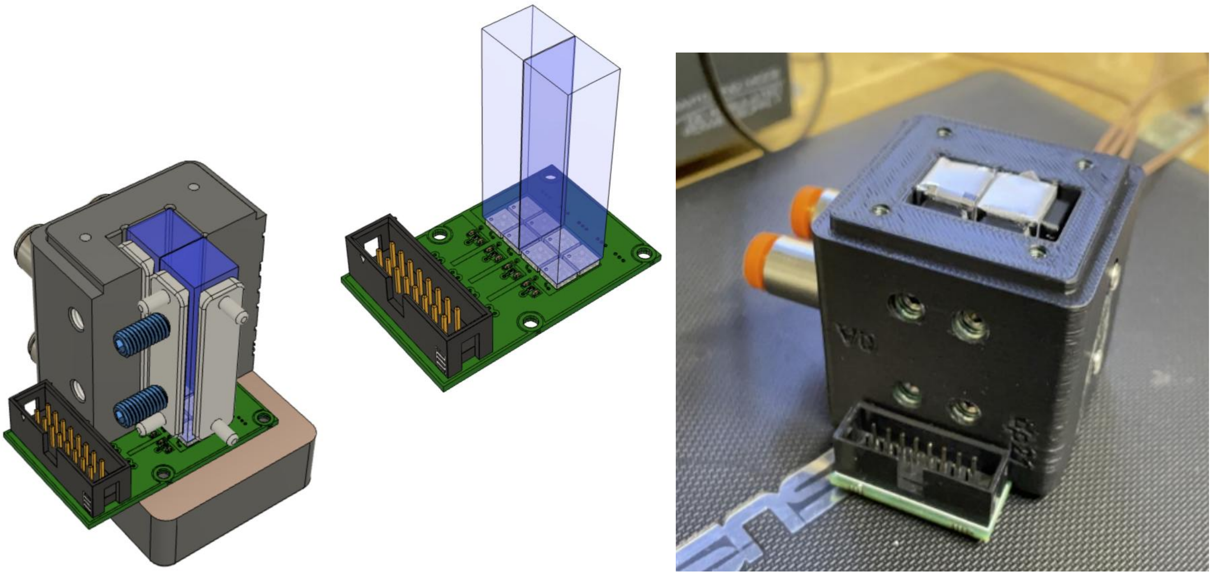

Figure 6.1: Left: 3D renderings of the Proto-0 prototype layout. The pair of PbF_2 crystals is shown in blue and a section of the mechanical structure in black. In green the SiPM board and the SiPMs matrix are shown in the central figure[58]. Right: photo of the Proto-0 fully assembled for the experimental tests.[56]

hydraulically connected and placed on the lateral side of the prototype and visible in blue in Figure 6.2 (right).

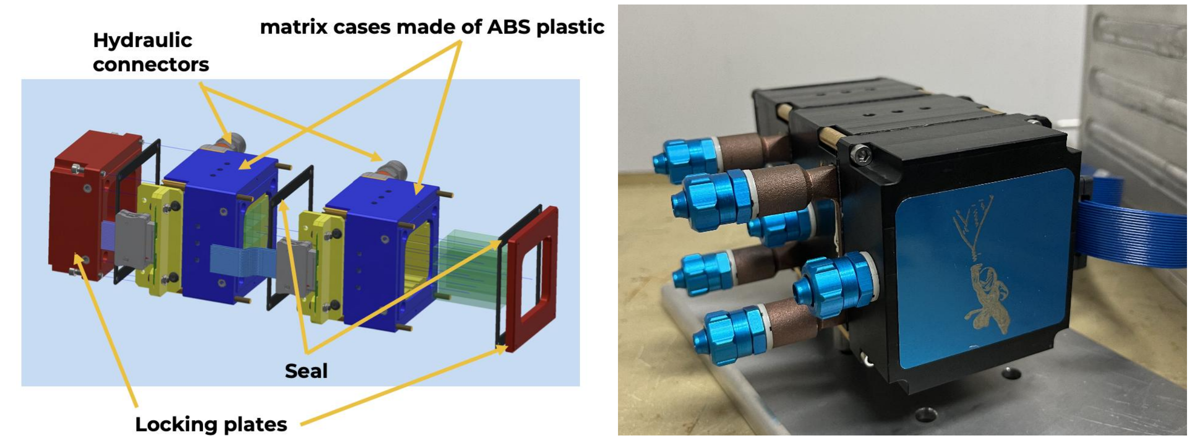

Figure 6.2: Right: rendering of the assembly of Proto-1 with the various components that form the two modules. Left: Photo of Proto-1 fully assembled.[56]

6.1.3 The Front-End electronics

The front-end electronics for the Proto-1 prototype consist of two main components: the SiPM Board and the Mezzanine Board.

The SiPM Board

Figure 6.3 shows a front (right) and back (left) photo of the SiPM Board used for a single layer of Proto-1. In Figure 6.3 left, the arrangement of the SiPMs can be seen; each crystal is connected to one of the 2x2 matrix of SiPMs. This setup enables two independent readout channels per crystal, achieved by connecting a pair of SiPMs from the 2x2 matrix either in series or parallel. Consequently, a single layer of Proto-1 provides a total of 18 readout channels. The SiPMs used are Hamamatsu S14160-3015PS SMD models, measuring 3x3 mm^2 with a pixel size of 10 μm. As will be justified in the next section, the choice of this specific model is related to the

minimization of the dark current due to the flux of BIB particles expected in the Muon Collider detector environment.
From the Figure 6.3 left it is possible to notice that four 0603 SMD blue LEDs are installed among the SiPM groups. The light produced by the LEDs allows us to perform diagnostic checks by monitoring the SiPMs's response and carry out an in-situ calibration. On the right side of Figure 6.3, the socket for cable connections is visible in black.

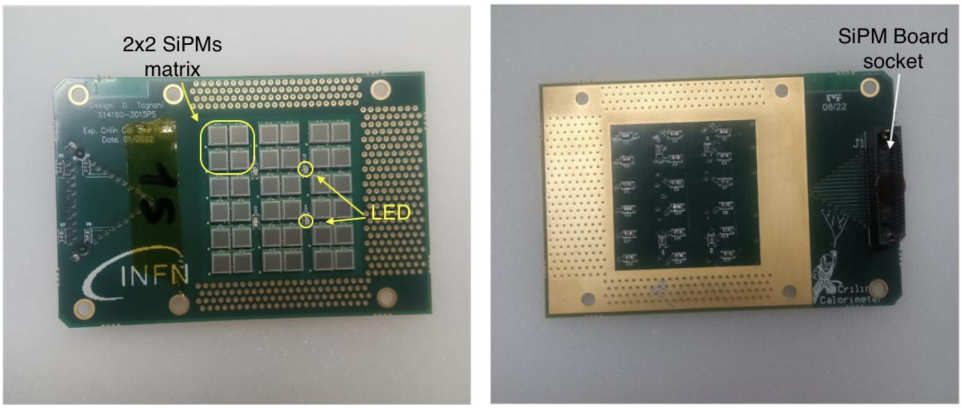

Figure 6.3: Photo of the SiPM board model produced for the Proto-1 of CRILIN. The left image shows the front side, where each crystal is connected to a 2x2 matrix of SiPMs, highlighted in yellow. [55]. The right photo represents the back side of the board with the cable connector.[55]

The Mezzanine Board

The Mezzanine Board is connected to the SiPM Board via 50-ohm micro-coaxial transmission line (Samtec ERCD-040-40.00-TEU-TED-1-D). These lines are used both to supply the bias voltage to the SiPMs and to transmit the generated signals in output to the Mezzanine Board. Figure 6.4 shows a 3D rendering of the Mezzanine Board designed for the Proto-1 prototype. Specifically:

- The signal from each of the 18 SiPM channels in a single layer undergoes amplification and shaping processes. In particular, the signals are terminated adequately to avoid reflections and are subjected to a first non-inverting amplification step with a gain value of 4. After which the signal is processed by a pole-zero cancellation circuit, which allows the elimination of signal distortions due to the electronic components, and a second non-inverting amplification stage with gain 2 is then applied. Consequently, the signal, following a total amplification with gain 8, is ready to be digitized with a dynamic range of 2 V.
- On-board SiPM biases are provided by 18 high-voltage linear regulators, which offer a range of 0-100 V and can source up to 5 mA of current. These regulators deliver precisely adjustable bias voltages with 0.24 V resolution, controlled by 12-bit DACs. They have minimal ripple and fast settling times. The system also includes high-voltage current sense amplifiers for monitoring individual bias currents and 12-bit ADCs for measuring regulated voltages, bias currents, and the temperature of the SiPM matrix. A Cortex M4 microprocessor manages all slow control functions and monitors the status of each readout channel.

6.1.4 Cooling system

After irradiation, SiPMs experience an increase in temperature, which leads to a rise in dark current. Given an expected radiation dose in the Muon Collider calorimeter of 1-MeV-neq fluence of $10^{14}\,\mathrm{n_{1MeV}/cm^2}$, the total thermal load is estimated to be 350 mW per crystal cell (with 4 SiPMs). The implementation of the cooling system is necessary to maintain the signal-to-noise ratio as low as possible and the SiPM response stable during the acquisition. The system is

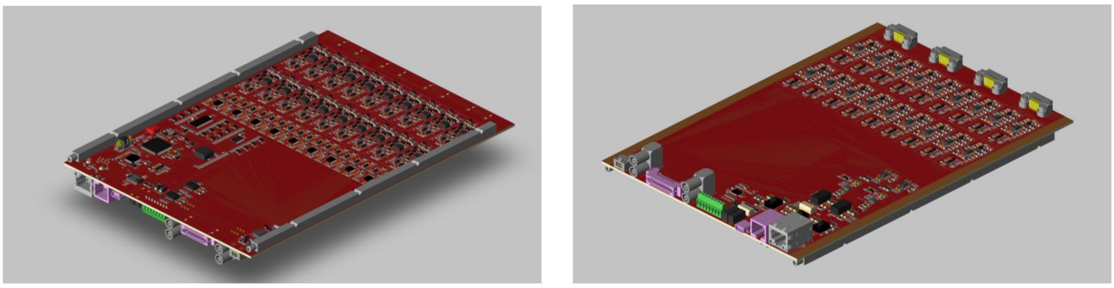

Figure 6.4: 3D rendering of the Mezzanine Board designed for CRILIN Proto-1 prototype. The two figures represent the two sides of the card. [55]

designed to maintain the reference operating temperature at approximately 0°C.
Figure 6.5 shows two photos of the cooling system for Proto-1. It consists of a copper cold plate through which a glycol-water solution circulates. Its internal structure has micro-channels that enhance heat exchange with the SiPM Board while maintaining a compact cooling system design. The refrigerant liquid is supplied by a cooling plant connected to the plate via hydraulic connectors (shown in blue in Figure 6.5 right). As illustrated in Figure 6.5 (left), the cold plate is in direct contact with the back side of the SiPM Board. The right side of the figure shows the two modules with their respective cooling systems installed.

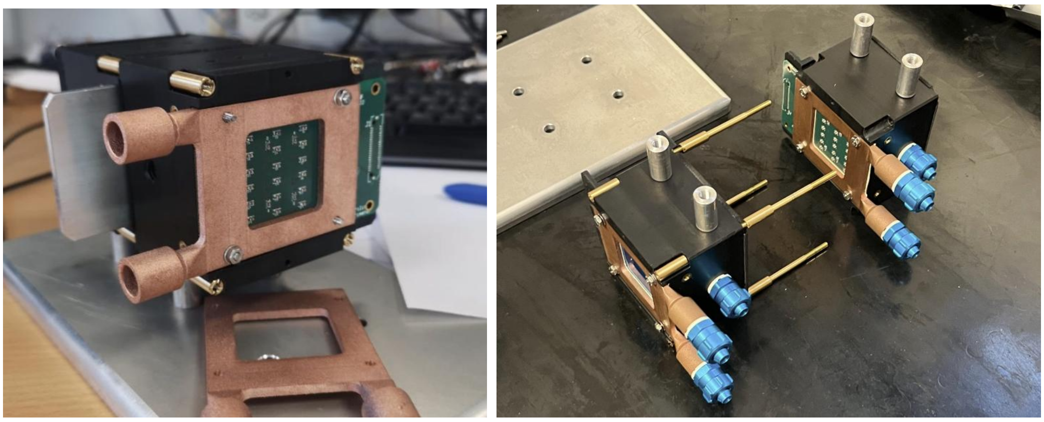

Figure 6.5: Left: Photo of the cold plate in direct contact with the back of the SiPM Board. Right: View of the two Proto-1 modules separated. The cold plates of the respective modules are visible, with the hydraulic connectors for the coolant flow highlighted in blue. [55]

6.2 Prototype components characterization

Before testing the prototypes with dedicated beam tests, it was crucial to thoroughly study the characteristics of the individual components of the CRILIN ECAL prototype. This section will outline the tests conducted on the crystals, SiPMs, and electronics to verify their proper functionality and resistance to radiation.

6.2.1 Test of the crystals

As outlined in Chapter 4, PbF_2 crystals were chosen for the CRILIN technology. The choice was based on the characteristics that this crystal presents, compared to other types of crystals used in calorimetry. PbF_2 crystals are an excellent material for generating Cherenkov radiation and this is a key feature to achieve good temporal resolution performance. Additionally, PbF_2 crystals exhibit excellent transmittance in the ultraviolet light region down to wavelengths (λ) of 240 nm. This feature is highly advantageous because the Cherenkov photon yield peaks at shorter wavelengths, as indicated by Equation 6.1, choosing to implement these crystals highly compatible for application in CRILIN.

$$dN \ \alpha \ \frac{d\lambda}{\lambda^2} \tag{6.1}$$

In table 6.1 the main characteristics of the PbF_2 crystal compared to those of the PWO-UF (Lead Tungstate Ultra-Fast) crystal, which has also been considered for the CRILIN calorimeter, are presented.

Crystal	PbF_2	PWO-UF
Density [g/cm^2]	7.77	8.27
Radiation length [cm]	0.93	0.89
Molière radius [cm]	2.2	2.0
Decay constant [ns]	-	2.2
Refractive index at 450 nm	1.8	2.2
Manufacturer	SICCAS	Crytur

Table 6.1: Characteristics of PbF_2 and PWO-UF crystals. [58]

The characterization of the crystals involved the study of the deterioration of the transmittance of the PbF_2 crystal following the irradiation with both photons and neutrons. For this study, two samples of PbF_2 crystals sized 5x5x40 mm^3 were considered, with the first one left unwrapped ("naked") and the second one wrapped in a mylar sheet with a thickness of 100 μm. These crystals were both produced by the same company using a melt-growth procedure.
The transmittance was measured using a PerkinElmer Lambda 950 UV/VIS dual-beam spectrometer, considering the longitudinal direction of the crystal. In general, optical transmittance, defined as the ratio of the intensity of light transmitted through the material to the initial intensity, was calculated using the following relationship 6.2:

$$T = \frac{\frac{S-D}{Ref-D}}{\frac{S_0-D_0}{Ref_0-D_0}} \tag{6.2}$$

where S is the measured signal, D the dark signal, Ref the reference signal and Ref_0 the refernce signal without a crystal in the apparatus.

Figure 6.6 presents the result of the longitudinal transmittance measured before the irradiation of the two crystals: one without wrapping and the other with the mylar wrapping.

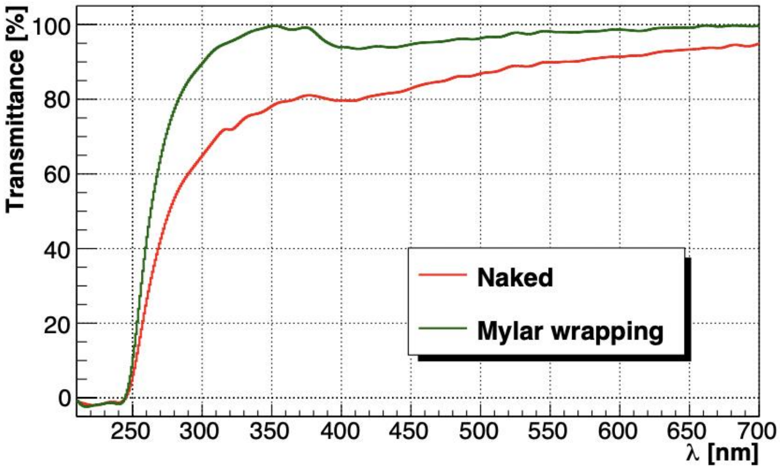

Figure 6.6: Longitudinal transmittance measured before the irradiation of the samples. [62]

The initial phase of crystal irradiation was conducted using photons. This procedure took place at Calliope (Casaccia, Italy), which is a pool-type gamma irradiation facility equipped with a rack of 25 Co^{60} sources arranged in a planar geometry, with a measured activity at the time of irradiation of 1.97 x 10^{15} Bq. The energy of the emitted photons, with a value of 1.25 MeV, is similar to the average energy of photons from BIB (1.8 MeV). Therefore, this test enables a fairly faithful reproduction of the experimental environment conditions expected for the electromagnetic calorimeter in a Muon Collider detector.
The absorbed dose rate, with the crystal under analysis positioned 70 cm from the radioactive source, was 100 krad/h, and 5 irradiation steps were conducted, as summarized in Table 6.2. The total dose given to the two crystal samples was 4.4 Mrad.

Irradiation step	Dose in the air [Krad]
I	30.2
II	89.88
III	2082
IV	4031.8
V	4435.5

Table 6.2: Values of the cumulative radiation dose given to the PbF_2 crystal sample for each irradiation step. [62]

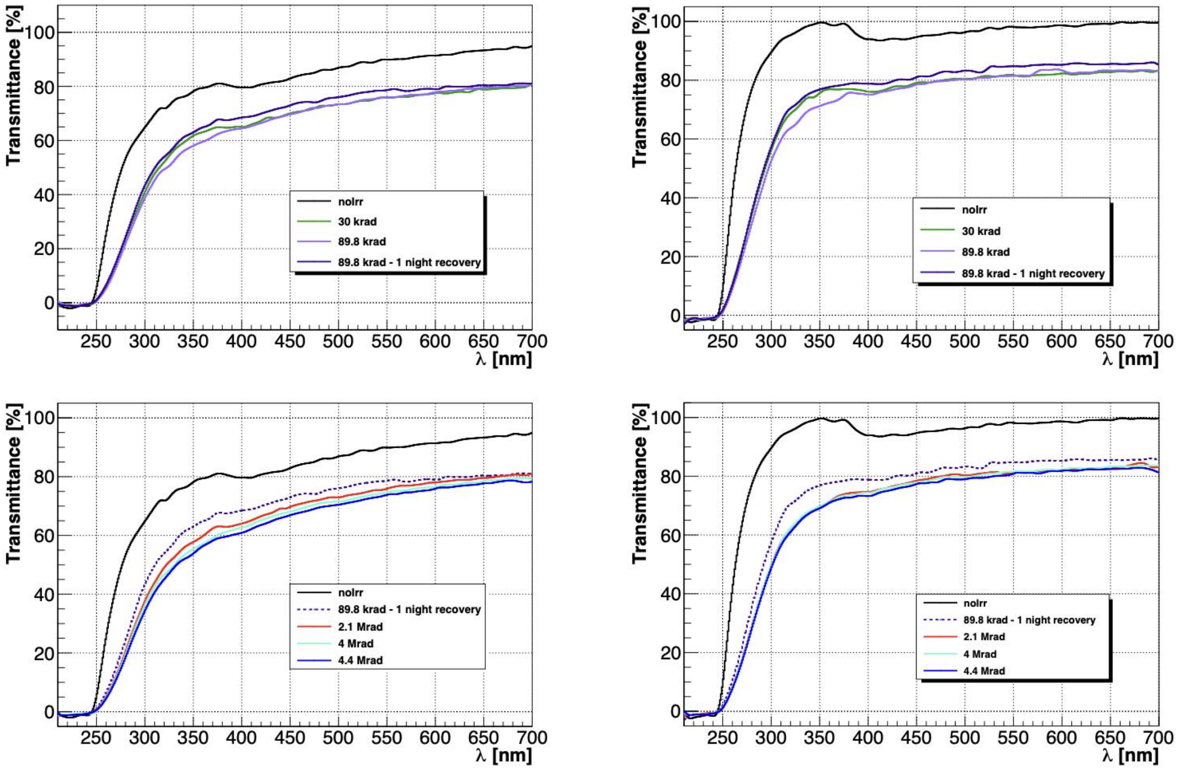

Figure 6.7: Trasmittance measurements after step I and II. Left: naked crystal. Right: crystal with Mylar wrapping.[62]

Following each irradiation step, a transmittance measurement was conducted. Figure 6.7 presents the results for both crystals, with the left plots showing the crystals with wrapping and the right column those without wrapping. In particular, the figures of the upper row show the result after the first two irradiation steps (I and II of Table 6.2), illustrating a noticeable deterioration in transmittance compared to the black line representing the pre-irradiation case. Meanwhile, the figures on the bottom row show the measurements for the remaining irradiation steps. It is possible to notice a saturation effect of the degradation due to the absorbed doses exceeding 89 krad. The maximum degradation of transmittance was observed to be around 40%.

After photon irradiation but before the neutron irradiation, the crystals' ability to repair radiation-induced damage was tested. The crystals were placed inside a light-tight box and exposed to blue light with a wavelength of 400 nm. Figure 6.8 compares the radiation damage recovery effect after 16 hours of blue light exposure (green line) with natural recovery after 18 days post-irradiation (orange line). It can be observed that, for both the wrapped crystal (left) and the naked crystal (right), a comparable recovery effect is achieved in a shorter time with blue light exposure.

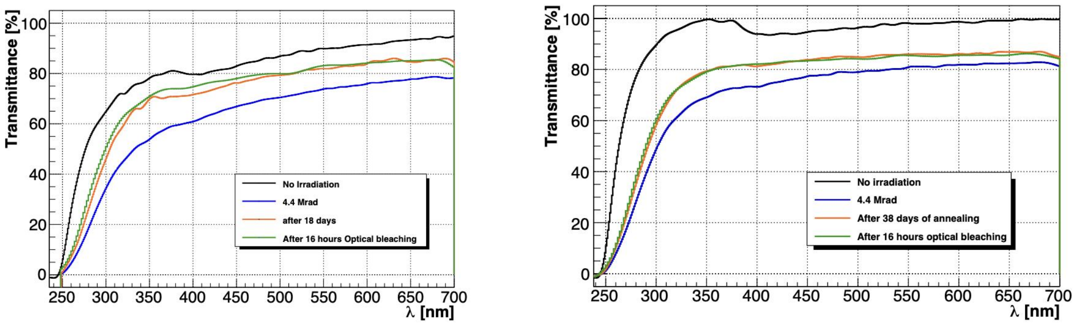

Figure 6.8: Comparison of the damage repair effect of 16 hours of treatment with blue light and 18 days in the dark. Right: crystal with Mylar wrapping.[62]

The second phase of crystal testing was conducted with neutron irradiation at the Frascati Neutron Generator (FNG) at ENEA, Frascati. This facility enables the generation of neutrons with a flux of up to 10^{12} n/s and an energy of 14 MeV. In this case, the crystal was positioned 1 cm from the source, and the total absorbed dose was negligible, on the order of 0.1 Krad.
In Figure 6.9, the result of transmittance measurements are presented, after a total irradiation duration of one hour and 30 minutes, with a total flux of 10^{13} neutrons/cm^2. It is notable that no significant differences in transmittance are observed, despite the measurement being conducted 14 days after irradiation due to transportation issues.

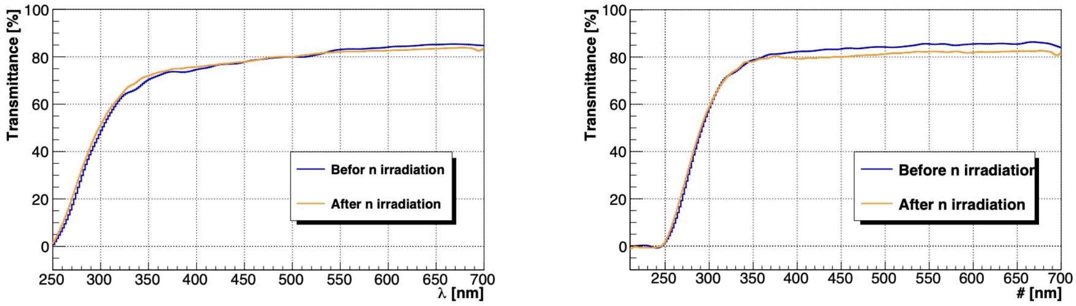

Figure 6.9: Transmittance measurements after 18 days from the neutron irradiation. Right: crystal with Mylar wrapping.[62]

The obtained results indicate that PbF_2 crystals exhibit excellent performance of radiation hardness, confirming their compatibility with the electromagnetic calorimeter requirements for a Muon Collider detector.

6.2.2 Test of SiPMs

Unlike crystals, where the primary source of radiation damage comes from the high flux of photons in the BIB, SiPMs are more susceptible to damage from neutron exposure. Neutrons in the BIB can penetrate the crystals and directly interact with the SiPM core, causing structural damage to the silicon lattice. This damage generally increases dark current. Consequently, in addition to the crystals, studies have also been conducted to assess the radiation hardness of the SiPMs [64]. In this case, two SiPM models were compared, with pixel sizes of 15 μm (SMD S14160-3015PS [63]) and 10 μm (S14160-3010PS), respectively. Irradiation was conducted with 14 MeV neutrons at a flux of up to 10^{14} n_{1MeV}/cm^2 at the Frascati Neutron Generator (FNG-ENEA)[65], monitoring the level of dark current generated after the irradiation. Table 6.3 presents the reference values of the dark current before irradiation for both SiPM models and at different bias voltage above the break down voltage (V_{br}).

Pixel Size	V_{br} [V]	I(V_{br} + 4V) [nA]	I(V_{br} + 6V) [nA]	I(V_{br} + 8V) [nA]
10 μm	80.97 ±0.01	23.89 ±0.01	42.58 ±0.01	70.80 ±0.01
15 μm	78.00 ±0.01	35.03 ±0.01	80.50 ±0.01	152.35 ±0.01

Table 6.3: Pre-irradiation dark current values compared for two SiPM models with pixel sizes of 10 μm and 15 μm at different bias voltages. [64]

Considering different temperature values, Table 6.4 and Table 6.5 display the dark current values measured post-irradiation, respectively for the SiPM model with a pixel size of 10μm and 15μm.

— Pixel size 10 μm —

T [°C]	V_{br} [V]	I(V_{br} + 4V) [nA]	I(V_{br} + 6V) [nA]	I(V_{br} + 8V) [nA]
-10±1	76.76 ±0.01	1.84 ±0.01	6.82 ±0.01	29.91 ±0.01
-5±1	77.23 ±0.01	2.23 ±0.01	9.66 ±0.01	37.51 ±0.01
0±1	77.49 ±0.01	2.99 ±0.01	11.59 ±0.01	38.48 ±0.01

Table 6.4: Dark current values after irradiation for SiPMs with a pixel size of 10μm at different bias voltages and temperatures.[64]

— Pixel size 15 μm—

T [°C]	V_{br} [V]	I(V_{br} + 4V) [nA]	I(V_{br} + 6V) [nA]	I(V_{br} + 8V) [nA]
-10 ±1	75.29 ±0.01	12.56 ±0.01	30.45 ±0.01	46.76 ±0.01
-5±1	75.81 ±0.01	14.89 ±0.01	32.12 ±0.01	46.77 ±0.01
0±1	76.27 ±0.01	17.38 ±0.01	33.93 ±0.01	47.47 ±0.01

Table 6.5: Dark current values after irradiation for SiPMs with a pixel size of 15μm at different bias voltages and temperatures.[64]

Based on the measured current values, it can be observed that the SiPM model with 10 μm pixels has lower dark current levels, at the same temperature and bias voltage, compared to the model with 15 μm pixels. These results demonstrate that between the two SiPM models studied, the one with 10 μm pixels offers the best performance for muon collider applications. In fact, in addition to increasing the granularity, this model allows the contribution of the dark current to be reduced, thus improving the overall performance of the calorimeter.

Chapter 7

CRILIN prototypes tests with electron beams

This chapter focuses on the tests of the CRILIN prototypes conducted with electron beams at the CERN SPS-H2 facility [66], in which I actively participated during my thesis work.

7.1 Goal of the Test beam

The test beam was carried out on the CRILIN Proto-1 prototype by using high-energy electron beams. The main objectives were:

- Validate the overall functionality of the CRILIN prototype, in particular test the readout electronics for both layers of the Proto-1 setup.
- Measure the time resolution of Proto-1 across a wide energy range.

As outlined in Chapter 4, one of the most critical requirements for the electromagnetic calorimeter in the Muon Collider detector is to achieve excellent time resolution, specifically less than 100 ps. This experimental test is thus fundamental to demonstrate that the CRILIN technology can satisfy this stringent requirement. Additionally, the results from these tests provide valuable insights into the optimization of the overall design of the calorimeter system.

7.2 Overview of test beam instrumentation

The beam test was conducted at the North Area of CERN: a dedicated facility for experimental tests based on particle beams. The North Area is supplied by the Super Proton Synchrotron (SPS) [67], which can provide beams with a wide range of intensity, and energy and with different types of particles such as electrons, protons, muons, and pions, depending on experimental needs. The experimental area features multiple secondary beam lines, one of which, the H2 line, was utilized for the CRILIN test beam. The test was carried out using electron beams with energies in the range of 40 GeV to 150 GeV.

The layout of the experimental setup is shown in Figure 7.1, with the incident electron beam directed from left to right. The z-axis is along the beam direction while the transverse directions are labeled as the x- and y-axes and arranged as indicated in the figure.
In the setup, the Proto-1 prototype was positioned on a 4-axis motorized stage (referred to as the Desy table in Figure 7.1), which allows for precise movements of the plane along two spatial directions (x and y axis) and two rotations.

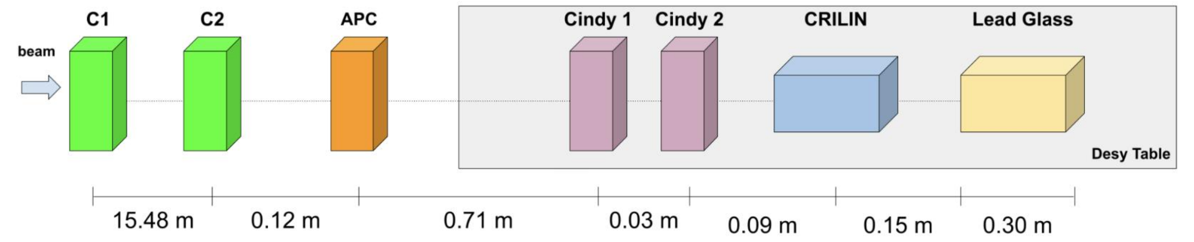

Figure 7.1: Scheme of the layout of the experimental setup used for the beam test. Starting from left to right there are a pair of trackers C1, C2, an APC scintillator, near the experimental table there are a pair of fast scintillators (Cindy 1, Cindy 2), the CRILIN prototype, and finally a lead glass cell. The distances between the various components are indicated below the diagram.

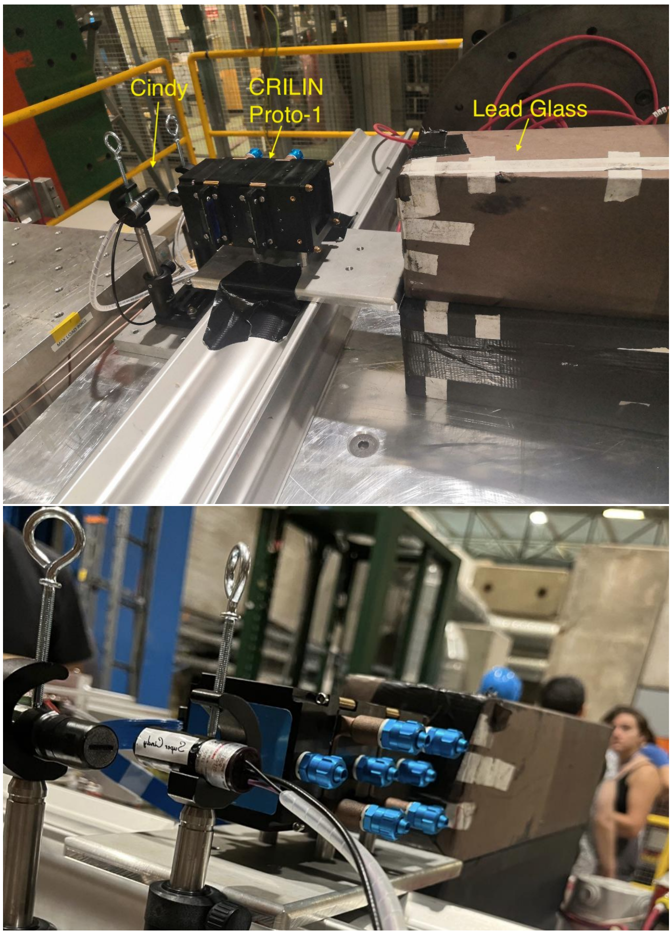

Figure 7.2: Up: Photo of the experimental setup placed on the Desy table. The beam direction is from left to right. In front of the Proto-1 CRILIN prototype, the Cindy detector is positioned for timing reference, and behind the prototype is the lead glass module serving as a tail catcher. Down: Front view of the setup.

Behind the prototype, a lead glass calorimeter cell was placed, to absorb the leakage of the electromagnetic shower produced in the prototype. The shower could not be fully contained due to the presence of only two layers of CRILIN (8.5 X_0). In front of Proto-1, a detector called Cindy was placed. It consists of a pair of plastic fast scintillator (BC408) sensors with dimensions of $5 \times 5 \times 7mm^2$ and dual readout with 9880U photomultiplier. This detector served as an external timing reference for the electrons arriving at the prototype, with a time resolution of 40 ps and it was used to obtain optimal alignment of the experimental table with the beam direction.

Figure 7.2 shows detailed photos of the arrangement of the setup, highlighting the position of the prototype along with the timing reference detector (Cindy) and the lead glass cell. It can be seen that all components were securely fixed to the table using supports to ensure reliable measurements.

The beam position was continuously monitored by a pair of tracking telescope detectors, denoted as C1 and C2 in Figure 7.1. These are silicon micro-strip tracking detectors positioned at a distance between the two stations of 15.48 m. This system enables the reconstruction of the beam particle trajectories and thus the precise determination of particle positions at the CRILIN front surface. With a spatial resolution of 47 μm, it was possible to obtain the reconstruction of the track with an angular resolution of 3μrad.
Finally, the trigger system is based on the coincidence of signals from the two detection stations C1 and C2 and with scintillator counters, labeled APC in Figure 7.1. During data acquisition, only single-particle events were selected, while events showing multi-cluster in the C1 and C2 trackers were discarded. In this way, it was possible to collect electron samples for a single event, in which the position was well determined on the surface of the prototype and the relevant signal was associated without ambiguity.

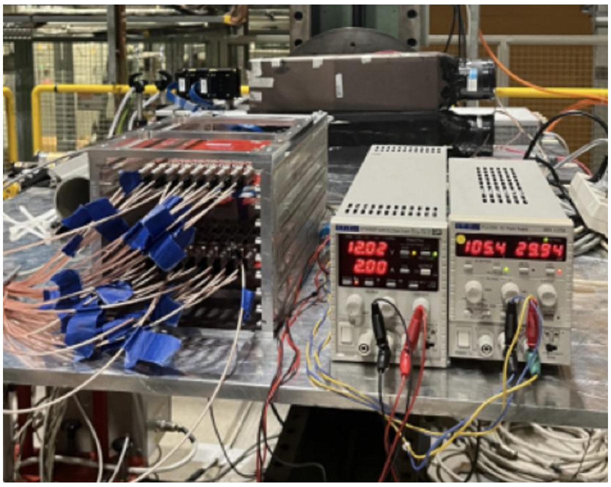

Figure 7.3: Photo of the DAQ system used for the test beam. On the left, the rack containing the Mezzanine electronics boards along with two digitizers is visible, while on the right, the power supply system is shown.

In Figure 7.3, a photo of the data acquisition (DAQ) system is shown. In the rack, visible on the left, are housed the Mezzanine Boards and two CAEN V1742 digitizers [68], each with 32 channels and a sampling rate of 5 Gsps. On the right side, there are the power supply modules that provide the necessary bias voltage for both the data acquisition system and the SiPMs.

7.3 Data acquisition

The data acquisition phase was conducted with the prototype oriented to the incident beam, as illustrated in Figure 7.4. In this arrangement, called backward orientation, the beam hits the prototype from the SiPM side, indicated in orange in the figure, and then passes through the portion of the layer occupied by the crystal, represented in blue.

The prototype was oriented in this specific manner relative to the incident beam to minimize the dependence of the particle's entry position on light transport within the crystal cell.
In fact, beam test results on the Proto-0 prototype [58] show that in the case of forward orientation, where the beam first strikes the crystal side, there is a variation in the waveform shape depending on the particle's impact position on the crystal surface. This effect is due to the way Cherenkov light propagates in the crystal, as shown in Figure 7.5. The solid lines represent a comparison of the waveforms measured from a single readout channel, corresponding to the forward orientation, with three different particle impact regions. In particular, the green line

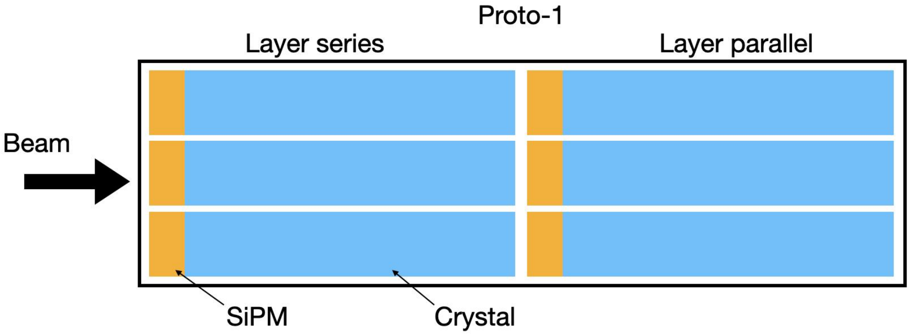

Figure 7.4: Scheme of the prototype orientation considered during the test beam. The beam, coming from the left, first impacts the SiPM side (indicated in orange) before passing through the crystal (shown in blue)

represents the case where the particle impacts the crystal face near the side of the active readout channel; the magenta line, on the other hand, refers to the opposite scenario, where the particle strikes the region opposite the readout channel; finally, the blue line indicates the case where the particle impacts the central region of the crystal face, which is positioned between the two readout channels. The dashed line corresponds to the prototype in the backward orientation. The waveform variation observed in the forward orientation case introduces a source of uncertainty in the measurement of the arrival time of the incident particle, thus leading to a worsening of the temporal resolution. On the contrary, in the backward orientation configuration, the dependence of the waveform on the particle impact position vanishes, since the Cherenkov light, before being detected by the SiPMs, has to propagate along the crystal, being then reflected by the bottom of the crystal and coming back towards the side of the SiPMs. This process allows for randomization of the trajectories of the Cherenkov light, thus eliminating any dependence on the particle impact position on the crystal.

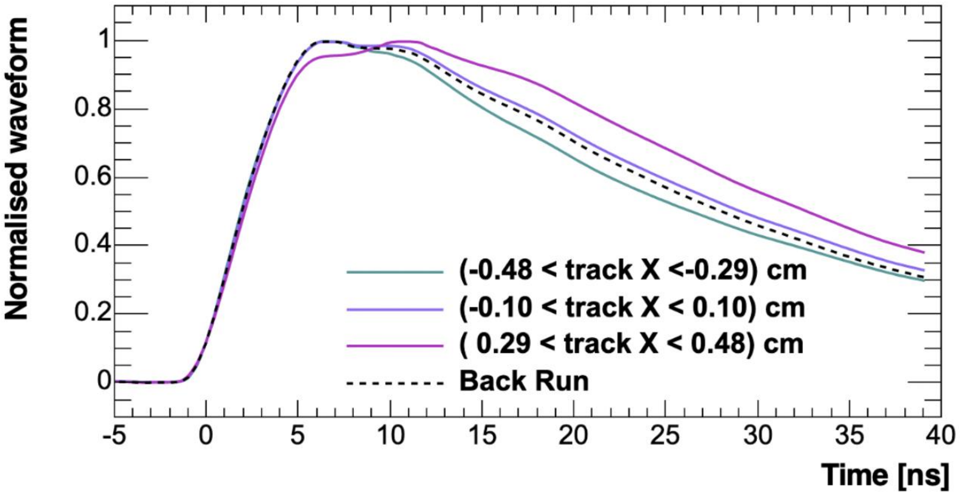

Figure 7.5: The solid lines show a comparison between the shape of the waveforms read by a single readout channel of the CRILIN cell as a function of the impact position of the incipient particle on the crystal face in the case of the forward orientation of the detector. The dashed line refers to the backward configuration.[58].

After the selection of the configuration, the mechanical table was employed to precisely align and center the prototype's face with the incoming beam. This alignment ensured that the prototype was correctly positioned, and the setup was then finalized for data acquisition.

As indicated in Figure 7.4, during the test beam, the two layers of the Proto-1 prototype were equipped with two different SiPM Boards:

- In one layer, the pairs of SiPMs forming a readout channel were connected in series. This is the layer first hit by the beam and is referred to as the **series-layer**.
- In the other layer, a SiPM Board was used where the pairs of SiPMs were connected in parallel. This layer will be identified as the **parallel-layer** and is the one where the beam arrived later.

Data was collected by using electron beams with energy values ranging from 40 GeV to 150 GeV. In Table 7.1 are summarized for each acquisition run, the energy and the number of the collected events.

Beam Energy [GeV]	Number of Events
40	100000
60	100000
80	100000
100	130000
120	110000
150	50000

Table 7.1: Acquisition runs with an electron beam at energies ranging from 40 GeV to 150 GeV.

7.4 Data analysis

This section presents the data analysis I carried out, taking the 120 GeV run as a reference. The final results also include data from other runs carried out at different energies.

7.4.1 Waveform reconstruction

The first step in analyzing the events collected was the reconstruction of the waveforms. During this phase, I selected the events contained within a two-dimensional region (referred to as the fiducial region) in the transverse x and y coordinates relative to the beam direction and centered on the face of the prototype. Figure 7.6 shows the distribution of the hit position in the x-y plane of the prototype surface, with the fiducial region highlighted by a red box. The selection of the x and y coordinate ranges that define the fiducial region was done by analyzing the distributions of impact positions along x and y. Specifically, I determined the ranges using the Full Width at Half Maximum (FWHM) of the distributions.

The waveforms collected within the fiducial region undergo a series of selection requirements before the event reconstruction. These steps are chosen to enhance the quality of the signal from the SiPM by removing noise and distorted signals, ensuring that only valid and significant signals are used in subsequent analyses.

The quality control requirements applied to the waveforms are as follows:

- Low pass filtering: the collected waveforms undergo low pass filtering using a 2nd order Bessel filter [ref]. This filter allows the attenuation of high-frequency noise while preserving the essential features of the signal. The cutoff frequency for this filter is set such that the threshold value referred to the parallel SiPM connection is approximately double that of the series configuration. This setup allows for effective noise reduction without distorting the signal's key characteristics.
- Dynamic Cutoff Frequency Adjustment: the cutoff frequency of the low pass filter is dynamically adjusted based on two parameters: the baseline root-mean-square (RMS) and the rise time of the waveform required to go from 10% to 90% of its final amplitude. The baseline RMS provides a measure of the noise level, while the rise-time indicates how quickly the signal reaches its peak. By defining the cutoff frequency value based on these

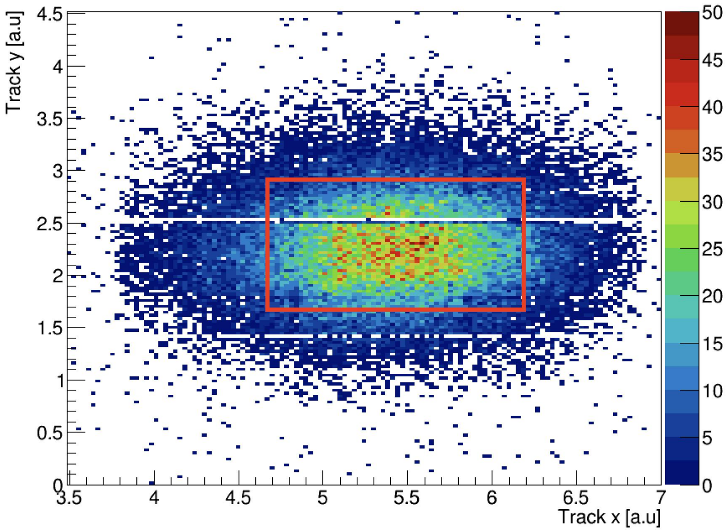

Figure 7.6: Histogram of the x-y position of the events on the prototype's surface. The color scale on the right represents the number of counts. The red box highlights the fiducial region selected for waveform analysis.

waveform parameters, the filtering process is optimized for each waveform, ensuring that noise is minimized without compromising the signal's integrity.

- Wave quality control is based on three parameters: baseline RMS, peak amplitude, and rise-time. These parameters help identify waveforms that may be affected by noise, signal distortion, or other anomalies. Waveforms that fail to meet predefined quality thresholds are identified and filtered out, ensuring that only high-quality signals are considered for further analysis.
- Waveform filtering threshold: to further refine the selection, a selection cut is applied to the waveforms based on their peak amplitude. Only waveforms with a peak greater than 2 mV are selected. This helps to eliminate weak signals, which could be caused by noise.

The waveform reconstruction for each event was based on a waveform template fitting procedure. The template was created by aligning and averaging a large sample of waveforms from individual events. This alignment and averaging process produced a representative waveform template, particularly focused on accurately modeling the rising edge of the signal.
In Figure 7.7, an example is shown where the waveform and its corresponding fit in the rise region can be observed. This template serves as the reference for fitting individual waveforms, allowing for precise extraction of signal characteristics. For further details on the construction of the waveform fit template refer to [58].

Once the reconstruction of the waveform is completed, as shown in Figure 7.7, it was then possible to analyze it by extracting the main parameters that characterize the given event for a specific readout channel. The main extracted parameters are the following:

- **Charge pulse:** is obtained by integrating the signal in an appropriate time interval and dividing it by the digitizer input impedance equal to 50Ω .T_{peak} represents the time relative to the position of the waveform maximum. In Figure 7.7 it is possible to observe the position of the wave peak, identified with the red cross and the relative signal integration interval in green.
- **Pulse amplitude:** represents the maximum value of the waveform's amplitude. As it is possible to see from Figure 7.7, it is correctly extracted from the reconstruction of the waveform.
- **Pulse time:** The reference time for the event in a given readout channel was obtained

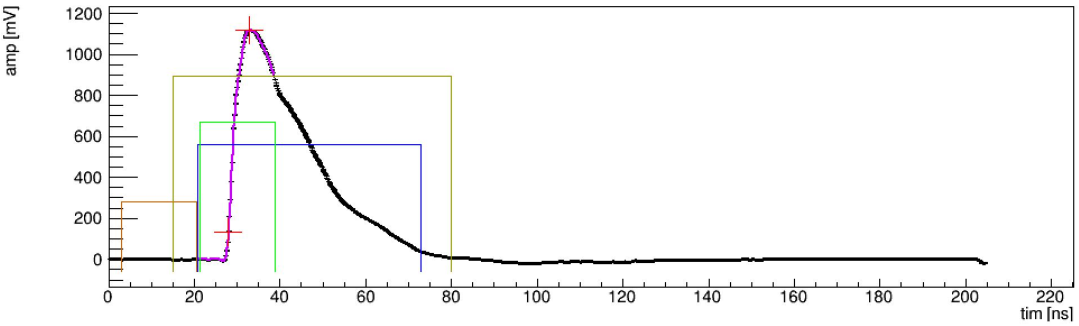

Figure 7.7: Representation of a waveform from a 120 GeV electron signal, measured in one of the two readout channels of the central crystal in the series layer of Proto-1 prototype. The reconstruction template fit for the rise region of the waveform is presented in magenta, along with the corresponding time intervals used to extract the waveform parameters.

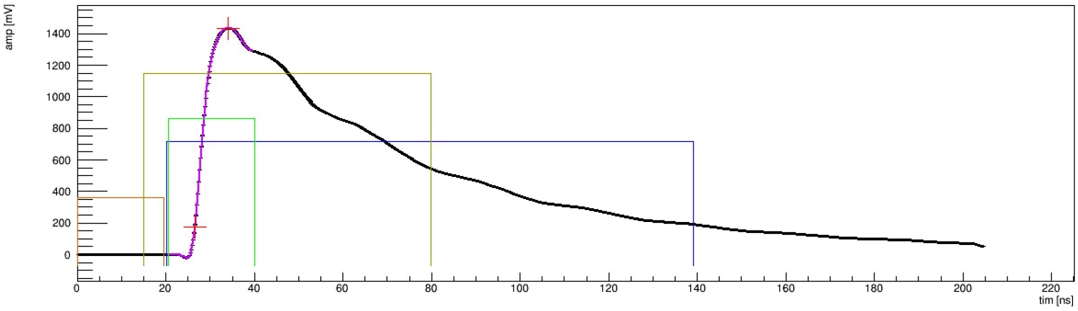

Figure 7.8: Representation of a waveform from a 120 GeV electron signal, measured in one of the two readout channels of the central crystal in the parallel layer of the Proto-1 prototype. The reconstruction template fit for the rise region of the waveform is presented in magenta, along with the corresponding time intervals used to extract the waveform parameters.

from the reconstructed waveform by determining the temporal value corresponding to a fixed Constant Fraction (CF) of the amplitude rise. The CF value is taken equal to 12% of the waveform rise. This value is obtained as a result of a timing optimization study, presented in [55].

- **Base line:** was obtained as the average value of the signal amplitude measured in a time interval of width 15 ns before the rise of the waveform, in Figure 7.7 represented in red.

I carried out this procedure for each readout channel of both layers of the prototype (layer series and layer parallel) and also for the Lead Glass and Cindy detectors. Through this approach, I obtained the necessary parameters to study Proto-1 performance.

7.4.2 Operational monitoring studies

After reconstructing the waveforms, a general evaluation of the prototype's operational performance was conducted. This assessment is essential to ensure that all readout channels were functioning correctly and that no anomalies were present that could affect subsequent analyses, particularly those related to time resolution.

To verify the proper operation of the readout channels, I first conducted a comparison of the collected charge values between the pairs of readout channels for each cell of the prototype. Figure 7.9 displays histograms of the charge for each event, plotted as a function of the two readout channels: Ch0 (x-axis) and Ch1 (y-axis) for the cells in the series layer of the prototype. An analogous plot for the parallel layer is shown in Figure 7.10.

From the results shown in the two figures, it is possible to make the following observations:

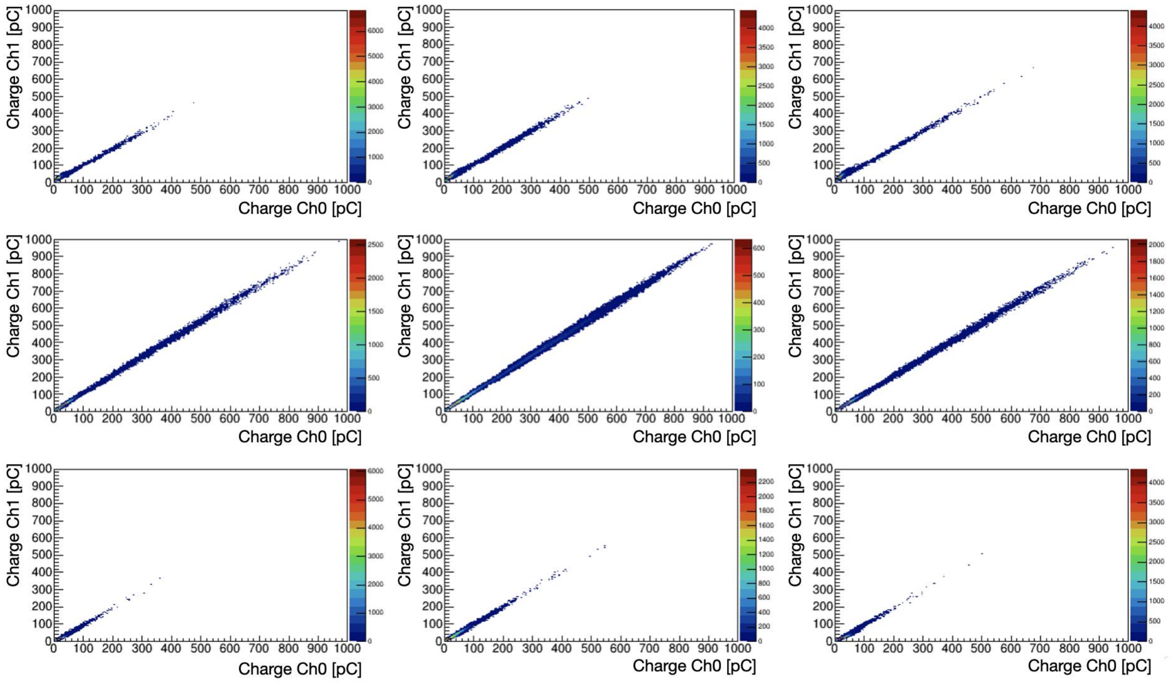

Figure 7.9: Correlation of the charge collected for each event from the cells of the Proto-1 series layer. The x-axis has the value measured by the Ch0 reading channel, while the y-axis is the one of the Ch1 channel. The chromatic scale indicates the number of counts in the individual two-dimensional bins.

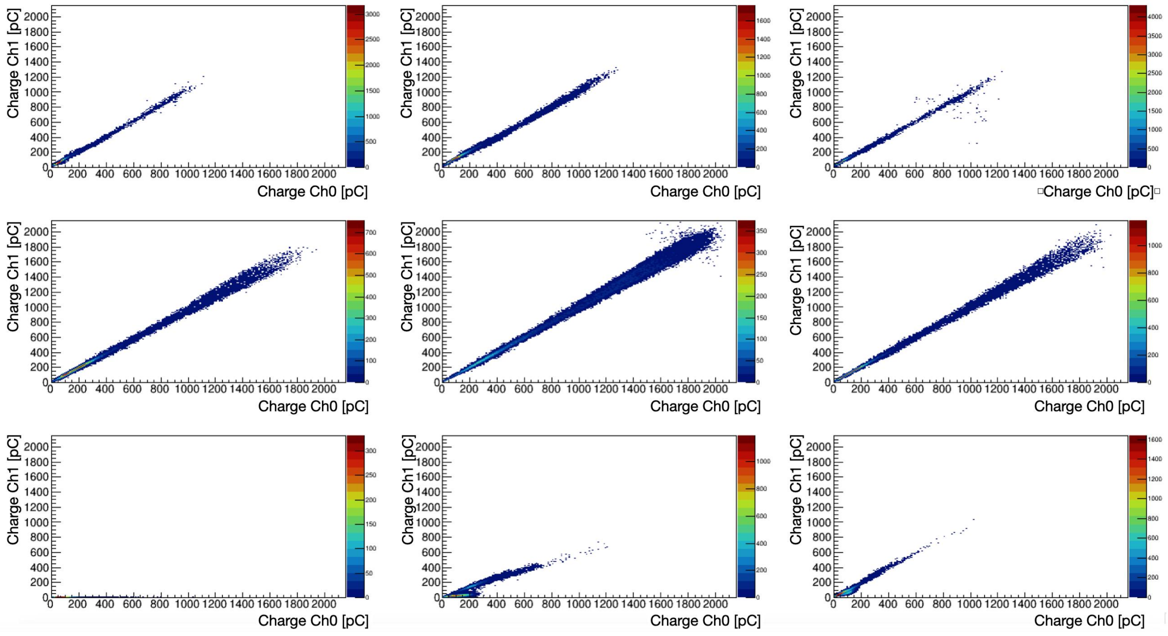

Figure 7.10: Correlation of the charge values collected for each event from the cells of the Proto-1 parallel layer. The x-axis has the value measured by the Ch0 reading channel, while the y-axis has the one of the Ch1 channel. The chromatic scale indicates the number of counts in the individual two-dimensional bins.

- Except for a few cells, the values of the charge collected by the readout channels (Ch0, Ch1) have an excellent correlation. This indicates excellent equalization of the response between the two readout channels for each individual cell, for both layers.
- In reference to the histograms of the parallel layer shown in Figure 7.10, anomalies are noticeable in the three cells located in the bottom row. Starting with the cell on the bottom left, only the Ch0 readout channel is operational, while Ch1 is not working. For the cells

in the center and on the right of the bottom row, there is a lack of perfect homogeneity between the responses of the two channels. This discrepancy is likely due either to a malfunction of the SiPM in Ch1 or damage to the crystal.

- The collected charge values are highest in the central crystal and decrease symmetrically in the surrounding crystals. This pattern suggests that the prototype was correctly aligned with the center of the incident beam. Additionally, it is observed that higher charge values are collected in the parallel layer, which is attributed to the development of the electromagnetic shower induced by the incident electrons.

I conducted this check not only for the 120 GeV electron sample but also for all other runs. In Figure 7.11 and 7.12 the analogous plots relating to the run with energy of 40 GeV are presented. It is possible to observe the same behavior with the only difference that the values of the charge collected in the individual channels are lower than the case at 120 GeV.
This allows us to confirm that the setup remained stable during the data acquisition phase and that there were no further malfunctions in the readout channels.

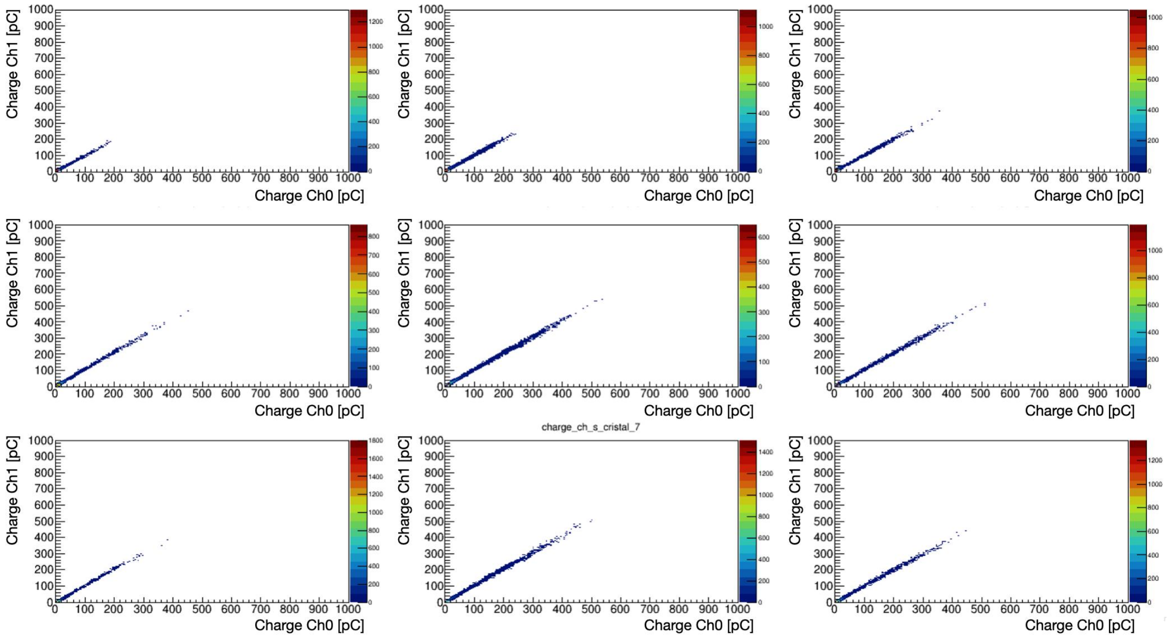

Figure 7.11: Correlation of the charge collected for each event from the cells of the Proto-1 series layer. The x-axis has the value measured by the Ch0 reading channel, while the y-axis has the one of the Ch1 channel. The chromatic scale indicates the number of counts in the individual two-dimensional bins.

To further validate the prototype's performance, I conducted an additional analysis using a sample of 120 GeV electrons. I compared the energy collected across an entire layer (either series or parallel) for each event with the one obtained by using a simulation (the simulation plots were provided by the CRILIN development group from Laboratori Nazionali di Frascati). Figure 7.13 presents the energy distributions obtained from GEANT4 simulations, with the series layer shown on the left and the parallel layer on the right. Figure 7.14 displays analogous histograms that I obtained from the data collected with the 120 GeV electron sample.
As can be noticed, the results from the test beam are in agreement with those from the simulation studies.

7.4.3 Timing

The measurement of the temporal resolution was performed by analyzing the signal arrival times recorded in the two readout channels, called Ch0 and Ch1, associated with the central crystal of the 3x3 matrix for both layers of Proto-1. The parameter of interest considered is ΔT, defined

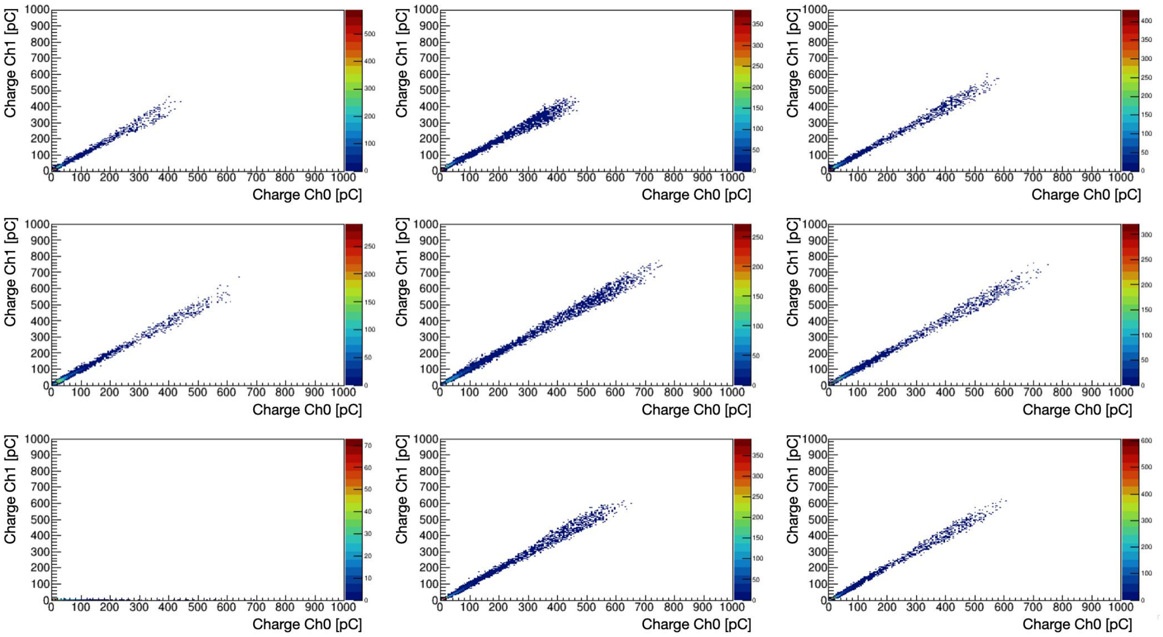

Figure 7.12: Correlation of the charge values collected for each event from the cells of the Proto-1 parallel layer. The x-axis has the value measured by the Ch0 reading channel, while the y-axis has the one of the Ch1 channel. The chromatic scale indicates the number of counts in the individual two-dimensional bins.

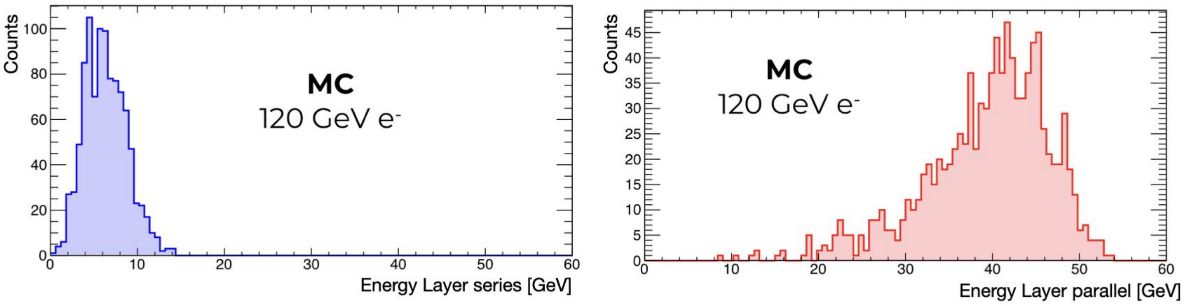

Figure 7.13: Distribution of the energy values deposited by electrons with energy of 120 GeV in the series layer (left) and in the parallel layer (right), obtained through simulation with GEANT4 (the simulation plots were provided by the CRILIN development group from Laboratori Nazionali di Frascati).

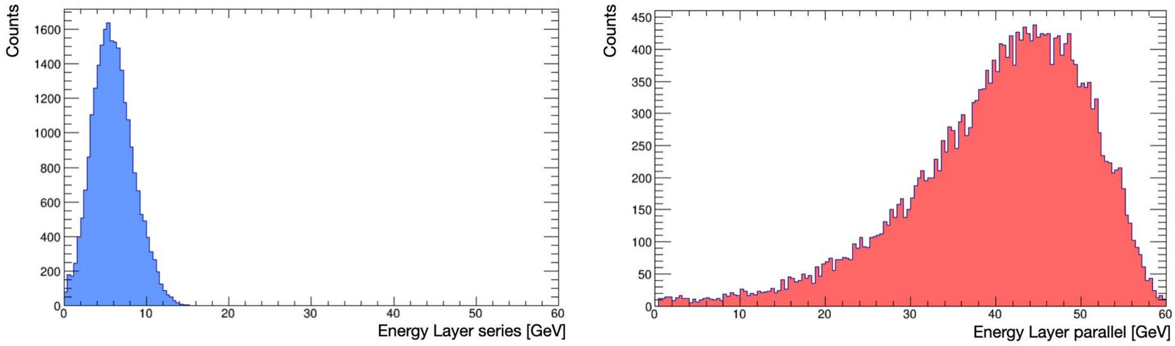

Figure 7.14: Distribution of the energy values deposited by electrons with energy of 120 GeV in the series layer (left) and in the parallel layer (right), obtained from data collected during the acquisition run.

as the difference between the times measured in the two readout channels:

$$\Delta T = T_1 - T_0 \tag{7.1}$$

where T_0 and T_1 represent the times measured in the Ch0 and Ch1 channels respectively. The time difference values were evaluated for each single event of a given data set, obtaining a distribution of ΔT for the layer in series and the layer in parallel respectively.
The distributions obtained were then fitted using a Gaussian function, from which it was possible to extract the value of the standard deviation $\sigma_{\Delta T}$.

Figure 7.15 shows the ΔT distributions obtained for the electron sample with an energy of 120 GeV. The distribution on the left refers to the series layer configuration, while the one on the right refers to the parallel layer configuration. The values of the parameters obtained from the Gaussian fit are indicated in the corresponding figures.
It is possible to observe that in the case of the parallel layer, the distribution has a greater width. This effect can be attributed to several factors, including increased signal fluctuation in parallel-connected SiPMs and the effects of shower propagation, which starts in the series-connected layer and subsequently expands into the parallel-connected layer.

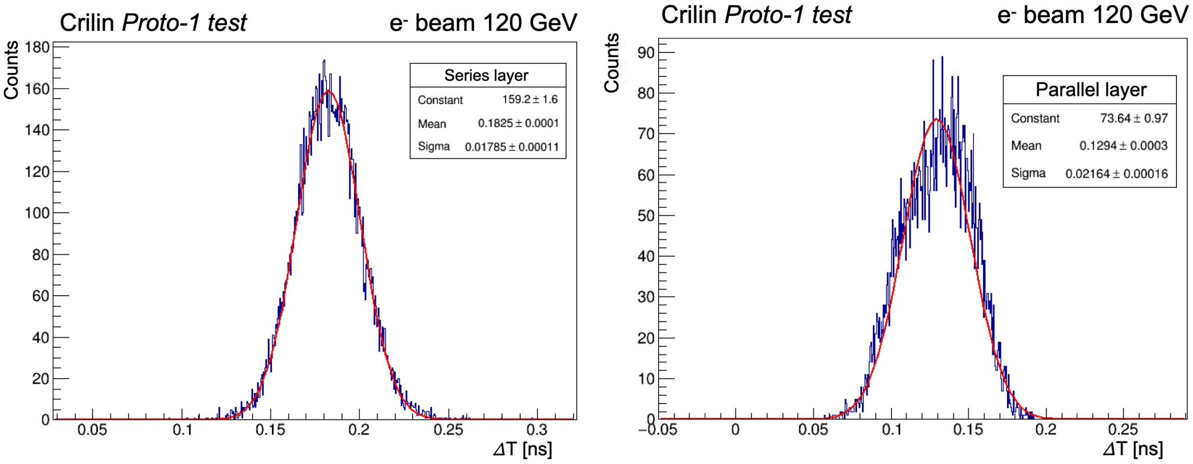

Figure 7.15: Distributions of the time difference measured by the Ch0 and Ch1 channels of the central crystal, for the run with electrons at 120 GeV. The left figure refers to the series layer, the right figure to the parallel layer.

Figures 7.16 and 7.17 present the corresponding distributions for the runs with electron beams at energies of 150 GeV and 60 GeV, respectively.

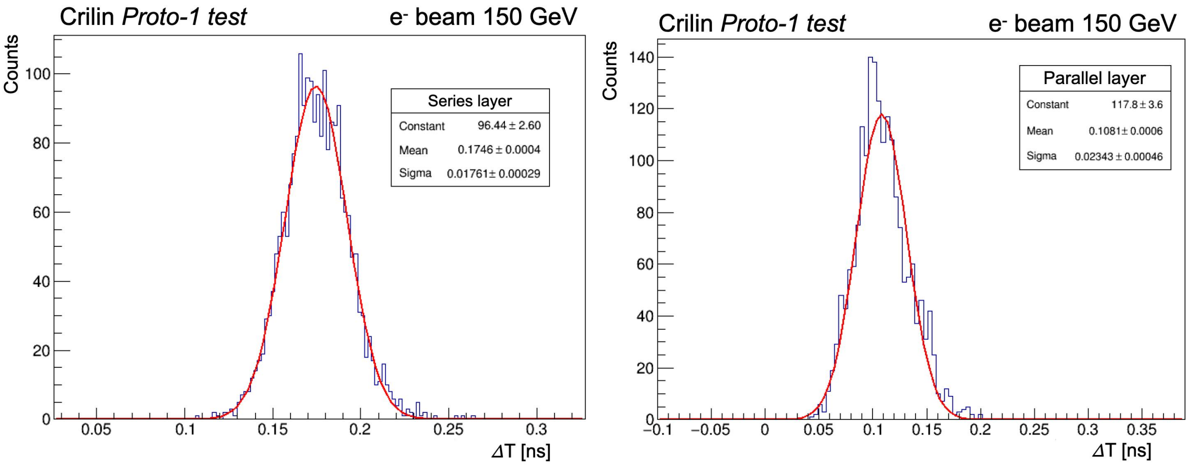

Figure 7.16: Distributions of the time difference measured by the Ch0 and Ch1 channels of the central crystal, for the run with electrons at 150 GeV. The left figure refers to the series layer and the right figure to the parallel layer.

The temporal resolution was determined from the sigma value of the ΔT distribution obtained through a Gaussian fit. In this context, it was assumed that the temporal resolution of the two

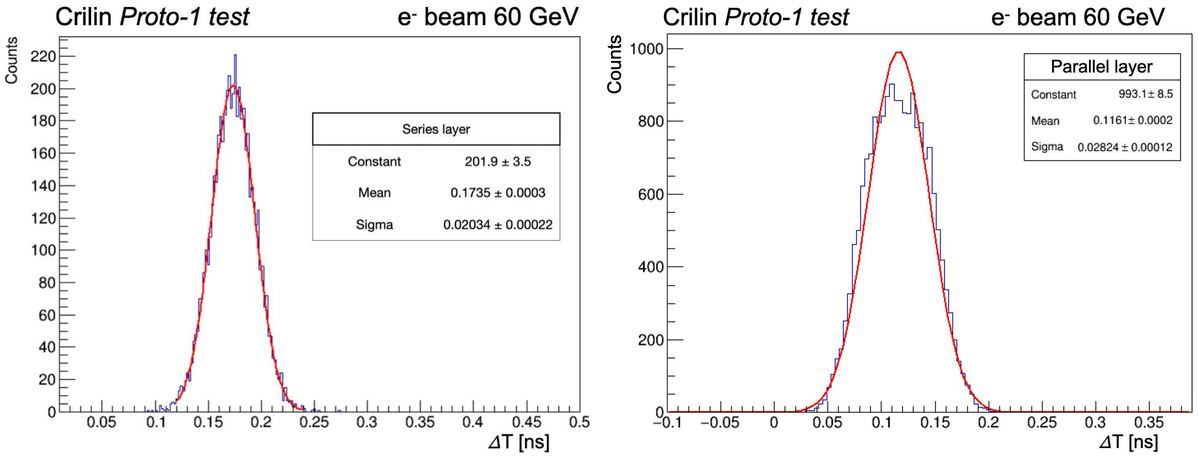

Figure 7.17: Distributions of the time difference measured by the Ch0 and Ch1 channels of the central crystal, for the run with electrons at 60 GeV. The left figure refers to the series layer and the right figure to the parallel layer.

readout channels, corresponding to the SiPMs pair connected in series or in parallel respectively, was equivalent: $\sigma_{T_0} = \sigma_{T_1} = \sigma_T$. Under this assumption, the temporal resolution was estimated using the following relation:

$$\sigma_{MT} = \frac{\sigma_{\Delta T}}{2} \tag{7.2}$$

where σ_{MT} represents the average temporal resolution obtained by the two readout channels of the single crystal calorimeter.

This relationship is based on the fact that the two readout channels provide independent measurements, each with the same uncertainty σ_T. Indeed the uncertainty associated with the time difference of the two channels, $\sigma_{\Delta T}$, follows from the following error relation:

$$\sigma_{\Delta T} = \sqrt{2}\sigma_T \tag{7.3}$$

Combining this relationship with the fact that the uncertainty associated with the mean-time measured by the two readout channels of the single cell $(T_1 + T_0/2)$ is given by:

$$\sigma_{MT} = \frac{\sigma_T}{\sqrt{2}} \tag{7.4}$$

therefore the relationship used to estimate the temporal resolution reported in Equation 7.2 can be obtained. With this approach is possible to calculate the average temporal resolution starting from the information of the width of the ΔT distribution.

For the 120 GeV energy run, using this approach, a temporal resolution of about 9 ps for the series layer and about 11 ps for the parallel layer was obtained. Table 7.2 reports the results for all runs at different energies, highlighting separately the values obtained for the series layer and those for the parallel layer. It can be observed that, in the case of the series layer, the values of the average temporal resolution progressively decrease as the beam energy increases. On the contrary, in the case of the parallel layer, a monotonic trend is not observed. This behavior is most likely influenced by the development of the electromagnetic shower, which starts to form in the series layer and then propagates to the parallel layer, where the incident particle arrives at a later time.

Beam Energy [GeV]	σ_{MT} Series Layer [ps]	σ_{MT} Parallel Layer [ps]
150	8.7 ± 0.1	11.7 ± 0.2
120	8.92 ± 0.05	10.8 ± 0.8
100	9.2 ± 0.1	9.5 ± 0.2
80	9.44 ± 0.1	13.25 ± 0.1
60	10.2 ± 0.1	14.12 ± 0.05
40	10.7 ± 0.8	16.4 ± 0.4

Table 7.2: Time resolution values as a function of the incident electron beam energy. The central column shows the results for the series layer. The right column shows the results for the parallel layer.

Figure 7.18 summarizes the average temporal resolution values obtained for each run at different energies (E_{beam}) in the case of the layer with SiPMs connected in series. The data were fitted using the following function:

$$\sigma_{MT} = \frac{p0}{\sqrt{E_{beam}}} \oplus p1 \tag{7.5}$$

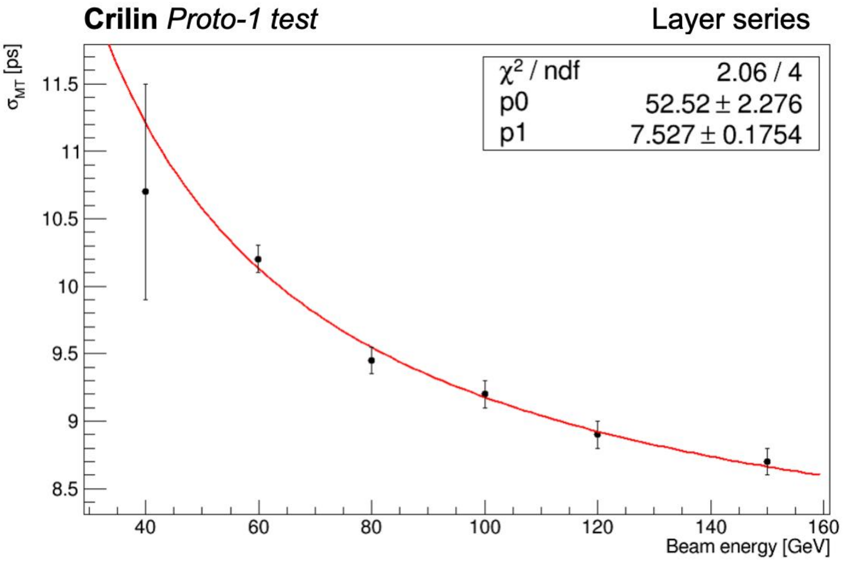

Figure 7.18: Distributions of the time difference measured by the Ch0 and Ch1 channels of the central crystal, for the run with electrons at 60 GeV. The left figure refers to the series layer, the right figure to the parallel layer.

The result obtained from the fit is shown in the figure and is summarized below:

$$\sigma_{MT} = \frac{(52 \pm 2)\ \text{ps}}{\sqrt{E\ (\text{GeV})}} \oplus (7.5 \pm 0.1)\ \text{ps} \tag{7.6}$$

This result demonstrates that the CRILIN proposal meets the time resolution requirements for the electromagnetic calorimeter of the Muon Collider detector. This compliance allows to precisely apply the acquisition time windows, essential for the mitigation of BIB particles in a crucial region of the detector, such as that of the electromagnetic calorimeter. The time selection capability, together with future developments of both the detector and the reconstruction algorithms, will allow to significantly improve the calorimeter performance. In this way, it will be possible to conduct an extensive physics campaign to confirm the validity of the Muon Collider design.

Conclusions

The work developed in this thesis concerns the design, study, and development of a new detector aimed at collecting muon collisions at a very high center-of-mass energy. The examples described above concern $\sqrt{s} = 1.5, 3$ and 10 TeV. My activities have been dedicated mainly to the study of a novel electromagnetic calorimeter proposed for the first time for a muon collider experiment.

The main issue to address in the design of a calorimeter for a muon collider detector is the BIB. As described in 1.4, the fluxes of particles created by the muon decay, arrive on the detector and could jeopardize its performance even in the presence of the nozzle. The tracker system and the electromagnetic calorimeter are the most affected.

My thesis starts briefly introducing the most important physics cases that justify the muon collider proposal 1.1. An overall description of the facility is given in 1.2 with the detector concept explained in 2. This is the first time a detector concept for $\sqrt{s} = 10$ TeV is proposed, therefore a significant amount of optimization is expected in the future. The software used to study the detector performance is illustrated in 3. The novel calorimeter, CRILIN, is introduced in 5. In this chapter, I summarise the studies I have done to determine the requirements for an electromagnetic calorimeter in the muon collider environment and CRILIN is described. The characterization of the performance obtained with the simulation is done in 5. The results obtained with the BIB generated at $\sqrt{s} = 1.5$ TeV (that has almost the same characteristics as that at $\sqrt{s} = 3$ TeV) show how the use of such a design can provide an optimal calorimeter to do physics at a muon collider. I obtained an energy resolution, including the contribution of BIB

$$\frac{\sigma_E}{E} = \frac{(15 \pm 1)\%}{\sqrt{E(GeV)}} \oplus (0.77 \pm 0.04). \tag{7.7}$$

When I moved to study the BIB effect for a center-of-mass energy collision of 10 TeV, done in this thesis for the first time, I realized that several things have to be changed. I optimized the digitization of the CRILIN signal including also the time information. But the cluster reconstruction in the Pandora code needs to be rewritten for shower generated by different particles and this activity is in progress.

In addition to the simulation studies, I participated in the CRILIN prototype tests. Chapter 6 describes prototype 0 and prototype 1 and the preliminary tests performed in Frascati. The primary aim of these initial tests was to characterize the components of the CRILIN calorimeter, focusing specifically on their radiation hardness. The results from these tests indicate that the PbF_2 crystals exhibit excellent radiation hardness. Additionally, to minimize the dark current in the SiPMs, it is essential to use sensors with a pixel size of 10 μm.

Chapter 7 is dedicated to the description of the tests performed at CERN by using beams of electrons with energies ranging from 40 GeV to 150 GeV impinging on the CRILIN prototype Proto-1. During these test beam experiments, I was actively involved in both the data acquisition process and the subsequent data analysis. My primary focus was on characterizing the temporal resolution of the CRILIN detector. I mainly focused on characterizing the temporal resolution of CRILIN and the result I obtained is the following:

$$\sigma_{MT} = \frac{(52 \pm 2)\ \mathrm{ps}}{\sqrt{E\ (\mathrm{GeV})}} \oplus (7.5 \pm 0.1)\ \mathrm{ps} \tag{7.8}$$

These results confirm that the CRILIN electromagnetic calorimeter meets the requirements for a detector for an experiment at the Muon Collider. In particular, CRILIN demonstrates that it can significantly contribute to the mitigation of BIB effects in the calorimeter system.

The findings presented in this thesis are highly encouraging and suggest that CRILIN is a promising candidate for an advanced electromagnetic calorimeter. Its development will continue with new simulations involving electrons instead of the photons used in this thesis, which will allow it to complete its characterization and make improvements to the software for the clustering phase.
Regarding experimental tests, a new prototype is currently under design, significantly larger than the Proto-0 and Proto-1 prototypes. This new prototype will consist of 4 layers of 5x5 crystal matrices. Upcoming test beams will provide crucial information for further enhancing CRILIN and for a more detailed assessment of its performance.

Bibliography

[1] G. I. Budker. “Accelerators and colliding beams”. In: *Conf. Proc. C* 690827 (1969). Ed. by A. I. Alikhanian, pp. 33–39.

[2] M. A. Palmer. “An Overview of the US Muon Accelerator Program”. In: *International Workshop on Beam Cooling and Related Topics.* June 2013.

[3] International Muon Collider Collaboration. *Muon Collider.* `https://muoncollider.web.cern.ch/`. Accessed: 2024-09-01. 2024.

[4] Particle Data Group. “Review of Particle Physics”. In: *Prog. Theor. Exp. Phys.* 2022.8 (2022), p. 083C01. DOI: `10.1093/ptep/ptac097`. URL: `https://pdg.lbl.gov`.

[5] Antonio Costantini et al. “Vector boson fusion at multi-TeV muon colliders”. In: *Journal of High Energy Physics* 2020.9 (Sept. 2020). ISSN: 1029-8479. DOI: `10.1007/jhep09(2020)080`. URL: `http://dx.doi.org/10.1007/JHEP09(2020)080`.

[6] Richard Ruiz et al. “The Effective Vector Boson Approximation in high-energy muon collisions”. In: *Journal of High Energy Physics* 2022.6 (June 2022). ISSN: 1029-8479. DOI: `10.1007/jhep06(2022)114`. URL: `http://dx.doi.org/10.1007/JHEP06(2022)114`.

[7] Kateryna Korshynska et al. *Z’ boson mass reach and model discrimination at muon colliders.* 2024. arXiv: `2402.18460 [hep-ph]`. URL: `https://arxiv.org/abs/2402.18460`.

[8] Peter W. Higgs. “Broken Symmetries and the Masses of Gauge Bosons”. In: *Physical Review Letters* 13.16 (1964), pp. 508–509. DOI: `10.1103/PhysRevLett.13.508`. URL: `https://journals.aps.org/prl/abstract/10.1103/PhysRevLett.13.508`.

[9] CERN. *CMS Experiment.* Accessed: 2024-08-30. 2024. URL: `https://www.home.cern/science/experiments/cms`.

[10] CERN. *ATLAS Experiment.* Accessed: 2024-08-30. 2024. URL: `https://www.home.cern/science/experiments/atlas`.

[11] Hind Al Ali et al. “The muon Smasher’s guide”. In: *Reports on Progress in Physics* 85.8 (July 2022), p. 084201. ISSN: 1361-6633. DOI: `10.1088/1361-6633/ac6678`. URL: `http://dx.doi.org/10.1088/1361-6633/ac6678`.

[12] Massimo Casarsa, Donatella Lucchesi, and Lorenzo Sestini. “Experimentation at a Muon Collider”. In: *Annual Review of Nuclear and Particle Science* (July 2024). ISSN: 1545-4134. DOI: `10.1146/annurev-nucl-102622-011319`. URL: `http://dx.doi.org/10.1146/annurev-nucl-102622-011319`.

[13] Paolo Andreetto et al. *Higgs Physics at a $\sqrt{s} = 3$ TeV Muon Collider with detailed detector simulation.* 2024. arXiv: `2405.19314 [hep-ex]`. URL: `https://arxiv.org/abs/2405.19314`.

[14] LHC Higgs Cross Section Working Group et al. *LHC HXSWG interim recommendations to explore the coupling structure of a Higgs-like particle.* 2012. arXiv: `1209.0040 [hep-ph]`. URL: `https://arxiv.org/abs/1209.0040`.

[15] Matthew Forslund and Patrick Meade. “High precision higgs from high energy muon colliders”. In: *Journal of High Energy Physics* 2022.8 (Aug. 2022). ISSN: 1029-8479. DOI: `10.1007/jhep08(2022)185`. URL: `http://dx.doi.org/10.1007/JHEP08(2022)185`.

[16] CERN. *Compact Linear Collider (CLIC).* Accessed: 2024-08-30. 2024. URL: `https://home.cern/science/accelerators/compact-linear-collider`.

[17] C. Accettura et al. *Interim report for the International Muon Collider Collaboration (IMCC)*. 2024. arXiv: `2407.12450 [physics.acc-ph]`. URL: `https://arxiv.org/abs/2407.12450`.

[18] Carlotta Accettura et al. *Towards a Muon Collider*. 2023. arXiv: `2303.08533 [physics.acc-ph]`. URL: `https://arxiv.org/abs/2303.08533`.

[19] D. Neuffer et al. “Muon Sources for Particle Physics - Accomplishments of the Muon Accelerator Program”. In: *8th International Particle Accelerator Conference*. May 2017. DOI: `10.18429/JACoW-IPAC2017-TUPIK038`.

[20] A. N. Skrinsky and V. V. Parkhomchuk. “Cooling Methods for Beams of Charged Particles. (In Russian)”. In: *Sov. J. Part. Nucl.* 12 (1981), pp. 223–247.

[21] M. Bogomilov et al. *First demonstration of ionization cooling by the Muon Ionization Cooling Experiment*. 2019. arXiv: `1907.08562 [physics.acc-ph]`. URL: `https://arxiv.org/abs/1907.08562`.

[22] S. Alex Bogacz. “Muon Acceleration - RLA and FFAG”. In: *AIP Conf. Proc.* 1382.1 (2011). Ed. by B. S. Acharya, Maury Goodman, and Naba Kumar Mondal, pp. 202–204. DOI: `10.1063/1.3644312`.

[23] F. Ruggiero and H. Hahn. *Rapid-Cycling Synchrotrons: Beam Dynamics and Applications*. FERMILAB-TM-2367. Fermilab, 2008. URL: `https://lss.fnal.gov/archive/test-tm/2000/fermilab-tm-2367.pdf`.

[24] S. Machida and N. K. K. W. B. Wu. “Fixed-Field Alternating Gradient Accelerators”. In: *Physics of Accelerators and Detectors* 48.4 (2001), pp. 701–709. DOI: `10.1016/S0168-9002(01)00214-1`. URL: `https://doi.org/10.1016/S0168-9002(01)00214-1`.

[25] F. Collamati et al. “Advanced assessment of beam-induced background at a muon collider”. In: *Journal of Instrumentation* 16.11 (Nov. 2021), P11009. ISSN: 1748-0221. DOI: `10.1088/1748-0221/16/11/p11009`. URL: `http://dx.doi.org/10.1088/1748-0221/16/11/P11009`.

[26] H. Bethe and W. Heitler. “Stopping of fast particles and radiation by atoms”. In: *Proceedings of the Royal Society of London. Series A, Containing Papers of a Mathematical and Physical Character* 146.856 (1934), pp. 83–112.

[27] M. D. Swanson. “Incoherent $e^{-}e^{-}$ Production in High-Energy Colliders”. In: *Journal of High Energy Physics* 2001.12 (2001), pp. 123–135. DOI: `10.1088/1126-6708/2001/12/123`. URL: `https://doi.org/10.1088/1126-6708/2001/12/123`.

[28] B. G. Irwin and M. B. H. Lee. “Beam Halo Effects in Muon Colliders”. In: *Nuclear Instruments and Methods in Physics Research A* 618 (2010), pp. 122–129. DOI: `10.1016/j.nima.2010.05.048`. URL: `https://doi.org/10.1016/j.nima.2010.05.048`.

[29] Ilya F. Ginzburg. *Initial Particle Instability in Muon Collisions*. 1996. arXiv: `hep-ph/9601272 [hep-ph]`. URL: `https://arxiv.org/abs/hep-ph/9601272`.

[30] A. M. L. A. I. Y. N. M. G. *MARS15 User’s Guide*. Available online at: https://www.fnal.gov/projects/mars/. Fermilab. 2015. URL: `https://www.fnal.gov/projects/mars/`.

[31] P. M. G. Abreu et al. “Studies of Muon Collider Backgrounds and their Impact on Detector Design”. In: *Physics Review Special Topics - Accelerators and Beams* 6.5 (2003), p. 051001. DOI: `10.1103/PhysRevSTAB.6.051001`. URL: `https://doi.org/10.1103/PhysRevSTAB.6.051001`.

[32] A. Ferrari et al. *FLUKA User’s Guide*. Available online at: https://fluka.cern. CERN. 2005. URL: `https://fluka.cern`.

[33] CERN FLUKA Team. *LineBuilder Package*. Accessed: 2024-08-30. 2024. URL: `https://twiki.cern.ch/twiki/bin/view/FlukaTeam/FlukaLineBuilder`.

[34] CERN FLUKA Team. *Fluka Element Data Base*. Accessed: 2024-08-30. 2024. URL: `https://twiki.cern.ch/twiki/bin/view/FlukaTeam/FlukaElementDataBase`.

[35] Nazar Bartosik et al. *Simulated Detector Performance at the Muon Collider*. 2022. arXiv: `2203.07964 [hep-ex]`. URL: `https://arxiv.org/abs/2203.07964`.

[36] CERN Proceedings. *CERN Proceedings, Vol 1 (2017): CERN-BINP Workshop for Young Scientists in e+e- Colliders*. en. 2017. DOI: 10.23727/CERN-PROCEEDINGS-2017-001. URL: https://e-publishing.cern.ch/index.php/CP/issue/view/26.

[37] Laura Buonincontri. “Study of Mitigation Strategies of Beam-Induced Background and Higgs Boson Couplings Measurements at a Muon Collider”. Accessed: 2024-09-02. Master’s Thesis. Padua, Italy: University of Padua, 2021. URL: https://hdl.handle.net/20.500.12608/22861.

[38] “The Phase-2 Upgrade of the CMS Endcap Calorimeter”. In: (2017). DOI: 10.17181/CERN.IV8M.1JY2.

[39] MadGraph Collaboration. *MadGraph*. Accessed: 2024-08-30. 2024. URL: https://cp3.irmp.ucl.ac.be/projects/madgraph/.

[40] International Linear Collider Software (ILCSoft). *ILCSoft: The International Linear Collider Software*. Accessed: 2024-08-30. 2024. URL: https://ilcsoft.desy.de/portal.

[41] DD4HEP Collaboration. *DD4HEP: Detector Description for High-Energy Physics*. Accessed: 2024-08-30. 2024. URL: https://dd4hep.web.cern.ch/dd4hep/.

[42] Geant4 Collaboration. *Geant4: Software for Radiation and Particle Transport*. Accessed: 2024-08-30. 2024. URL: https://geant4.web.cern.ch/.

[43] Natascia Bartosik. *Beam-Induced Background in a Muon Collider Detector*. Presentation at the INFN Workshop, 21 December 2022. 2022. URL: https://agenda.infn.it/event/33332/contributions/187231/attachments/100672/140081/2022_12_21_bartosik_v0.pdf.

[44] E. Brondolin et al. “Conformal tracking for all-silicon trackers at future electron–positron colliders”. In: *Nuclear Instruments and Methods in Physics Research Section A: Accelerators, Spectrometers, Detectors and Associated Equipment* 956 (Mar. 2020), p. 163304. ISSN: 0168-9002. DOI: 10.1016/j.nima.2019.163304. URL: http://dx.doi.org/10.1016/j.nima.2019.163304.

[45] Massimo Casarsa. *Muon Collider Detectors: Beam-Induced Backgrounds and Mitigation Strategies*. CERN EP Seminar. Presentation at CERN EP Seminar, 30 August 2023. 2023. URL: https://indico.cern.ch/event/1291157/contributions/5888177/attachments/2900970/5087220/casarsa_MuCollDetectors.pdf.

[46] P. Billoir. “Progressive track recognition with a Kalman-like fitting procedure”. In: *Comput. Phys. Commun.* 57 (1989), pp. 390–394.

[47] Pierre Billoir and S. Qian. “Simultaneous pattern recognition and track fitting by the Kalman filtering method”. In: *Nucl. Instrum. Meth. A* 294 (1990), pp. 219–228. DOI: 10.1016/0168-9002(90)91835-Y.

[48] R. Mankel. “A Concurrent track evolution algorithm for pattern recognition in the HERA-B main tracking system”. In: *Nucl. Instrum. Meth. A* 395 (1997), pp. 169–184. DOI: 10.1016/S0168-9002(97)00705-5.

[49] Xiaocong Ai et al. “A Common Tracking Software Project”. In: *Computing and Software for Big Science* 6.1 (Apr. 2022). ISSN: 2510-2044. DOI: 10.1007/s41781-021-00078-8. URL: http://dx.doi.org/10.1007/s41781-021-00078-8.

[50] Randal Ruchti and Katja Kruger. *Particle Flow Calorimetry*. 2022. arXiv: 2203.15138 [physics.ins-det]. URL: https://arxiv.org/abs/2203.15138.

[51] J. S. Marshall. *Presentation on PandoraPFA with LC Reconstruction*. https://github.com/PandoraPFA/Documentation/blob/master/Pandora_LC_Reconstruction.pdf. Accessed: 2024-08-31.

[52] Richard Wigmans. *Calorimetry: Energy Measurement in Particle Physics*. Oxford University Press, 2000. URL: https://doi.org/10.1093/acprof:oso/9780198548561.001.0001.

[53] K. M. Black et al. *Muon Collider Forum Report*. 2023. arXiv: 2209.01318 [hep-ex]. URL: https://arxiv.org/abs/2209.01318.

[54] L. Sestini et al. “Design a Calorimeter System for the Muon Collider Experiment”. In: *Proceedings of the European Physical Society Conference on High Energy Physics (EPS-*

HEP2021). Vol. 398. Pre-published on January 26, 2022. T12: Detector R&D and Data Handling, 2022. URL: `https://doi.org/10.22323/1.398.0869`.

[55] S. Ceravolo et al. “Crilin: A CRystal calorImeter with Longitudinal InformatioN for a future Muon Collider”. In: *Journal of Instrumentation* 17.09 (Sept. 2022), P09033. ISSN: 1748-0221. DOI: `10.1088/1748-0221/17/09/p09033`. URL: `http://dx.doi.org/10.1088/1748-0221/17/09/P09033`.

[56] Sergio Ceravolo et al. “Crilin: A Semi-Homogeneous Calorimeter for a Future Muon Collider”. In: *Instruments* 6 (Oct. 2022), p. 62. DOI: `10.3390/instruments6040062`.

[57] Zoltan Seres et al. “Optical transmission of Mylar and Teflon films”. In: *Optical Engineering - OPT ENG* 33 (Sept. 1994), pp. 3031–3033. DOI: `10.1117/12.177513`.

[58] C. Cantone et al. *Beam test, simulation, and performance evaluation of PbF_2 and PWO-UF crystals with SiPM readout for a semi-homogeneous calorimeter prototype with longitudinal segmentation*. 2023. arXiv: `2308.01148 [physics.ins-det]`. URL: `https://arxiv.org/abs/2308.01148`.

[59] Peter Kozma, Robert Bajgar, and Petr Kozma. “Radiation resistivity of PbF 2 crystals”. In: *Nuclear Instruments and Methods in Physics Research Section A-accelerators Spectrometers Detectors and Associated Equipment - NUCL INSTRUM METH PHYS RES A* 484 (May 2002), pp. 149–152. DOI: `10.1016/S0168-9002(01)02011-3`.

[60] Frank Simon. “Silicon photomultipliers in particle and nuclear physics”. In: *Nucl. Instrum. Meth. A* 926 (2019), pp. 85–100. DOI: `10.1016/j.nima.2018.11.042`. arXiv: `1811.03877 [physics.ins-det]`.

[61] Giovanni Calzolari. “MDI: Machine-Detector Interface at ICHEP 2024”. In: *Proceedings of the 41st International Conference on High Energy Physics (ICHEP)*. `https://indico.cern.ch/event/1291157/contributions/5890023/attachments/2899807/5085792/MDI_ICHEP24_final.pdf`. 2024.

[62] A. Cemmi et al. “Radiation study of Lead Fluoride crystals”. In: *JINST* 17.05 (2022), T05015. DOI: `10.1088/1748-0221/17/05/T05015`. arXiv: `2107.12307 [physics.ins-det]`.

[63] Hamamatsu Photonics. *S14160-3010PS MPPC*. `https://www.hamamatsu.com/eu/en/product/optical-sensors/mppc/mppc_mppc-array/S14160-3010PS.html`.

[64] C. Cantone et al. “R&D status for an innovative crystal calorimeter for the future Muon Collider”. In: *EPJ Web Conf.* 288 (2023), p. 02002. DOI: `10.1051/epjconf/202328802002`.

[65] ENEA. *Il Frascati Neutron Generator e i test di resistenza a radiazione*. `https://www.eai.enea.it/archivio/ricerca-e-innovazione-per-la-sfida-spaziale/il-frascati-neutron-generator-e-i-test-di-resistenza-a-radiazione.html`.

[66] CERN. *H2 Beamline at CERN SPS North Area*. `https://sba.web.cern.ch/sba/BeamsAndAreas/H2/H2_presentation.html`.

[67] CERN. *Super Proton Synchrotron (SPS)*. `https://home.cern/science/accelerators/super-proton-synchrotron`.

[68] CAEN. *V1742 - 32 Channel 12-bit 5 GS/s Switched Capacitor Digitizer*. `https://www.caen.it/products/v1742/`.